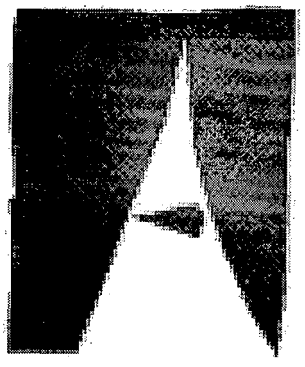

Measurement of the W mass from the $WW \rightarrow q\bar{q}q\bar{q}$ channel with the ALEPH detector [1]

Imma Riu

Universitat Autònoma de Barcelona

Departament de Física

Institut de Física d'Altes Energies

Edifici Cn

E-08193 Bellaterra (Barcelona)

December 1998

[1] Ph. Dissertation

Contents

List of Figures

List of Tables

Chapter 1

Introduction

During almost 40 years the physics model of electroweak and strong interactions between particles, the Standard Model [1] (SM), has succesfully survived every test. In recent years new powerful tests of the model have been performed mainly at LEP but also at SLC and at the Tevatron. At LEP, the high statistics data collected at the Z peak allowed very accurate measurements of the parameters of the SM and provided a very good test at the quantum level of the electroweak theory. The mass of the Z boson was measured with a relative error of 0.002% while the mass of the W boson, measured at hadron colliders, with a relative error of 0.1%.

In June 1996, a second phase of LEP (LEP2) started at a centre-of-mass energy of 161 GeV, the kinematical threshold of W-pair production. The interest was focussed in W physics for the first time at LEP and the W mass measurement became one of the main purposes of this running period. Its accurate measurement can constraint the allowed range of values of the mass of the Higgs boson, the only particle of the SM not discovered yet, as well as constraint the existence of new physics beyond the SM.

At 161 GeV the Ws are produced at rest and the sensitivity of the cross-section to the W mass allow a first measurement of the W boson mass. In November 1996 the centre-of-mass energy was raised up to 172 GeV. At this energy, the W bosons are produced sufficiently boosted to allow the direct reconstruction of the boson. Making use of a very good performance LEP reached an unprecedent centre-of-mass energy of 183 GeV in 1997, and high statistics was accumulated allowing the best accurate W mass measurement at LEP so far. Even higher statistics with higher

centre-of-mass energies are expected to be accumulated during the coming years, hopefully allowing an accuracy of 30 MeV for the W mass.

In this thesis, the measurement of the W mass using the hadronic channel and the data collected by ALEPH at 172 GeV and 183 GeV centre-of-mass energy is detailed in the following chapters. The direct reconstruction method is used to determine the mass of the W boson. Particular problems to the fully hadronic decay channel come from the large background contamination, the important distortions due to fragmentation and detector effects when reconstructing the hadronic jets. Due to the similarities of the signal and background processes, the selection is based on a multidimensional analysis which performs a good separation. Taking the algorithm which best pairs the jets, the invariant masses of both Ws can be reconstructed, and using a kinematical fit, their resolutions are improved. The W mass is measured using the reweighting procedure that takes the Monte Carlo with a given W mass which best fits to the data.

An important systematic uncertainty comes from the final state interactions which increase the error on the W mass measured with the hadronic channel.

Chapter 2 describes the theoretical framework of the analysis. Chapter 3 gives a description of the ALEPH detector emphasizing the parts of the apparatus used for the analysis. The description of the measurement of the W mass in the hadronic channel using the data collected at 172 GeV centre-of-mass energy is detailed in chapter 4. In chapter 5 the W mass is measured with the data collected at 183 GeV centre-of-mass energy. The combination of both results, together with the combination with the other LEP and hadron colliders W mass measurements are given in chapter 6. Finally, the summary and conclusions are given in chapter 7. A list of appendices give some more detailed information on the formulae used.

Chapter 2

Theoretical framework

This chapter provides a few introductory remarks on the Standard Model and then the reminder of this chapter concentrates on the areas of the theory which relate directly to the W boson. After a brief introduction to the Standard Model , the W pair production in e^+e^- annihilation is described. The different methods of measuring the W mass are given at the end of the chapter.

2.1 The Standard Model structure

The Standard Model (SM) is a gauge theory, based on the group $SU(3)_C \otimes SU(2)_L \otimes U(1)_Y$, describing electroweak and strong interactions between particles. The model describing electroweak interactions was firstly introduced by Glashow, Weinberg and Salam [1]. Later, through the GIM mechanism (Glashow, Iliopoulos and Maiani) [2], the electroweak interactions of quarks were also introduced. This theory predicted the existence of neutral and charged currents mediated by the massive gauge bosons ($W^{\pm}$, Z^0) which were for the first time observed in the $p\bar{p}$ colider at CERN in 1983.

The unification of the electromagnetic (mediated by photons) and weak interactions (mediated by $W^{\pm}$) is done by requiring a gauge invariance under the $SU(2)_L \otimes U(1)_Y$ transformation group. As a result of a spontaneous symmetry breaking process, the vector bosons adquire masses without breaking the local gauge invariance of the lagrangian, and a new scalar particle, the Higgs, is predicted although it has not been observed experimentally yet. The renormalization

was established in 1971 by 't Hooft [3] ensuring the systematic cancellations of divergences order by order of the perturbative expansion of the hamiltonian and its absorption in the definition of a finite set of "bare" parameters. The strong interaction between quarks (mediated by eight massless gluons) is included in the electroweak model by a field theory, local gauge invariant under the symmetry group $SU(3)_C$.

The Standard Model consists of fermionic families of quarks and leptons, gauge bosons and the Higgs bosons.

There are experimental results showing the existence of only three families with the hypotesis of three light neutrinos [4]. The fermionic matter content is organised in a 3-fold family structure as shown in table 2.1. An antiparticle corresponds to each particle with the same mass and opposite quantum numbers. The left-(right-) handed fields transform as $SU(2)_L$ doublets(singlets). Each quark appears in three different 'colours' and transform as $SU(3)_C$ via the exchange of gluons. The $\{d', s', b'\}$ weak isospin eigenstates are related to the $\{d, s, b\}$ mass eigenstates through the unitarity matrix Cabibbo-Kobayashi-Maskawa [5], which depends on three mixing angles and a phase space which have to be determined experimentally. This phase is the responsible for the CP symmetry breaking in the SM and it is widely believed that CP non-conservation in the early Universe is one of the sources of the apparent imbalance between matter and antimatter. Recent experiments [6] seem to indicate the existence of $\nu_e - \nu_\mu$ oscillations, thus introducing flavour mixing in the leptonic sector and invalidating the hypothesis of massless neutrinos.

The mass of the Higgs boson is constrained by direct search at LEP to be greater than $84\,\mathrm{GeV}/c^2$ at 95% confidence level [4].

The precise electroweak measurements at LEP have some sensitivity to the $\log(m_\mathrm{H})$ through loop corrections, and allow to constraint m_H to be below $280\,\mathrm{GeV}/c^2$ at 95% confidence level [7]. The next generation machine LHC as well as the data collected by LEP2 and Tevatron in the near future should be able to decide whether the simplest Higgs model is correct or not. At LEP2, the precise measurement of M_W will be of big importance in order to stringe more the limits on the mass of the Higgs, as well as further constrain the allowed regions in the space of parameters of the Minimal Supersymmetric Standard Model (MSSM). Later will be discussed in some more detail.

Leptons

$$\begin{array}{ccc} \begin{pmatrix} \nu_{e_L} \\ e_L \end{pmatrix}_{Y=-\frac{1}{2}} & \begin{pmatrix} \nu_{\mu_L} \\ \mu_L \end{pmatrix}_{Y=-\frac{1}{2}} & \begin{pmatrix} \nu_{\tau_L} \\ \tau_L \end{pmatrix}_{Y=-\frac{1}{2}} \\ (\ e_R\ )_{Y=-1} & (\ \mu_R\ )_{Y=-1} & (\ \tau_R\ )_{Y=-1} \end{array}$$

Quarks

$$\begin{array}{ccc} \begin{pmatrix} u_L \\ d'_L \end{pmatrix}_{Y=-\frac{1}{2}} & \begin{pmatrix} c_L \\ s'_L \end{pmatrix}_{Y=-\frac{1}{2}} & \begin{pmatrix} t_L \\ b'_L \end{pmatrix}_{Y=-\frac{1}{2}} \\ (\ u_R\ )_{Y=\frac{2}{3}} & (\ c_R\ )_{Y=\frac{2}{3}} & (\ t_R\ )_{Y=\frac{2}{3}} \\ (\ d'_R\ )_{Y=-\frac{1}{3}} & (\ s'_R\ )_{Y=-\frac{1}{3}} & (\ b'_R\ )_{Y=-\frac{1}{3}} \end{array}$$

Table 2.1: Gauge group representations of fermion fields.

2.2 W pair production in e^+e^- annihilation

The W bosons at LEP2 are produced in pairs above threshold by the annihilation of electrons and positrons $e^+e^- \rightarrow W^+W^-$.

At tree level (lowest order) the 'on-shell' production of a W pair is either through the *annihilation* diagram e^+e^- into a virtual γ or a Z^0 boson, or via the double *conversion* diagram with a t-channel neutrino exchange [1]. These processes are shown in figure 2.1 and are called CC03 diagrams (three Charged-Current processes).

A second phase of the process follows ('off-shell' W pair production) when each of the initial W's decay into two fermions, thus producing a detectable final state signal of four fermions. This is due to the fact that the massive bosons are unstable particles; they have a finite width Γ_W. A detailed description of the W width follows.

2.2.1 The W width

The width of the W boson is a crucial ingredient for the (off-shell) W pair production cross-section since it is the responsible for the 'off-shellness' of the W boson. It

[1] The Higgs boson exchange diagram is neglected since it is suppressed by a factor m_e/M_W.

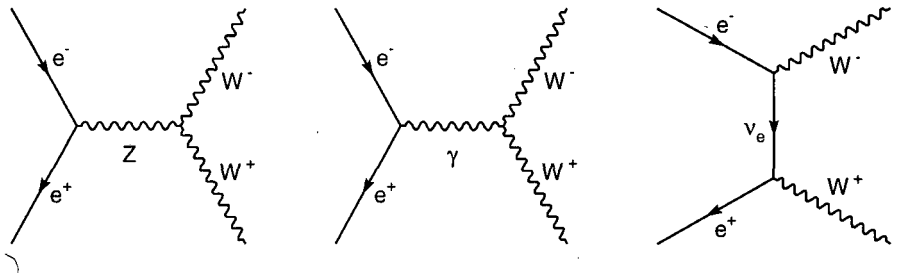

Figure 2.1: CC03 diagrams of W^+W^- production.

importantly distorts the W lineshape close to the threshold and determines the topologies of the W^+W^- final states through the partial widths.

The W bosons may be described as resonances with a Breit-Wigner shape distorted by effects such as detector response, background contamination, initial state radiation, etc. The W boson Breit-Wigner has a total finite width Γ_W (to avoid singularities c.f. section 2.4.4) which corresponds to the sum of the partial decay width $\Gamma_{W\to f_i f'_j}$ of each of the W channels, described in section 2.3. The partial W width for each decay channel at lowest order can be obtained from the matrix element:

$$\Gamma_{W\to f_i f'_j} = \frac{g_W^2 M_W}{48\pi} |V_{ij}|^2 N_C^f \tag{2.1}$$

where massless fermions are assumed. For leptonic decays the mixing matrix V_{ij} is diagonal and the colour factor N_C^f equals one; for hadronic decays V_{ij} is the relevant element of the CKM matrix, and (neglecting QCD corrections) N_C^f is three. g_w is the weak coupling of the W field.

By summing over the partial decay widths and neglecting the fermion masses, a simple formula for the total width is obtained: [10]

$$\Gamma_W \simeq \frac{3g_w^2}{16\pi} M_W. \tag{2.2}$$

When taking into account electroweak and QCD radiative corrections an improved Born approximation for the partial widths (for leptonic $\nu_i \ell_i$ and hadronic

$u_i d_j$ decays) is obtained:

$$\Gamma_{\mathrm{W}\to\nu_i\ell_i} \simeq \frac{G_\mu M_{\mathrm{W}}^3}{6\sqrt{2}\pi}, \tag{2.3}$$

$$\Gamma_{\mathrm{W}\to u_i d_j} \simeq \frac{G_\mu M_{\mathrm{W}}^3}{2\sqrt{2}\pi}|V_{ij}|^2\left(1+\frac{\alpha_s(M_{\mathrm{W}}^2)}{\pi}\right), \tag{2.4}$$

$$\tag{2.5}$$

as well as for the total width:

$$\Gamma_{\mathrm{W}} \simeq \frac{3G_\mu M_{\mathrm{W}}^3}{2\sqrt{2}\pi}\left(1+\frac{2\alpha_s(M_{\mathrm{W}}^2)}{3\pi}\right). \tag{2.6}$$

G_μ is the Fermi constant and α_s is the strong coupling constant. Note that Γ_{W} is proportional to the third power of M_{W}.

Concerning the impact of Γ_{W} on the determination of M_{W}, two different points of view can be adopted. Either the total width of the W boson is extracted simultaneously with the mass, or the functional dependence $\Gamma_{\mathrm{W}} = \Gamma_{\mathrm{W}}(M_{\mathrm{W}})$ of the Standard Model is imposed as a constraint for increased accuracy on M_{W}.

Precise measurements of the W width, like those of the Z^0 width, may yield evidence for non-standard decays involving, for example, supersymmetric particles or heavy quarks [95].

2.3 The W decays

Since the W boson decays into quarks (67.8% of the times) and leptons (32.2% of the times), one may classify the four-fermion $\mathrm{W^+W^-}$ final states into:

- Hadronic channel: $\mathrm{W^+W^-} \to \mathrm{q_1\bar{q}_2\,q_3\bar{q}_4}$, (4q) with a branching ratio of 45.9%.
- Semileptonic channel: $\mathrm{W^+W^-} \to \ell^-\bar{\nu}_\ell\,\mathrm{q_1\bar{q}_2}$, $\ell^+\nu_\ell\,\mathrm{q_1\bar{q}_2}$, ($\ell\nu$2q) with a branching ratio of 43.7%.
- Leptonic channel: $\mathrm{W^+W^-} \to \ell^-\bar{\nu}_\ell\,\ell'^+\nu'_\ell$, ($2\ell\nu$) with a branching ratio of 10.4%.

In the hadronic channel, the most probable decays are: $\mathrm{W^+} \to \mathrm{u\bar{d}}$, $\mathrm{c\bar{s}}$ as the decay involving a b quark is negligible.

2.3.1 Four-fermion production

Besides the W^+W^- production other processes occur at LEP2:

$$e^+e^- \rightarrow Z^0Z^0, \tag{2.7}$$
$$e^+e^- \rightarrow We\nu_e, \tag{2.8}$$
$$e^+e^- \rightarrow Z^0e^+e^-, \tag{2.9}$$
$$e^+e^- \rightarrow Z^0\nu_e\bar{\nu}_e \tag{2.10}$$

among others. The actually measurable final states in the above reactions are their decay products. All of them are just special cases of $e^+e^- \rightarrow 4f$. The number of Feynman diagrams contributing to a given final state can be very large and the same four-fermion final state can originate from several reactions. For example, $e^+e^- \ \nu_e\bar{\nu}_e$ can be originated from any of the reactions above. To distinguish them, they will be called *signal* when coming from W^+W^- production and *background* when coming from other reactions.

Not all the diagrams contribute equally. In the W pair production the CC03 diagrams (fig. 2.1) dominate.

A classification of four-fermion processes

In general all possible four-fermion final states are subdivided into two classes (for certain final states both classes overlap):

- Charged-Current processes ('CC'-type): via the production of (up, anti-down) and (down, anti-up) fermion pairs. These are the contributing processes to the W^+W^- signal events.

- Neutral-Current processes ('NC'-type): via a pair of virtual neutral vector bosons. These diagrams contribute to the background processes.

The number of Feynman diagrams in the CC classes are shown in table 2.2.

One may distinguish three different cases for 'CC'-type processes, all of them containing the CC03 processes as a subset:

	$d\bar{u}$	$s\bar{c}$	$\bar{e}\nu_e$	$\bar{\mu}\nu_\mu$	$\bar{\tau}\nu_\tau$
$d\bar{u}$	*43*	**11**	20	**10**	**10**
$e\bar{\nu}_e$	20	20	*56*	18	18
$\mu\bar{\nu}_\mu$	**10**	**10**	18	*19*	**9**

Table 2.2: Number of Feynman diagrams for 'CC'-type final states.

(i) The `CC11` family.

The two fermion pairs are different and the final state does not contain identical particles neither electrons nor electron neutrinos (**boldface** numbers in table 2.2). There are less diagrams if neutrinos are produced (`CC09`, `CC10` families). A typical four-quark process with 11 contributing Feynman diagrams is $u\bar{d}s\bar{c}$.

(ii) The `CC20` family.

The final state contains one $e^{\pm}$ together with its neutrino (Roman numbers in table 2.2). The additional diagrams to (i) have a t-channel gauge boson exchange. In figure 2.2 all the diagrams contributing to $e^+e^- \to e^-\nu_e u\bar{d}$ are shown. Graphs numbers 15 and 16 are called *fusion* diagrams, while graphs numbers 11 to 14 are called *bremsstrahlung* diagrams (graphs 4 to 10 are also bremsstrahlung diagrams of a W from Bhabha-like scattering usually called singly-resonant diagrams) and graphs numbers 17 to 20 *multiperipheral* diagrams. For a purely leptonic final state, a `CC18` family results.

(iii) The `mix43` and `mix56` families.

Two mutually charge conjugated fermion pairs are produced (*italic* numbers in table 2.2). Differing from the cases (i) and (ii), the diagrams may contain neutral boson exchanges ('NC'-type diagrams), and therefore `mix-` named. If neutrinos are produced, the `mix43` family converts into `mix19`. With the two charge conjugate ($\bar{e}\nu_e$) doublets, `mix56` family is obtained.

A similar classification can be done for the 'NC'-type diagrams [62].

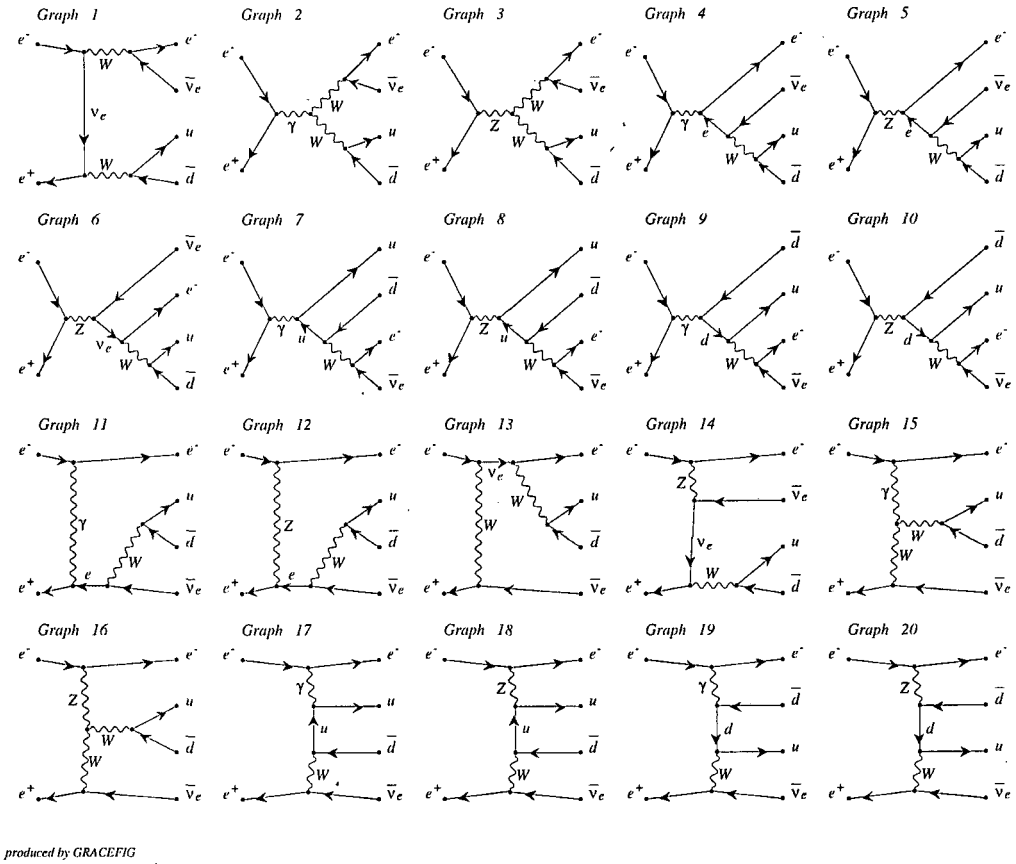

Figure 2.2: Set of the 20 charged current diagrams (CC20) contributing to the process $e^+e^- \to e^-\nu_e u\bar{d}$. The first diagrams correspond to the CC03 diagrams containing two resonating W bosons. The figure has been produced by using the GRACE [59] program.

2.4 W^+W^- cross-section

In this section some of the important features of the theoretical cross-sections which are relevant to the W mass measurement are described.

2.4.1 Cross-sections for the W^+W^- signal and backgrounds

Schematically the cross-section of the process $e^+e^- \to 4f(+\gamma, g, ...)$, σ_{tot} can be decomposited into signal, σ, and background, σ_{bkg}, contributions although neither

contribution is separately exactly gauge invariant nor experimentally distinguishable in general:

$$\sigma_{\text{tot}} = \sigma + \sigma_{\text{bkg}}, \tag{2.11}$$

$$\sigma = \sigma^0(1 + \delta_{\text{EW}} + \delta_{\text{QCD}}) \tag{2.12}$$

where the various terms correspond to:

(i) σ^0: the Born contribution from the three CC03 leading order diagrams from $e^+e^- \to W^+W^-$.

(ii) δ_{EW}: higher order electroweak radiative corrections, including loop corrections, real photon emission, etc.

(iii) δ_{QCD}: higher order QCD corrections to W^+W^- final states containing quark pairs. They can lead to additional jets in the final state, e.g. $W^+W^- \to q\bar{q}q\bar{q}g$ from one hard gluon emission. This affects the direct reconstruction method as the kinematic fits to reconstruct the W mass assume a four-jet final state.

(iv) σ_{bkg}: background contribution as for example from non-resonant diagrams (e.g. $e^+e^- \to \mu^+\nu_\mu W^-$) and QCD contributions $e^+e^- \to q\bar{q}gg(\gamma), q\bar{q}q\bar{q}(\gamma)$ to the four-jet final state.

More detailed description of (i) and (ii) follows.

2.4.2 The W^+W^- on-shell cross-section

In the on-shell W^+W^- production, i.e. when neglecting the decays of the W's, the total cross-section at the lowest order (Born approximation) can be analytically calculated leading to the following expression:

$$\sigma^0 \sim \frac{\pi\alpha^2}{s}\frac{1}{4\sin^4\theta_W}4\beta + \mathcal{O}(\beta^3) \tag{2.13}$$

where θ_W is the Weinberg angle and $\beta = \sqrt{1 - 4M_W^2/s}$. In figure 2.3 the W^+W^- on-shell cross-section is shown. The contribution to the cross-section proportional

to β is due to the t-channel, while the contribution from the s-channel and the s-t interference is proportional to β^3 [2].

Since accurate predictions of the cross-section are vital, the use of the simple on-shell description of W pair production cannot be justified and it is necessary to include additional effects from initial state radiation, Coulomb singularity, finite width of the decaying W's and inclusion of four-fermion background.

2.4.3 The W^+W^- off-shell cross-section

The leading order cross-section for off-shell W pair production can be described by a two-fold convolution of a hard-scattering off-shell cross-section with Breit-Wigner density functions [11]:

$$\sigma(s) = \int_0^s ds_1 \rho(s_1) \int_0^{(\sqrt{s}-\sqrt{s_1})^2} ds_2 \rho(s_2) \sigma^0(s; s_1, s_2), \tag{2.14}$$

where

$$\rho(s) = \frac{1}{\pi} \frac{\Gamma_W}{M_W} \frac{s}{(s - M_W^2)^2 + s^2\Gamma_W^2/M_W^2} \tag{2.15}$$

is the Breit-Wigner like function associated to the $W^{\pm}$ propagators.

The $\sigma^0(s; s_1, s_2)$ is the on-shell cross-section of the W pair with invariant masses s_1 and s_2 at the leading order. It contains terms corresponding to the CC03 diagrams for W pair production and their interferences. Explicit expressions for the various contributions can be found in Ref. [11].

From equation 2.14, it can be seen that, when not taking into account radiative corrections, the influence of the W mass to the cross-sections is exclusively through the off-shell W propagators. All other parts are independent of M_W and Γ_W.

In the W propagator of the equation 2.15 an s-dependent W width is used:

$$\Gamma_W(s) = \frac{s}{M_W^2} \Gamma_W, \tag{2.16}$$

where $\Gamma_W \equiv \Gamma_W(M_W^2)$. Therefore the resonance associated to the W boson is a definition of the W mass, the same definition as for the Z^0 boson at LEP1.

[2] This is the consequence of CP conservation, fermion-helicity conservation in the initial state, and the orthogonality of different partial waves [8].

From the theoretical point of view another possible approach is a constant W width in the propagator:

$$\bar{\rho}(s) = \frac{1}{\pi} \frac{\bar{M}_W \bar{\Gamma}_W}{\left(s - \bar{M}_W^2\right)^2 + \bar{M}_W^2 \bar{\Gamma}_W^2}. \tag{2.17}$$

This approach introduces a different W mass definition. For a discussion see Ref. [13]. Numerically the values of the mass and the width of the W from both definitions are related by: [14]

$$\bar{M}_W = M_W - \frac{1}{2} \frac{\Gamma_W^2}{M_W} \simeq M_W - 27\,\text{MeV}, \tag{2.18}$$

$$\bar{\Gamma}_W = \Gamma_W - \frac{1}{2} \frac{\Gamma_W^3}{M_W^2} \simeq M_W - 0.7\,\text{MeV}. \tag{2.19}$$

These relations may be derived from the following relation:

$$(s - \bar{m}_W^2 + i\bar{m}_W^2 \bar{\Gamma}_W) = \frac{s - M_W^2 + i\,s\Gamma_W/M_W}{1 + i\,\Gamma_W/M_W}. \tag{2.20}$$

For the present analysis the variable width in the propagator will be taken as the definition of the W mass.

2.4.4 Gauge invariance

When going from on-shell W pair production to the off-shell case, two sources of gauge non-invariance arise.

First of all the use of incomplete sets of contributions. Only the `CC03` diagrams have been taken into account instead of all four-fermion diagrams, which would give a gauge independent result for a given final state. As for example, for a final state with four different fermions and no electrons or positrons the gauge invariance is fulfilled when adding the singly-resonant diagrams (bremstrahlung diagrams of a W from Bhabha-like scattering, described in 2.3.1) to the doubly-resonant ones (`CC03` diagrams).

Secondly and more fundamental gauge invariance is the introduction of the finite width to cure for the gauge-noninvariantce of the resonant graphs having poles at

$s = M_W^2$. At the same time, unitarity has to be preserved through a proper energy dependence. In field theory, such width arises naturally from the imaginary parts of higher order diagrams describing the boson self-energies, resummed to all orders. In the past, the Z^0 resonance was described to very high numerical accuracy by using this procedure. However, in doing a Dyson summation of self-energy graphs, only a very limited subset of all possible higher order diagrams are taken, leaving a residual gauge dependence. Many schemes have been developed to solve for this problem:

- 'fixed-width scheme':

$$\frac{1}{s - M_W^2} \longrightarrow \frac{1}{s - M_W^2 + i M_W \Gamma_W} \tag{2.21}$$

  where s is the invariant mass. It is also used for $s < 0$. This scheme has no physical motivation since, in perturbation theory, the propagator for space-like momenta do not develop an imaginary part. Consequently, unitarity is violated.

- 'running-width scheme': To improve unitarity,

$$\frac{1}{s - M_W^2} \longrightarrow \frac{1}{s - M_W^2 + i M_W \Gamma_W(s)} \tag{2.22}$$

  where: $\Gamma_W(s) = \frac{s}{M_W^2}\Gamma_W(M_W^2)$. Still it does not solve the gauge dependence. This scheme leads to completely unreliable results when collinear singularities are present.

- Others as 'fudge-factor scheme' [15], 'pole scheme' [16], 'fermion-loop scheme' [17]. Although the last scheme is well justified in standard perturbation theory, the computation is very time consuming.

By studying how much the predictions of different schemes differ [18], the 'fixed width scheme' gives numerical results close to the ones obtained with the 'fermion-loop scheme', eventhough the gauge dependence is not solved.

2.5 Radiative corrections

Since the measurement of the W mass is one of the key parameters of the electroweak theory, a good precision is necessary. Therefore the theoretical accuracy of the Standard Model predictions should be of half a percent [18], although fortunately specific final states, distributions, or observables do not require such a precision. In this context, radiative corrections are mandatory.

Ideally one would like to have the full radiative corrections to the final state of four fermions originated from the two decaying vector bosons. In practice such a calculation does not exist and is not required for the present accuracy.

The complete set of $\mathcal{O}(\alpha)$ next-to-leading order corrections to W^+W^- production is available for the on-shell case, comprising the virtual one-loop corrections and the real-photon bremsstrahlung [19] [20]. However, it is not the same for the off-shell case. By using the on-shell calculation as a guide, some of the largest effects can be possibly predicted. As for example, the contribution coming from the Coulomb correction (the long-range electromagnetic interaction between almost stationary heavy particles), initial state radiation (emission of photons collinear with the initial state e^+e^- , and further corrections. The coefficients of these corrections involve large factors like $\log(s/m_e^2)$, $\sqrt{M_W/\Gamma_W}$, m_t^2/M_W^2. Once these corrections are taken into account the remaining ones are expected not to be larger than $\mathcal{O}(\alpha)$.

Trying to divide the $\mathcal{O}(\alpha)$ corrections into different parts the situation differs from LEP1 (the $\mu^+\mu^-$ production, for example). It is not possible to divide them into initial state radiation, final state radiation and its interferece, because the photon should couple to all charged particles in a line of the Feynman diagram, and it is not the case for the t-channel diagram. The two sets of initial and final state radiation Feynman diagrams are not separately gauge invariant. Therefore another natural division of the radiative corrections is: the virtual, soft-photonic, and hard-photonic contributions.

2.5.1 Coulomb singularity

This correction is associated to the very old known long-range electromagnetic interaction [21]: when oppositely charged particles have low relative velocity $v \ll 1$ (in units of c) Coulomb effects enhance the cross-section by a factor, which to

leading order in α/v is $(1 + \alpha\pi/v)$, provided that the particles are stable (on-shell case). In this case, this correction would diverge.

In the off-shell case the W width acts as a natural cutoff for multiple soft-photon interchange between both W's and, as a result, the divergence disappear. However, this effect is particularly significant – approximately +6% – near the W^+W^- production (as the relative velocity v of the W bosons approaches zero at threshold), while negligible for centre-of-mass energies satisfying $\sqrt{s} - 2M_W \gg \Gamma_W$. Higher order Coulomb corrections can be safely neglected ($\ll 1\%$).

Similarly as equation 2.14 the W^+W^- cross-section for off-shell bosons including the Coulomb correction can be expressed as: [22]

$$\sigma(s) = \int_0^s ds_1 \rho(s_1) \int_0^{(\sqrt{s}-\sqrt{s_1})^2} ds_2 \rho(s_2) \sigma^0(s; s_1, s_2)[1 + \delta_C(s; s_1, s_2)]. \tag{2.23}$$

The term $\delta_C(s; s_1, s_2)$ represents the radiative Coulomb correction:

$$\delta_C(s; s_1, s_2) = \frac{\alpha}{v}\left[\pi - 2\arctan\left(\frac{|\kappa|^2 - p^2}{2p\,\Re(\kappa)}\right)\right]$$

where:

$$v = \frac{4p}{\sqrt{s}} = 2\sqrt{1 - \frac{(2s\,(s_1 + s_2) - (s_1 - s_2)^2)}{s^2}} \tag{2.24}$$

$$\kappa = \sqrt{-M_W(E + i\Gamma_W)}, \quad E = \frac{s - 4M_W^2}{4M_W}.$$

The exchange of a soft photon distorts the lineshape of the $W^\pm$ and therefore, affects the direct reconstruction method of measuring the W mass .

Figure 2.3 shows the cross-section for $e^+e^- \to W^+W^-$ in various approximations. In particular, with first order Coulomb corrections.

2.5.2 Initial state radiation

Initital state radiation (ISR) is the most important class of electroweak corrections to the W^+W^- cross-section. It comes from the emission of photons from the incoming e^+ and e^-, and is the reason why the effectively available centre-of-mass energy

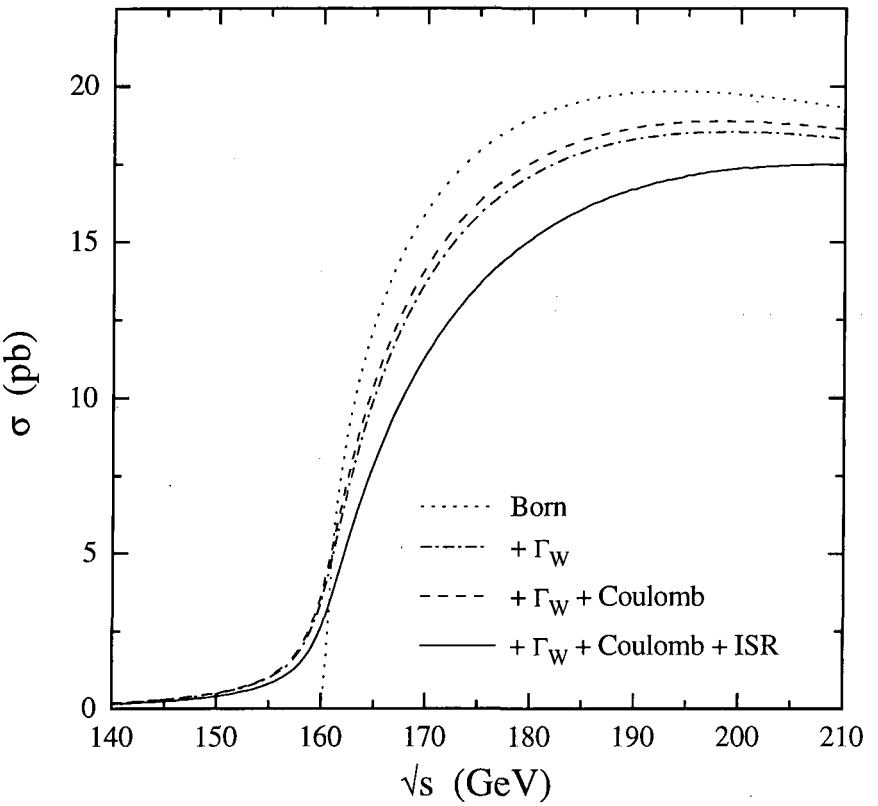

Figure 2.3: The cross-section for $e^+e^- \to W^+W^-$ in various approximations: (i) Born (on-shell) cross-section, (ii) Born (off-shell) cross-section, (iii) with first order Coulomb corrections, and (iv) with initial state radiation.

is lower for the W^+W^- production, thus reducing the cross-section and modifying the mass distributions (see figure 2.3).

The emission of virtual photons leads to divergent corrections (infra-red divergences), compensated for when adding hard photon radiation. The collinear photon radiation off the electron or positron leads to logarithmic corrections $\sim \log(s/m_e^2)$ which can be resumed and incorporated in the cross-section using a 'flux function' or a 'structure function' [12] approach. Both assume that ISR correction factorises.

The ISR corrected cross-section in the flux function (FF) approach is given by:

$$\sigma_{\mathrm{ISR}}(s) = \int_{s_{min}}^{s} \frac{ds'}{s} F(x,s)\sigma(s') \tag{2.25}$$

where s' is the reduced centre-of-mass energy squared, $x = 1 - s'/s$, and σ is given

by Eq. 2.23. The radiator function $F(x,s)$ in the flux approach, is given by:

$$F(x,s) = tx^{t-1}(1+S(s)) + \mathcal{H}(x,s) \tag{2.26}$$

with t containing all mass singularities $\log(s/m_e^2)$:

$$t = \frac{2\alpha}{\pi}\left[\log\left(\frac{s}{m_e^2}\right) - 1\right]. \tag{2.27}$$

The $S(s)$ term comes from soft and virtual photon emission and the $\mathcal{H}(x,s)$ term comes from hard photon emission [25].

2.5.3 Improved Born approximation

Three parameters are sufficient to parametrise the electroweak interactions in the Standard Model. Conventionally the choice is $\{\alpha, G_\mu, M_Z\}$ since these are accurately measured. In this case, M_W is a prediction of the model. Radiative corrections to the expression of the W mass in terms of these three parameters introduce non-trivial dependences on m_t and M_H, and therefore a measurement of M_W provides a constraint on these masses. This choice does not appear to be well suited to the W^+W^- production.

A more appropriate choice of parameters for LEP2 is the set $\{M_W, G_\mu, M_Z\}$ (the so-called G_μ scheme) [26], since in this case M_W is one of the parameters of the model. With the tree level relation:

$$g^2 = 4\pi\alpha\frac{4M_W^2}{\sin^2\theta_W} = 4\sqrt{2}G_\mu M_W^2 \tag{2.28}$$

it can be seen that the dominant t-channel neutrino exchange amplitude, and hence the corresponding contribution to the cross-section, depends only on the parameters M_W and G_μ. In this G_μ scheme there are no large next-to-leading order contributions to the cross-section depending on m_t, either quadratically or logarithmically. It seems to be the most model independent approach when defining the parameters for computing the W^+W^- cross-section.

2.6 Interconnection effects

These effects are due to the fact that the W boson has a width and therefore, the final state may interact (QCD interconnection phenomena and QED interactions)

and may no longer be considered as a superposition of two separate W decays.

In general, QCD and QED inteconnection phenomena affect differently each method of determining the W mass , the direct reconstruction method being more affected than the cross-section method. Only the contribution from the Coulomb interaction between slowly moving W bosons, already described in section 2.5, has a bigger effect in the threshold region, hence in the cross-section method.

A good theoretical knowledge of these effects may be needed in order to be able to have a precise W mass measurement. Therefore, many authors have made an effort to understand these effects better [27] [28].

Specific to the fully hadronic decay channel are QCD interconnection phenomena (the so-called colour reconnection effects) and Bose-Einstein correlations between identical bosons (in practice pions). Both are potential sources of a W mass shift. Although there exist a lot of models for colour reconnection, only those tested in the scope of this thesis are briefly described below.

2.6.1 Colour reconnection

A first attempt to describe the reaction: $e^+e^- \rightarrow W^+W^- \rightarrow q_1\bar{q}_2q_3\bar{q}_4$ would be to assume that the $q\bar{q}$-pair from W^+ forms one colour singlet and that the $q\bar{q}$-pair from W^- forms a second one, and then the two systems parton-shower and hadronise independently of each other. The W-particles, however, exist only for a very short time (as a result of the large W width), therefore the space-time separation between the production points ot the two $q\bar{q}$-pairs is very small , < 0.1 fm, compared to the typical distance scale of hadronisation, ~ 1 fm. In one extreme case the production of the four quarks at the same point could be assumed. Thus, in addition to the original colour dipoles $q_1\bar{q}_2$ and $q_3\bar{q}_4$, it could be possible to form another set of dipoles, namely $q_1\bar{q}_4$ and $q_2\bar{q}_3$. These QCD interconnection phenomena between the W^+W^- decay products −most commonly called colour reconnection− could influence the reconstructed W mass in this hadronic channel.

The picture is complicated by the possibility of gluon emission. It is useful to discuss the wavelength of gluons in different stages of the process. A hard gluon (energy $\gg \Gamma_W$) in the perturbative region (the parton-shower) has a wavelength much smaller than the decay vertex separation and can therefore resolve the two

decay vertices. This is described by perturbative QCD and different reconnection probabilities are expected to be suppressed by factors $1/(N_C^2 - 1)$ yielding small effects [28] [3]. On the other hand, in the hadronisation region, gluon wavelenghts are much larger and might feel the joint action of all four quarks colour charges. As a result, is in the non-perturbative hadronisation region where interference effects might be important.

Studies on these effects cannot be described by perturbative methods, thus fully reliying on specific model-dependent implementations. All the commonly-used models for non-perturbative colour reconnection are based on a space-time picture in which reconnection is a local phenomenon. Objects are formed at the hadronisation stage via a local interaction which may combine products of the two W decays in regions where they overlap. Two classes of models may be distinguished, according to the types of combinations that are permitted. In *singlet* models only colour-singlet objects can be formed whereas in *non-singlet* models there is no such constraint.

All the reconnection models based on string hadronisation proposed by Khoze and Sjöstrand [28] are singlet models, since each string is a colour singlet (reconnections within a W system are not considered). Within this framework three classes of models are investigated:

- model I: After the parton-shower the string-systems are described as spheres and may reconnect with a probability proportional to the volume of overlap of the two independent string-systems. The model contains a free strength parameter that can be modified to give any reconnection probability.
- model II: Strings are considered to have negligible thickness (thin vortex lines) and reconnection may happen when they intersect each other.
- model II': Similiar to model II but reconnection is suppressed if there is no reduction of the total string length.

The reason for these names is the analogy to the two types of superconducting vortices (I and II) which could correspond to colour strings. These three models are implemented in the EXCALIBUR Monte Carlo and used for the systematic studies in the W mass measurement.

[3] N_C is the number of colours.

The main alternative to the string hadronisation model is the cluster model, in which quarks and gluons from the parton showers combine locally into clusters. These clusters are much less extended and less massive objects than strings, typically light enough to decay more or less isotropically into a small number of hadrons each. The most widely used cluster models have also been colour singlet models, in which only singlet combinations of partons (quarks and antiquarks) are allowed to form clusters. This model is implemented in HERWIG [66] and a parameter called PRECO sets the probability for colour reconnection (1/9 as default value).

The only general hadronisation model available at present which includes non-singlet component is that of Ellis and Geiger [29] – called "colour-full" –, which is based on a transport-theoretical treatment of parton showering and cluster formation.

2.6.2 Bose-Einstein correlations

In hadronic decays large number of pions are produced and these bosons must obey Bose statistics. Hence, an enhancement of the production of identical particles at small momentum separation, relative to the hypothetical state of uncorrelated production, is expected (Bose-Einstein effect [30]). Therefore, the softest particles from each W would be "dragged" closer to each other and this would reduce the momentum of the W's. Then an increase of the measured W mass would be expected. On the other hand, there is a prejudice that this cross-talk effect should be small, because it affects the overlapping regions of the jets, i.e. low-energy hadrons, whereas fast hadrons, which are critical for the di-jet masses, should not be affected. The Bose-Einstein correlation radius has been measured at LEP1 to be approximately 0.5 fm.

The problem with estimating such effects is that they are purely quantum mechanical in nature, whereas the Monte Carlo programs used to generate simulated events are based on classical models, dealing with probabilities and not with amplitudes. The simulation approaches adopted fall into two categories: 'local' and 'global'.

The most developed model is of the local type and is implemented in JETSET [31] [32]. In this approach the momenta of identical final state particles are redistributed (shifted) to reproduce the expected two-boson momentum correlations. The main

problem is that the momentum shifts spoil overall energy-momentum conservation and so some momenta of non-identical particles has to be modified in order to compensate for this (the so-called global rescaling procedure). It was found [32] that the implications for the W mass measurement could be quite severe, which would make the hadronic channel essentially useless for the W mass determination. Recent studies on the "local event weighting strategy" [33] with improved algorithms of handling locally energy and momentum conservation indicate a lower uncertainty due to this effect.

Recently, a different approach based on the assignment of a global BE weight w_{BE} to the events according to the momentum distribution of the final state boson has been adopted in order to assess this systematic uncertainty [34]. The method arises very naturally in a quantum-mechanical approach, where the weight can be constructed as the ratio of the square matrix elements of the production process with and without BE, respectively. Such an approach assumes that a model exists for particle production in the absence of Bose statistics. The introduction of a global weight still leaves the door open for intentional or spurious BE effects of a non-local character. The problem is that, even if the correct calculation of the weight function is known, this would be too laborious, involving a sum over all permutations of particles. This has led to the investigation of 'partial symmetrization' procedures that aim to include the most important permutations for each event. Assuming a spherical space-time distribution of the particle source, the correlation function takes the form:

$$C(Q) = 1 + \lambda\rho(Q) \tag{2.29}$$

where Q is the four-momentum difference, $Q^2 = -(p_1 - p_2)^2$, and ρ is the absolute square of the Fourier transofrm of the particle emitting source density, with the normalization condition $\rho(0) = 1$. The incoherence parameter λ takes into account the fact that, for various reasons, the strength for the source density, which leads to:

$$\rho(Q) = exp(-R^2Q^2) \tag{2.30}$$

where R is the source radius.

Other methods that could be found in the literature are outside the scope of this thesis.

2.7 W mass at LEP

The W mass at LEP has been measured since the energy threshold production of W bosons was reached in 1996. Since then, different methods of measuring were used.

(i) **Threshold cross-section measurement** of the process $e^+e^- \rightarrow W^+W^-$. It makes use of the rapid increase of the W^+W^- production cross-section at $\sqrt{s} \sim 2M_W$ to measure the W mass. It relies on the comparison of an absolute cross-section measurement with a theoretical calculation which has M_W as a free parameter. The smallness of the cross-section near the threshold is compensated by the enhanced sensitivity to M_W in this region. Using the 161 GeV energy data collected by the four experiments at LEP, a measurement of the W mass was done using this method and obtaining an error of $220\,\mathrm{MeV}/c^2$.

(ii) **Direct reconstruction** method. Reconstructing the Breit-Wigner resonant shape from the $W^\pm$ final states using kimeatic fitting techniques to improve the mass resolution the W mass can be measured. It makes use of the large W^+W^- statistics at the higher LEP2 energies, $\sqrt{s} \geq 175\,\mathrm{GeV}$. Here, the most important issue is the accurate modeling of the $W^\pm$ lineshape, i.e. the distribution in the invariant mass of the $W^\pm$ decay products. This is the method used in this thesis, and it will be in more detail explained in the following chapters. This method can be used when the energy is higher from the threshold energy.

(iii) **Determination of M_W from the lepton end-point energy**. The end-points of the lepton spectrum in semileptonic decays depend quite sensitively on the W mass . For on-shell W bosons at leading order:

$$E_- \leq E_l \leq E_+, \quad E_\pm = \frac{\sqrt{s}}{4}\left(1 \pm \sqrt{1 - 4M_W^2/s}\right). \tag{2.31}$$

In this case the statistical error on M_W is determined by the statistical error on the measurement of the lepton end-point energy:

$$\Delta M_W = \frac{\sqrt{s - 4M_W^2}}{M_W}\Delta E_\pm. \tag{2.32}$$

However, in practice, the end-points of the distribution are considerably smeared by finite width effects and by initial state radiation, and only a fraction of events close to the end-points are sensitive to M_W. This significantly weakens the statistical power of this method from the naive estimate of equation 2.32. This method has not been used by any of the LEP four experiments because of that.

In the present analysis, only the hadronic channel is used to measure the W mass. A combination of this measurement with that from the semileptonic channel is done in section 6.

Chapter 3

Description of the experiment

The measurement of the W mass presented in this thesis is based on the data produced as a result of e^+e^- collisions at $\sqrt{s} = 172\,\text{GeV}$ and $183\,\text{GeV}$ in the LEP accelerator at CERN and collected by the ALEPH detector. The first section of this chapter will be devoted to a brief description of the LEP collider and mainly focussed on the determination of the beam energy, of crucial importance for this measurement. Then, the ALEPH detector will be briefly described with some stress on the performances relevant to the analysis. Finally, a few words will be devoted to the event reconstruction and simulation processes.

3.1 The LEP collider

The LEP collider (Large Electron Positron collider) [35] is an e^+e^- storage ring of 27 Km of circumference (the largest collider of this kind in the world) sited at the European Centre for Particle Physics (CERN) in Geneva, Switzerland. It is located in a tunnel at a a depth between 80 m and 137 m, spanning the French and Swiss territories (see Fig. 3.1).

The beams that circulate around the ring are formed by bunches of electrons and positrons. They are accelerated in opposite directions and cross in eight or sixteen points in case the number of bunches is four or eight, respectively, although they are steered to collide every $22\,\mu$s (or $11\,\mu$s) only in the four points where the detectors ALEPH [36], DELPHI [37], L3 [38] and OPAL [39] are installed. The collisions in the other points are avoided by a system of electrostatic separators.

The LEP injection chain starts with the LINear ACcelerator (LINAC) which accelerates electrons and positrons in two stages. In a first stage, the electrons are accelerated up to an energy of 200 MeV and part of these electrons are used to produce positrons by collision with a target of tungsten. In a second acceleration stage, both electrons and positrons reach an energy of 600 MeV. These two linear accelerators constitute the LEP Linear Injector (LIL). Then, the particles are injected into a small storage ring of 0.12 Km of circumference, the Electron Positron Accumulator (EPA), where they are separated into bunches and accumulated until the beam intensities achieve the nominal value ($\sim 10^{10}$ particles). Afterwards, the bunches are injected into the Positron Synchroton (PS) storage ring, of 0.6 Km of circumference, where they achieve an energy of 3.5 GeV and then, into the Super Proton Synchroton (SPS) storage ring, of 7 Km of circumference, reaching an energy of 20 GeV. Finally, the particles are injected into the LEP main ring where they are accelerated till the collision energy.

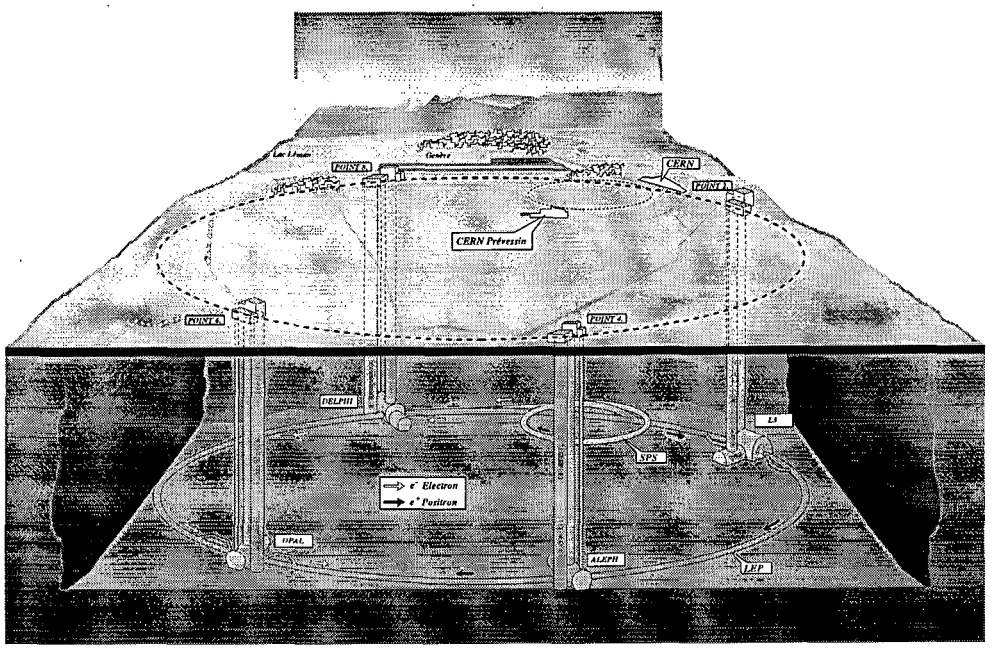

Figure 3.1: View of the LEP ring and the four interaction points.

Since the $e^{\pm}$ trajectory is curved, there is an important loss of energy in the form of synchroton radiation. The average energy loss is proportional to E^4/m^2R, where E is the particle energy, m the particle mass and R the radius of curvature. Then, it is very important for $e^{\pm}$ at high energy and becomes manageable only if the radius of the machine is sufficiently large. This loss of energy is compensated for by means of cavities of radiofrequency (RF), which provide an extra-acceleration.

During a first phase of the accelerator programme (LEP1), finished in 1995, the LEP machine has been operated at a centre-of-mass energy of $\sim 91\,\mathrm{GeV}$, at the peak of Z production, with luminosities at the level of $1 - 2 \times 10^{31}\,\mathrm{cm^{-2}s^{-1}}$ and producing around 4 million visible Z decays per experiment. Since November 1995, in order to increase even more the luminosity, a new scheme consisting in having four trains of up to four bunches colliding at each interaction point has been adopted. This scheme is expected to achieve luminosities in excess of $10^{32}\,\mathrm{cm^{-2}s^{-1}}$ in order to compensate somehow for the expected small cross-sections during the LEP2 phase. This second phase of the LEP programme started in summer 1996, when e^+e^- collisions at a centre-of-mass energy of $\sqrt{s} = 161\,\mathrm{GeV}$ and then at 172 GeV where produced for first time. In order to achieve this energy and compensate for the increased synchroton radiation, new niobium superconducting RF cavities had to be installed, partially replacing the old room temperature copper cavities. During 1997, the e^+e^- collisions where produced at $\sqrt{s} = 183\,\mathrm{GeV}$ and it is expected to increase the energy up to $\sqrt{s} = 189\,\mathrm{GeV}$ during 1998 with the installation of more superconducting cavities. A total integrated luminosity per experiment of about $500\,\mathrm{pb^{-1}}$ is expected to be collected during the whole LEP2 phase.

3.1.1 Determination of the beam energy

During the LEP1 phase, the highest precision measurement performed at LEP was precisely the determination of the beam energy. This allowed the determination of m_Z and Γ_Z with an unprecedented precision. As it will be seen, at LEP2 there are intrinsic limitations in the application of the successful technique applied in LEP1, which has to be combined with other techniques, ending up with a much worse beam energy determination.

Since 1992 and before LEP2, the method used to measure the beam energy was taking advantage of the fact that, under favourable conditions, transverse beam

polarisation can be built up in a circular machine due to the interaction of the electrons with the magnetic guide field (Sokolov-Ternov effect [42]). The number of spin precessions in one turn around the ring ("spin tune") is:

$$\nu = \frac{g_e - 2}{2}\frac{E_{beam}}{m_e} = \frac{E_{beam}(\mathrm{GeV})}{0.4406486(1)}$$

where g_e is the gyromagnetic constant and m_e is the electron mass. This relation is exact only for ideal storage rings and needs to be corrected for small imperfections. In this approximation, the spin precession frequency is equal to:

$$f_{prec} = \nu f_{rev}$$

with f_{rev} being the revolution frequency, which in typical conditions take the value $f_{rev} = 11245.5041(1)$ Hz. From the above equations, it is clear that this spin precession frequency (f_{prec}) is predicted with a very high accuracy as a function of the beam energy. On the other hand, this frequency can be measured using a sweeping kicker magnet which produces an exciting field perpendicular to the beam axis and in the horizontal plane. Then, when $f_{spin-kick} = (n \pm \nu) f_{rev}$ (n integer), that is when the exciting field is in phase with the spin precession, the spin rotations about the radial direction add up coherently from turn to turn. About 10^4 turns (~ 1 s) are needed to turn the polarisation vector into the horizontal plane (resonant depolarisation). In this way, by plotting the measured beam polarisation versus $f_{spin-kick}$, one can determine f_{prec} with a precision which corresponds to an accuracy on the beam energy at the level of 0.2 MeV. This method is often referred to as *energy calibration by resonant depolarisation* and has been extensively used for accurate beam energy calibrations and measurements of particle masses [43]. However, only two calibrations per week are in practice feasible, and the extrapolation between them is affected by errors coming from the status of the RF cavities, the temperature and humidity in the LEP tunnel, the distortions of the ring length (because e.g. of the tidal forces of the sun and the moon) and even by the current flow over the vacuum chamber created by trains travelling between the Geneva main station and destinations in France. The final precision of the measurement improves as these effects are understood and in LEP1 was at the level of 1.5 MeV.

However, at LEP2 the application of the above technique is limited by the fact that at a beam energy $E_{beam} \geq 80.5$ GeV the beam transverse polarisation can not be maintained. Therefore, the absolute energy scale at $E_{beam} = 80.5$ and 86 GeV

has been obtained by performing depolarisation measurements at $E_{beam} = 45$ and 50 GeV and extrapolating to higher energies by making use of the instantaneous measurements performed by nuclear magnetic resonance (NMR) probes installed in 16 dipole magnets. This calibration procedure assumes a linear behaviour (with zero intercept) of the NMR probes response as a function of the beam energy. In addition, the beam energy as determined by the NMR probes is compared to the one determined from the measurement of the magnetic field in the LEP dipoles ("flux-loop").

The estimated uncertainty in the determination of the beam energy is $\pm 27(30)$ MeV at $E_{beam} = 80.5(86)$ GeV, about 10 times larger than at LEP1 ! The different contributions to this uncertainty are summarised in Table 3.1 [44].

ΔE_{beam}[MeV] $E_{beam} =$	80.5 GeV	86 GeV
Energy scale uncertainties:		
Polarisation systematics	1	1
Energy difference e^+e^-	2	2
Fill-to-fill variations	10	5
Extrapolation	24	29
Beam-orbit corrections	1	1
Variations in a fill:		
Tidal forces model	1	1
NMR/temperature	2	2
Specific corrections at IP:		
Dispersion	1	1
RF	5	5
Total	27	30

Table 3.1: Different contributions to the uncertainty on the beam energy determination.

3.2 The ALEPH detector

The ALEPH detector is located at the experimental point number 4 in a cavern 143 m under the surface. It is a 12 m diameter by 12 m length cylinder positioned around the beam pipe, a tube of 10 cm of radius that forms part of the accelerator. In the ALEPH reference system, the z direction is around the beam pipe, positive in

the direction followed by the e^-, thereby slightly different from the local horizontal direction due to the fact that the accelerator is slightly tilted. The positive x direction points to the centre of LEP, and is horizontal by definition. The positive y direction is orthogonal to z and x and deviates 3.5875 mrad from the local vertical direction.

The detector consists of subdetectors, each of one specialised in a different task. The tracking devices allow to reconstruct the trajectories of charged particles and to classify them using the ionisation left in the detectors. The electromagnetic and hadronic calorimeters give a measurement of the energy of the particles, being also the only detector capable to give position information for the neutral particles. Muons are identified using the muon chambers and/or the final planes of the hadronic calorimeter. Specialised detectors situated at low angle give a precise measurement of the luminosity. Some other subdetectors monitor the luminosity and the background. Finally, the trigger and data acquisition system is used to manage everything and record useful information. A brief description of these devices follows, mainly stressing their performances [41], since a detailed and complete description can be found elsewhere [36, 40].

A particle leaving the interaction point would encounter the following subdetectors (see Fig. 3.2):

- **Mini Vertex DETector (VDET):** fully operational since end 1991, is a double sided silicon strip device with two layers of strips parallel (z) and perpendicular ($r\phi$) to the beam, situated around the beam pipe, providing a very accurate vertex tagging of tracks coming from the interaction point. The coordinate spatial resolution is $10\,\mu$m in $r\phi$ and $13\,\mu$m in z. It plays a very important rôle in the reconstruction of particles with very short lifetime, like hadrons containing the b or c quarks or the τ lepton, through the accurate measurement of the impact parameter of their charged decay products.

- **Inner Tracking Chamber (ITC):** is a cylindrical multiwire drift chamber. It contributes to the global ALEPH tracking and is also used for the triggering of charged particles coming from the interaction region. It can provide up to eight precise $r\phi$ coordinates per track, with an accuracy of $100\,\mu$m per coordinate.

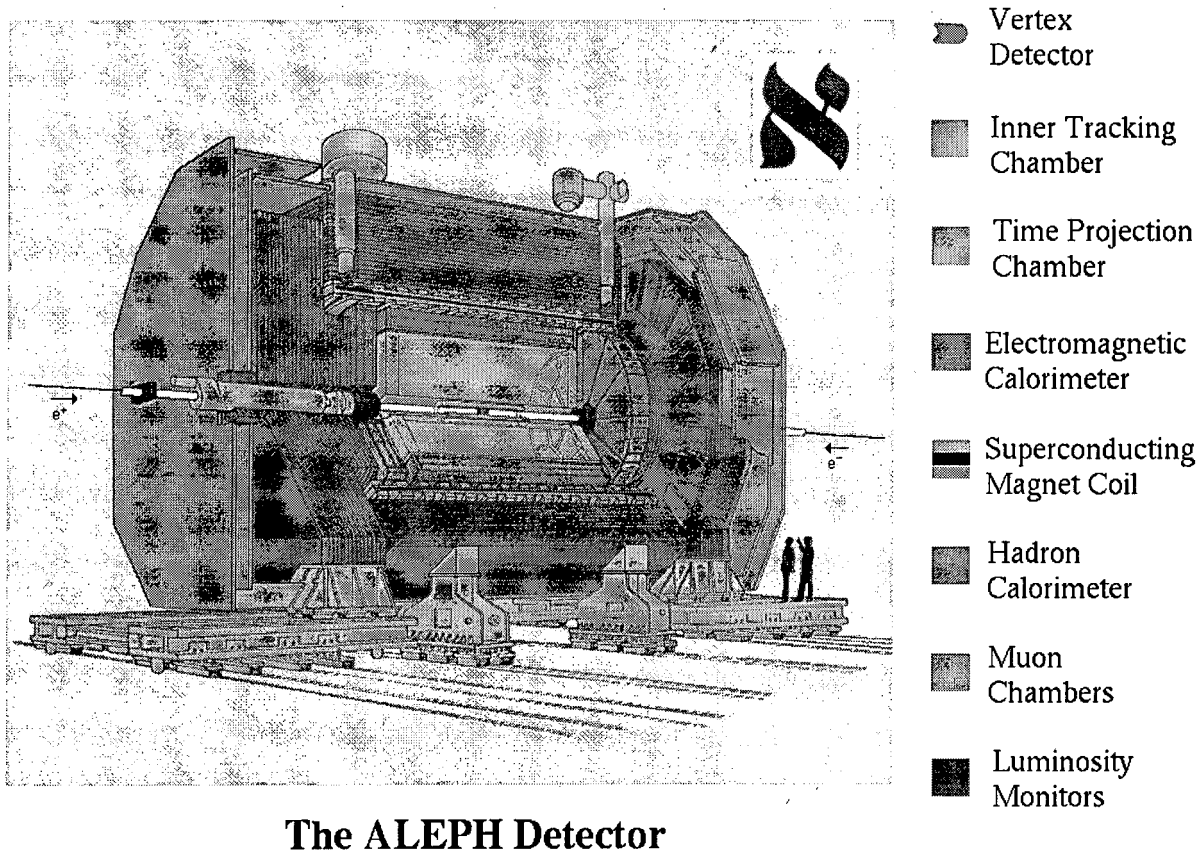

Figure 3.2: The ALEPH detector.

- **Time Projection Chamber (TPC):** the central track detector of ALEPH, is a very large three-dimensional imaging drift chamber. It provides up to 27 three-dimensional coordinate points for each track. The single-coordinate resolution is 173 μm in the azimuthal direction and 740 μm in the longitudinal direction. From the curvature of tracks in the magnetic field, the TPC gives a measurement of transverse particle momenta, p_T, with an accuracy of $\Delta(1/p_T) = 0{:}6 \times 10^{-3}\,(\mathrm{GeV/c})^{-1}$ at 45 GeV, if used together with the ITC and the VDET. The chamber also contributes to charged particle identification through measurements of energy loss (dE/dx) derived from the about 340 samples of the ionisation for a track traversing the full radial range.

- **Electromagnetic CALorimeter (ECAL):** is a sampling calorimeter con-

sisting of alternating lead sheets and proportional wire chambers read out in projective towers and longitudinally segmented in three compartments. A granularity of about $1^\circ \times 1^\circ$ is obtained. The ECAL measures the energy and position of electromagnetic showers. The energy resolution is $\sigma(E)/E = 0.16/\sqrt{E/\mathrm{GeV}} + 0.009$. The high position and energy resolution achieved lead to good electron identification and allow to measure photon energy even in the vicinity of hadrons.

- **Superconducting coil:** is a liquid-Helium cooled superconducting solenoid creating, together with the iron yoke, a 1.5 T axial magnetic field in the central detector.

- **Hadronic CALorimeter (HCAL):** is a sampling calorimeter made of layers of iron and streamer tubes. It measures energy and position for hadronic showers and, complemented with the muon chambers, acts as a muon detector. The energy resolution for a charged pion is $\sigma(E)/E = 0.85/\sqrt{E/\mathrm{GeV}}$. The readout is performed twice: using cathode pads forming projective towers and using digital readout of the streamer tubes for muon tracking and also for triggering. It also provides the main support of ALEPH, the large iron structure serving both as hadron absorber and as a return yoke of the magnet.

- **MUON chambers (MUON):** outside HCAL, are two double layers of limited streamer tubes which measure position coordinates of muons, the only detectable particles reaching this subdetector.

An accurate luminosity measurement is required for the precise measurement of cross-sections. This is provided by four detectors for small angle Bhabha scattering installed around the beam pipe:

- **Luminosity CALorimeter (LCAL):** is a lead/wire calorimeter similar to ECAL in its operation. It consists of two pairs of semi-circular modules placed around the beam pipe at each end of the detector. At LEP2, it provides the "official" ALEPH luminosity. Its acceptance in polar angle goes from 45 to 160 mrad, which corresponds to a Bhabha cross-section of about 59 nb at 161 GeV. The luminosity measurement consists essentially in "counting" the number of events for which there has been two back-to-back deposits of

energy compatible with the beam energy. The luminosity is obtained from the normalisation of the number of events observed to the theoretical cross-section (computed with the programme BHLUMI [45]) taking into account the experimental acceptance. The statistical and systematic errors in the luminosity measurement are respectively 0.4% and 0.6%. The systematic error includes a theoretical error in the cross-section calculation of 0.11%.

- **SIlicon luminosity CALorimeter (SICAL):** was installed in September 1992 on each side of the interaction region. It uses 12 silicon/tungsten layers to sample the showers produced by small angle Bhabhas. During the LEP1 phase, it provided the "official" ALEPH luminosity since it improved the statistical precision of the luminosity measurement by sampling at smaller angles than LCAL. The systematic error on the luminosity was also reduced thanks mainly to the greater precision in the positioning of its components. At LEP2, it is not used anymore to provide a luminosity measurement because it is partially "hidden" by the masks installed to protect the central detectors from the synchroton radiation, much higher than at LEP1. Instead, it is used to improve the ALEPH acceptance at very low angle.

- **Bhabha CALorimeter (BCAL):** located behind the final focus quadrupoles, it gives a measurement of the instantaneous luminosity and acts as a background monitor. Being sited at lower angles, allows to have high statistics at the cost of increased systematic errors. It is a sampling calorimeter made of tungsten converter sheets sandwiched with sampling layers of plastic scintillator. A single plane of silicon strips with $r\phi$ segmentation is used to locate the shower position.

The optimisation of the LEP performance needs also some monitoring of the beam conditions which is accomplished by:

- **Small Angle Monitor of BAckground (SAMBA):** is positioned in front of LCAL at either end of the detector. It consists of two multi-wire proportional chambers at each end, read out in two rings of 8 pads per ring. It is used as a background monitor.

- **Beam Orbit Monitors (BOMs):** located around the circumference of LEP, they measure the mean position and angle of the beam orbits which are used

by LEP to optimise the beam conditions, and by ALEPH to determine the (x, y) position of the beam spot as a starting point for offline reconstruction of the primary vertex.

Not all the collisions that take place at LEP are useful for the physics that ALEPH is willing to study. The large amount of useless events have to be filtered out in order to avoid inefficiencies in the detector and a large amount of unused data. The purpose of the trigger system is to produce a signal that starts the readout of the events. It is desirable to keep all the e^+e^- collisions and to reduce as much as possible the rate of background events. The trigger system has been organised in a three-level system:

- The **level one** decides whether or not to read out all the detector elements. Its purpose is to operate the TPC at a suitable rate. The decision is taken approximately 5 μs after the beam crossing from pad and wire information from ECAL and HCAL and hit patterns from the ITC. The level one rate must not exceed a few hundred Hz. If the decision is not to take the event, the TPC is reset and kept ready for the next event.

- The **level two** refines the level one charged track triggers using the TPC tracking information. If the level one decision can not be confirmed, the readout process is stopped and cleared. The decision is taken approximately 50 μs after the beam crossing (the time at which the TPC tracking information is available). The maximum trigger rate allowed for level two is about 10 Hz.

- The **level three** is performed by software. It has access to the information from all detector components and is used to reject background, mainly from beam-gas interactions and off-momentum beam-particles. It ensures a reduction of the trigger rate to 3-4 Hz, which is acceptable for data storage.

This trigger scheme has to be rather flexible since it has to be able to reject the background and keep signals from possible new physics events. Therefore, the available electronic signals from different ALEPH detector components allow for a variety of triggers which, together, cover all possible types of events.

The data acquisition (DAQ) system allows each subdetector to take data independently, process all the information taken by the detector, activates the trigger

system at every beam crossing, writes the data in a storage system and monitorises and regulates continuously all the detector and electronic system.

The DAQ [46] architecture is highly hierarchical. Following the data and/or control flow from the bunch crossing of the accelerator down to the storage device, the components found and their tasks are briefly described below:

- Timing, Trigger and Main Trigger Supervisor: synchronise the readout electronics to the accelerator and inform the ReadOut Controllers (ROCs) about the availability of the data.

- ROCs: initialise the front-end modules, read them out and format the data.

- Event Builders (EBs): build a subevent at the level of each subdetector and provide a "spy event" to a subdetector computer.

- Main Event Builder (MEB): collects the pieces of an event from the various EBs and ensures resynchronisation and completeness.

- Level Three Trigger: as seen, performs a refined data reduction.

- Main host and subdetector computers: the main machine (an AXP cluster) initialises the complete system, collects all data for storage and provides the common services. The subdetector computers get the "spy-events" and perform the monitoring of the large subdetectors (TPC, ECAL, HCAL).

The data taken by the online computers is called raw data and is reconstructed quasi online. In less than two hours after the data is taken, the event reconstruction and a check of the quality of the data is done, thus allowing ALEPH to have a fast cross-check of the data and correct possible detector problems. This task is performed by the Facility for ALeph COmputing and Networking (FALCON) [47].

The year by year continuous increase of CPU power of the machines has made the hardware and software of FALCON develop in order to accommodate to the available performance and requirements. In its current configuration, FALCON consists of three processors (three DEC-AXP machines). Each of the processors runs the full ALEPH reconstruction programme JULIA (Job to Understand Lep Interactions in ALEPH) [48] which, for each event of the raw data file, processes

all the information from the different subdetectors. Other programmes also run to compute the drift velocity in the TPC (PASS0), or to analyse the quality of the data taken (RunQuality).

After their reconstruction, the events are written in POT (Production Output Tape) data files and transmitted to the CERN computer centre where they are converted into different data types more suitable for physics analysis. In this work, the ALPHA (ALeph PHysics Analysis) [49] package has been used, as an interface that allows an easy access to the reconstructed physical quantities of particles: momenta, energies, etc.

3.3 Event reconstruction and simulation

In this section, the reconstruction processes more relevant to the analysis are briefly explained, together with the description of the different Monte Carlo codes used to generate simulated events.

3.3.1 Tracking in ALEPH

Tracks are reconstructed starting in the TPC: nearby hits are linked to form track segments and the segments are connected to make tracks by requiring consistency with a helix hypothesis. These track candidates are then extrapolated to the inner detectors where consistent hits are assigned. Coordinate errors are determined using the preliminary track parameters. The final track fit, based on Kalman filter [50] techniques, uses these errors and takes into account multiple scattering effects between each measurement.

Monte Carlo studies on hadronic Z events indicate that 98.6% of tracks that cross at least four pad rows in the TPC are reconstructed successfully; the small inefficiency, due to track overlaps and cracks, is reproduced to better than 0.1% by the simulation. The efficiency of associating a vertex detector hit to an isolated track is about 94% per layer, within the geometrical acceptance. By selecting dimuon events at 45 GeV in the angular acceptance $|\cos\theta| < 0.8$, the transverse momentum resolution is $\sigma(1/p_T) = 1.2\times10^{-3}\,(\mathrm{GeV/c})^{-1}$ for the TPC alone, whereas it improves up to $\sigma(1/p_T) = 0.6\times10^{-3}\,(\mathrm{GeV/c})^{-1}$ when VDET, ITC and TPC are

used together.

3.3.2 Energy flow determination

The simplest way to determine the energy flow of an event recorded in the ALEPH detector is to make the sum of the raw energy found in all calorimetric cells without performing any particle identification. This method yields a resolution of $\sigma(E) = 1.2\sqrt{E/\mathrm{GeV}}$ for hadronic Z decays. The energy flow algorithm [41] improves this resolution by making use of the track momenta and taking advantage of the photon, electron and muon identification capabilities.

A first cleaning procedure is applied to eliminate poorly reconstructed tracks, V^0's not compatible to originate from the nominal collision point, and noisy channels and fake energy deposits in the calorimeter towers. After the cleaning, the charged particle tracks are extrapolated to the calorimeters and groups of topologically connected tracks and clusters (so-called "calorimeter objects") are formed. From each calorimeter object are removed: charged particles identified as electrons (together with the energy contained in the associated electromagnetic calorimeter towers), charged particles identified as muons and photons and π^0's. At this stage, the only particles left in the calorimeter object should be charged and neutral hadrons. All charged particle tracks coming from the nominal interaction point or belonging to a reconstructed V^0 are counted as charged energy assumed they are pions. Neutral hadrons are identified as a significant excess of calorimetric energy.

As a result of the energy flow algorithm, a set of "energy-flow objects" (electrons, muons, photons, charged or neutral hadrons) is obtained, all of them characterised by their four-momenta. To this list are added all the clusters found in the luminosity monitors, where no particle identification is available. This list is expected to be a close representation of the stable particles actually produced in the collision. Neutrinos, which escape undetected, are indirectly detected by the presence of significant missing energy in the event.

As a result of the energy flow algorithm, the energy resolution, as measured on hadronic Z decays, can be described by the following parametrisation:

$$\sigma(E) = (0.59 \pm 0.03)\sqrt{E/\mathrm{GeV}} + (0.6 \pm 0.3)\ \mathrm{GeV},$$

which represents a big improvement with respect to what is obtained from the calorimeters alone.

3.3.3 Event simulation

In order to evaluate background contaminations, compute acceptances and efficiencies and, in general, compare the theoretical models to the experimental prediction, Monte Carlo simulated events are generated. The chain to produce simulated events is the following:

- Generation of event kinematics. The particle four-momenta are generated according to the different physics processes. In ALEPH, the different Monte Carlo codes to generate each physics process have been unified through the common interface KINGAL [51].

- Simulation of the detector response. This is done by using a GEANT [52] based programme, GALEPH [53], where all information about the geometry and materials involved in the experimental setup are described. For the tracking simulation, the primary long-lived particles are followed through the detector. Secondary particles are also produced by interaction with the detector material. GEANT and GHEISHA [54] are used to simulate, respectively, the electromagnetic and nuclear interactions of particles with matter. The energy depositions are converted into measurable signals.

- Reconstruction. The same reconstruction programme (JULIA) used for the real data is used in the simulated events. Thus, the output of all the simulation processes has the same format as for the real data.

The Monte Carlo codes used to generate (at each centre-of-mass energy) the physics processes relevant to this analysis are briefly described below.

Two Monte Carlo event generators were used to simulate the signal events, i.e. four fermion final states which can come from WW production and decay:

- KORALW, version 1.21 [55]. This programme includes multiphoton initial state radiation with finite photon transverse momentum via Yennie-Frautschi-Suura exponentiation [56], final state radiation via PHOTOS [57] and Coulomb

correction [58]. It can generate CC03 diagrams only, or include four-fermion diagrams computed with the GRACE package [59], with fixed W and Z widths. The JETSET [60] package takes care of gluon radiation and hadronisation; no colour reconnection effects are included. In four-quark final states the colour flow is chosen with probabilities proportional to the matrix elements squared for WW and ZZ production [61], [62].

- For comparison, the EXCALIBUR [?] generator was used, which can generate all diagrams (at tree-level) contributing to a given four-fermion final state). It includes initial state radiation collinear with the beams, final state radiation via PHOTOS, Coulomb correction and hadronisation by JETSET. In four-quark final states the same choice of colour flow as above is made.

At 172 GeV, samples of 100000 WW events were generated with KORALW with three different values of the W mass: 79.25, 80.25 and 81.25 GeV/c^2 for all four-fermion (WW-like) diagrams. Seven additional samples of 20000 events were generated with W masses of 79.25, 79.75, 80.00, 80.25, 80.50, 80.75 and 81.25 GeV/c^2. A comparison sample was generated with EXCALIBUR with 80.25 GeV/c^2 for all four-fermion diagrams. In order to assess the impact of colour reconnection effects, the same events (at the parton level) where hadronised following the colour reconnection Ansatz of [65].

In the generation of WW Monte Carlo with four-fermion diagrams, loose cuts are applied on the outgoing electron angle or the fermion-antifermion invariant masses in order to avoid regions of phase space with poles in the cross-section. Signal events produced in these regions would in any case be rejected by the selection cuts.

Monte Carlo samples corresponding to integrated luminosities at least twenty times as large as that of the data where generated and fully simulated for all relevant background reactions. Annihilation into quark pairs, $e^+e^- \rightarrow q\bar{q}(\gamma)$, was mainly simulated with PYTHIA [60] although, in order to assess the systematic effect of a different hadronisation model, a sample of events using HERWIG 5.8d [66] was also generated. Tagged two photon ($\gamma\gamma$) reactions into leptons and hadrons were generated with PHOT02 [67], whereas those hadronic untagged were generated with PYTHIA. Dileptons final states were generated with KORALZ [68] and UNIBAB [69]. Finally, PYTHIA was also used for various processes leading to four-fermion final states such as: ZZ, Ze^+e^-, $Z\nu\bar{\nu}$ and $We\nu$. To avoid double-counting of

four-fermion events between the signal and background Monte Carlos, events with a flavour content that could originate from WW production were explicitly removed from the background samples.

Chapter 4

W mass measurement at 172 GeV

4.1 Introduction

This chapter is devoted to describe the W mass measurement using the hadronic channel and the integrated luminosity of $10.65\,\mathrm{pb}^{-1}$ data taken by ALEPH at a mean centre-of-mass energy of 172.09 GeV. The first section is devoted to explain the event selection. The second and third sections are devoted to the jet clustering algorithm and the kinematical fit. The jet pairing is explained in the forth section. The mass extraction method comes afterwards, as well as the results, Monte Carlo checks and the systematic studies.

4.2 Monte Carlo samples

The W mass is extracted by comparing the experimental distributions to the corresponding Monte Carlo distributions, where generated events are processed through a full simulation of the ALEPH detector response and through the same reconstruction chain (explained in chapter 3). Two Monte Carlo event generators are used to simulate the signal events, i.e. four-fermion final states which can come from $\mathrm{W^+W^-}$ production and decay:

- `KORALW`, version 1.21 [55]. This program includes multi-photon initial state radiation with finite photon transverse momentum via Yenni-Frautschi-Suura

exponentiation [56], final state radiation via PHOTOS [?],and Coulomb correction [21]. It can generate CC03 diagrams, which correspond to the three Feynman diagrams that contribute to the production of two resonant W's at tree level, or include four-fermion diagrams computed with the GRACE package [?], with fixed W and Z^0 widths. The JETSET package [60] takes care of gluon radiation and hadronisation. In four-quark final states, the colour flow between fermions is chosen with probabilities proportional to the matrix elements squared for W^+W^- and Z^0Z^0 production [?]. Colour flow between two fermions produced by two different bosons, known as colour reconnection (section 2.6.1) is not included. Samples of 100000 events were generated with W masses of 79.25, 80.25 and 81.25 GeV/c^2, for all four-fermion diagrams. Loose cuts were applied at the generation level on the outgoing electron angle of the fermion-antifermion pair invariant masses, avoiding regions of phase space with poles in the cross-section . Signal events produced in these regions would in any case be rejected by the selection cuts. Seven additional samples of 20000 events each were generated with W masses of 79.25, 79.75, 80.0, 80.25, 80.50, 80.75 and 81.25 GeV/c^2 for all four-fermion diagrams.

- For comparison, the EXCALIBUR generator [63] is also used. It includes ISR collinear with the beams [64], fainl state radiation via PHOTOS [57], Coulomb Correction [21] and hadronisation by JETSET [60]. A sample was generated with $M_W = 80.25\,\mathrm{GeV}/c^2$ and the same choice of colour flow with loose cuts applied at the generation level as above. For colour reconnection studies the same events were hadronised follosing the ansatz of [65].

Monte Carlo samples, with integrated luminosities corresponding to at least twenty times that of the data, were fully simulated for all background reactions. Annihilation into quark pairs, $e^+e^- \rightarrow q\bar{q}(\gamma)$, was simulated with PYTHIA. Two-photon ($\gamma\gamma$) reactions into leptons and hadrons were simulated with the PHOTO2 [67] and PYTHIA generators. Some four-fermion configurations are found in both the signal W^+W^- and background Z^0Z^0 Monte Carlo's. Hence, events with a flavour content that could originate from W^+W^- production are explicitely rejected from the Z^0Z^0 sample.

4.3 Event selection

The W^+W^- events in the hadronic channel (45.5% of all W^+W^- events) are characterized by a high average multiplicity of charged tracks, spherical four-jet like topology and large visible energy, close to the available centre-of-mass energy. The global event topology consists of four (or more) high energetic jets originated from the underlying four-quark structure.

The main source of background to the $e^+e^- \rightarrow W^+W^- \rightarrow 4q$ process is the $e^+e^- \rightarrow Z^0/\gamma \rightarrow q\bar{q}(\gamma)$ production. Fortunately about 70% of these events are affected by hard initial state radiation photon emission which boosts the effective two-quark centre-of-mass energy back to the Z^0 mass (radiative return to the Z^0 events). Such events are characterized by having high missing energy and low invariant mass clustered around the Z^0 mass or, if the γ is detected, a very high energetic γ. In addition, these events tend to have a two-jet structure resulting in a more longitudinal topology, different from the spherical four-jet like topology of the hadronic W's. Additional less important backgrounds come from $e^+e^- \rightarrow Z^0Z^0$ events and, even less important, $e^+e^- \rightarrow Z^0ee$ and $e^+e^- \rightarrow W^+W^- \rightarrow 2q\ell\nu$ events.

The purpose of the different steps in the selection is to remove events originated from processes other than hadronic W^+W^- while keeping high efficiency for the hadronic events.

The initial selection requirements are the so-called class 16 requirements [70], which constitute a minimum set of cuts based entirely on charged tracks measured by the TPC to ensure that the event is well detected. The events are required to have at least five good tracks [1] in the TPC, and the total energy of all TPC good tracks should have more than 10% of the nominal centre-of-mass energy. These cuts reduce the number of beam-gas, beam-beampipe, cosmic ray and leptonic events in the data set.

After these initial requirements, a preselection in order to reject the main backgrounds is applied. It consists of the following cuts:

i. The missing energy must be smaller than 40 GeV;

[1] A good track must have at least four hits in the TPC, must be originated from within a cylinder with radius 2 cm and length 10 cm, centred arount the interaction point, and its polar angle θ must satisfy $|\cos\theta| < 0.95$.

ii. The number of energy-flow objects (defined in 3.3.2) larger than 45;

iii. The number of jets found with the JADE [71] algorithm with $y_{cut} = 0.005$ [2] must be larger than three.

The events are then forced into four jets using the DURHAM-P jet clustering algorithm (see Appendix A.1). Further preselection cuts are applied to these DURHAM jets:

iv. Each jet must contain at least two good tracks;

v. The fraction of electromagnetic to total energy in a jet must be smaller than 0.9.

To extract the W^+W^- signal with high purity and efficiency, the main selection is based on the output of a feed forward neural network (described in appendix A.4) with 21 input variables – chosen to optimise the selection efficiency –, 17 hidden units and one output unit (21-17-1). The output of the neural network peaks at plus one for signal events and at minus one for background events. Detailed explanations can be found in Ref. [75]. The input variables are related to: global event properties, flavour tagging to reduce the background from events containing b quarks, properties of jets, and kinematic variables. The most important ones to select W^+W^- hadronic events are global event quantities like the total visible energy, followed by jet properties.

The full set of variables is listed below, together with their discriminant power (defined in Appendix A.4):

Global event properties (definitions in A.2):

– Total visible energy in the event; (4.7%)
– Sum of momenta of all charged tracks in the event; (2.6%)
– Aplanarity; (4.7%)
– Oblateness; (3.8%)
– Fox-Wolfram moment H0; (3.8%)
– Fox-Wolfram moment H2; (5.4%)
– Fox-Wolfram moment H3; (7.0%)

[2] The y_{cut} is defined to be the cut-off "distance" from which different clusters are not combined into the same jet. For a detailed explanation see appendix A.1.

– Fox-Wolfram moment H4. (6.8%)

Heavy Flavour tagging:

– Sum of the b-tag probabilities [3] for the four jets; (4.8%)
– Sum of logarithms of the b-tag probabilities for the four jets; (4.5%)
– Global b-tag probability, constructed from all charged tracks in the event. (2.6%)

Properties of Jets:

– Number of energy-flow objects in the most energetic jet; (5.4%)
– Number of energy-flow objects in the least energetic jet; (3.6%)
– Largest energy fraction carried by one energy-flow object in the most energetic jet; (3.8%)
– Largest energy fraction carried by one energy-flow object in the second most energetic jet; (4.8%)
– Largest energy fraction carried by one energy-flow object in the third most energetic jet; (3.9%)
– Largest energy fraction carried by one charged track in the most energetic jet. (3.5%)

W^+W^- Kinematics:

– Sum of the cosines of the six angles between the jets; (9.2%)
– Largest of the smallest di-jet invariant masses from each of the three possible pairings; (6.1%)
– Largest invariant mass of all six di-jet combinations; (5.8%)
– Transverse momentum of the highest energetic jet. (3.7%)

Figure 4.1 shows the neural network output for hadronic W^+W^- events (generated at $M_W = 80.25\,\mathrm{GeV}/c^2$) and background ($q\bar{q}(\gamma)$ and Z^0Z^0) events. By requiring the neural network output larger than -0.3, $W^+W^- \rightarrow 4q$ events are selected with an efficiency of 82.3% and a purity of 78.5%.

[3] The b-tag probability of an ensemble of charged tracks is the product of the probabilities that each track comes from the primary vertex [76]. (b-jets have small probabilities).

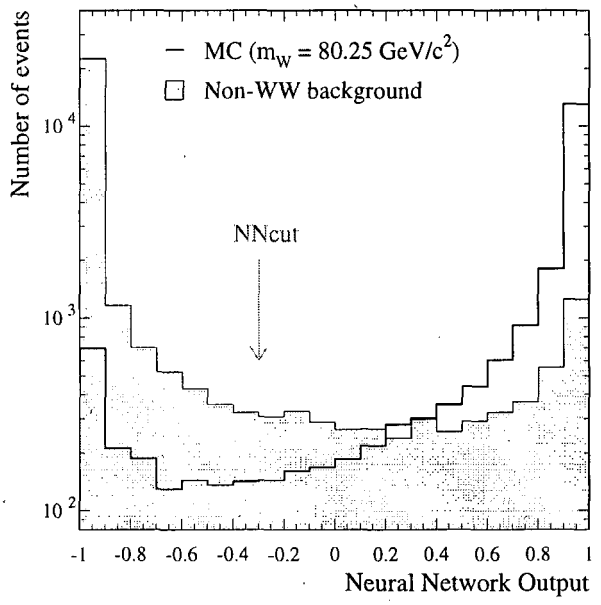

Figure 4.1: Neural network output for signal events generated with a $M_W = 80.25\,\mathrm{GeV}/c^2$ (open histogram) and background events – $q\bar{q}(\gamma)$, Z^0Z^0 – (full histogram). Both histograms are normalised to the same luminosity. The arrow indicates where the cut to select $e^+e^- \rightarrow W^+W^- \rightarrow 4q$ events is applied to the neural network output: -0.3.

By doing different cuts on the neural network output, figure 4.1 showing the purity versus the efficiency is obtained. The arrow shows the cut -0.3 applied to the neural network output. The optimization of the cut will be discussed in section 4.8.

A good performance of a neural network has to select hadronic W^+W^- events with an efficiency independent of the W mass. This is what figure 4.3 shows: the selection efficiency computed using fully reconstructed 4f KORALW Monte Carlo as a function of the W mass is more or less constant.

The number of events surviving the class 16 requirements and the number surviving the neural network cut are summarised in table 4.2 for the different W^+W^- channels and in table 4.3 for the different background processes considered. From these tables, it is obvious that sources of background other than $q\bar{q}(\gamma)$ and Z^0Z^0 are negligible after the selection step.

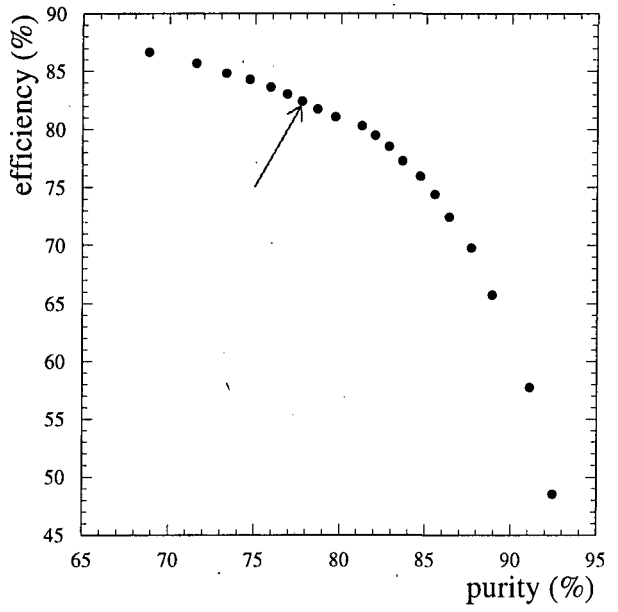

Figure 4.2: Signal efficiency versus purity of the neural network. The arrow indicates where the cut to the neural network output is applied.

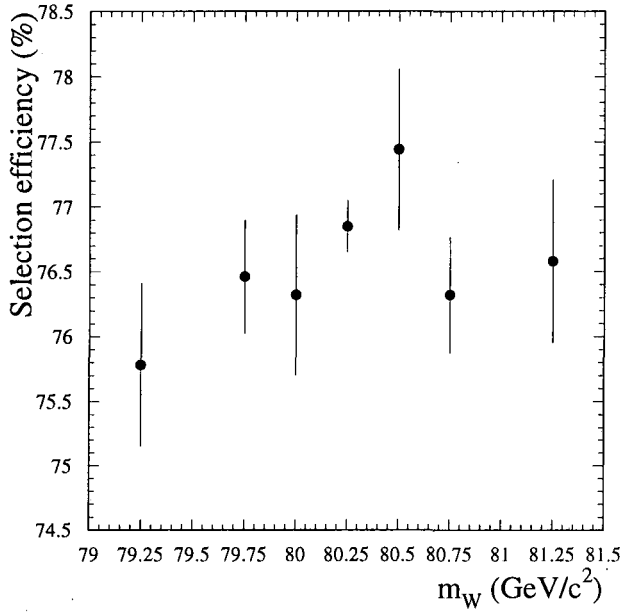

Figure 4.3: Hadronic efficiency as a function of the W mass.

4.4 Jet clustering algorithm

The most problematic thing when working with the hadronic channel is the reconstruction of its four-quark underlying structure because of the overlap between particles from different W's.

Different jet clustering algorithms are available to perform a good jet-quark matching. To choose which one a study is perfomed using DURHAM [72], JADE [71] and LUCLUS [73] in different recombination schemes [74]: E, P and E_0. A detailed description of each algorithm is available in appendix A.1.

The energy resolution, angular resolution and the shift between the reconstructed W mass and the generated one, Δm, are shown in table 4.1 for the different algorithms together with the different schemes.

Jet clustering	$\sigma(E)$(GeV)	$< \Delta m >$(GeV/c^2)	$\sigma(\cos\theta)$	$\sigma(\phi)$
DURHAM-P	13.42	8.07	0.303	0.397
DURHAM-E	14.46	4.01	0.328	0.418
DURHAM-E_0	14.43	4.60	0.311	0.408
DURHAM-PE	14.35	3.97	0.328	0.417
JADE-P	14.38	8.55	0.321	0.418
JADE-E	15.23	4.23	0.351	0.444
JADE-E_0	15.49	4.62	0.338	0.440
JADE-PE	14.83	4.11	0.350	0.442
LUCLUS	15.19	3.92	0.306	0.402

Table 4.1: Energy resolution, mass shift and angular resolutions for the different jet clustering algorithms and combination schemes.

DURHAM-P is the one which shows to have a better performance in correctly assigning particles to jets, evaluated in terms of jet energy and angular resolution. However, because the P-scheme assumes massless particles, large shifts appear between the reconstructed and the generated W masses. Thus, in order to guarantee the Lorentz invariance, a mixing between P and E schemes is used, i.e, the P-scheme is used to decide which particles (energy-flow objects) are assigned to which jet, and the E-scheme is used afterwards to compute the jet four-momenta.

4.5 Kinematical fit

The fact that four jets are forced in each event results in a smearing of the original quark energies and directions and, therefore, correlations between the reconstructed jets are introduced, as can be seen in table 4.1. This is mainly due to the finite energy resolution of the detector in combination with the loss of particles (loss in the beam pipe and cracks, etc.).

A kinematical fit will correct for some of these effects and translate the measured jet momenta to corrected ones fulfilling, at least, constraints such as energy and momentum conservation. This technique is very powerfull and as well a useful background rejection criterion. It is a very effective way to use all the information available in an event.

Different kinematical fits are available in order to improve the jet-resolution. They ask for different constraints and, therefore, ends up to different invariant masses.

The `MATHKINE` [77] package, whose principles are explained in appendix A.3, is used to do the kinematical fitting.

To apply the constrained fit it is necessary to determine a suitable parametrisation of the jet momenta so that the chosen parameters have distributions close to Gaussian distributions. In order to have full freedom in three directions for jets in the constrained fit, three parameters per jet are necessary giving a total of twelve parameters. Several choices are possible, as for example the jet energies and angles, and they must have a distribution as close to Gaussian as possible. Inspired by the Gaussian nature of the energy resolution of the detectors and so for the transverse momentum, the choice of parameters are defined through the following equation:

$$\vec{p}_j^{\,r} = a_j |\vec{p}_j^{\,m}| \vec{u}_j^{\,a} + b_j \vec{u}_j^{\,b} + c_j \vec{u}_j^{\,c}, \tag{4.1}$$

where the unit vectors $\vec{u}_j^{\,a}$,$\vec{u}_j^{\,b}$ and $\vec{u}_j^{\,c}$ are determined from the measured jet momenta and form a Cartesian system. The unit vector $\vec{u}_j^{\,a}$ is defined in the direction of the measured momentum, $\vec{u}_j^{\,b}$ is in the plane defined by the object axis and the z axis, and $\vec{u}_j^{\,c}$ is perpendicular to $\vec{u}_j^{\,b}$. The reconstructed energy of the jet is written as:

$$E_j^r = E_j^m \frac{|\vec{p}_j^{\,r}|}{|\vec{p}_j^{\,m}|} \tag{4.2}$$

making the jet massless.

The expectation values and resolutions of the parameters (a_i, b_i, c_i) are extracted from Monte Carlo studies by matching the measured jets to the underlying quarks.

Within this package, three possible constrained fits are available:

- 4C : requiring energy and momentum conservation.
- 5C : a 4C with the additional constraint that the two reconstructed masses, corresponding to the two W's in the event are equal to within some resolution.
- 4C+Rescaling : a 4C with the rescalation of the two reconstructed masses using the beam energy [80]:

$$m_{ij}^{resc} = m_{ij} \frac{E_b}{E_i + E_j}, \tag{4.3}$$

where E_b is the beam energy and E_i, E_j are the jet energies. The rescaled masses are directly related to the velocities of the two W's, and each one depends on the mass of both W's.

A comparison of the invariant mass resolution (reconstructed mass minus generated mass) for each constrained fit is done in figure 4.4. It can be seen that from 4C to 5C or 4C+R, there is an improvement. The invariant mass distributions for 5C and 4C+R are similar. The 4C+R fit seems to be less sensitive to detector systematic effects [81] and is eventually chosen for this analysis.

The number of signal and background events for which the fit has converged are shown in tables 4.2 and 4.3 respectively. Almost all signal events converge while not for background.

4.6 Jet pairing

For each selected event, the four jets can be coupled into two di-jets in three different ways. For each of these combinations, two rescaled 4C masses are determined as explained in the previous section. It is not obvious which one of these partitions is correct and, therefore, a jet pairing algorithm to choose one of them is needed. Three different pairing algorithms are tested, combined with two different window cuts in the invariant mass:

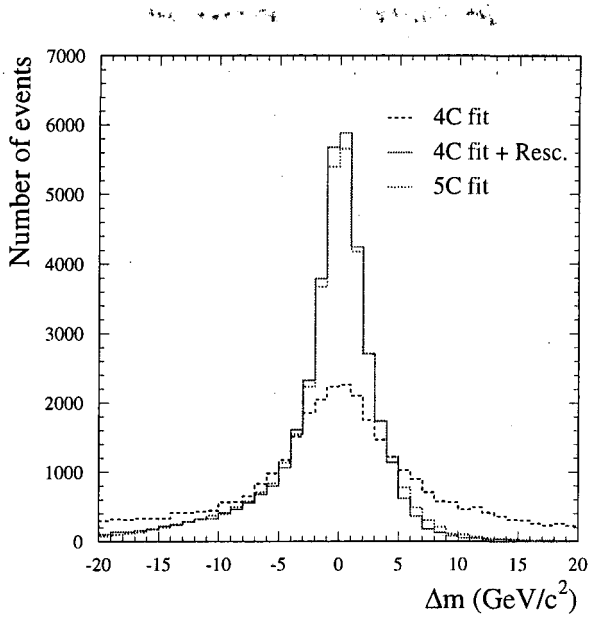

Figure 4.4: W mass resolution (reconstructed mass minus generated mass) for three different kinematical fits: 4C, 4C+R and 5C. The reconstructed masses correspond to the correct di-jet pair.

- **Chi2 Scheme** [82]: Among those combinations with the masses inside the window, the one with the smallest χ^2 from the 5C fit is chosen.
- **Angles Scheme** [83]: The combination chosen is the one with the smallest mass difference unless this is the one with the smallest sum of angles; in this case, the combination with the second smallest mass difference is chosen. Once the combination is chosen, the window cut is applied.
- **Reference Mass Scheme** [84]: The combination chosen is the one minimizing the distance of the two invariant masses to a certain reference mass. This distance is defined as $\Delta m = (m_1 - M_W^{ref})^2 + (m_2 - M_W^{ref})^2$. An iteration is performed using the fitted mass value as the new reference mass. Once the combination is chosen, the window cut is applied.

The two window cuts are:

- **Window 1**: $50 < m_1$ and $m_2 < 86$ GeV/c^2 and
  $74 < m_1$ or $m_2 < 86$ GeV/c^2.
- **Window 2**: $74 < m_1$ and $m_2 < 86$ GeV/c^2.

where m_1 and m_2 are the two resconstructed masses per event. For the chosen combination, the two masses are treated separately. The order of these two masses is taken randomly, so that the expected distribution for both masses is exactly the same.

The performance of these algorithms is compared on the basis of their final mass error. To do this, 300 Monte Carlo independent samples with the number of events fixed to the one expected for the data integrated luminosity ($10.65\,\mathrm{pb}^{-1}$) are built for each pairing algorithm. The dispersion of the obtained fitted masses is taken as an estimation of the error in the mass measurements associated to each method.

The results of such experiments show that the errors do not differ very much between *Chi2* and *Angles* schemes, although they are slightly smaller for the second one [85], [86].

The iterative *reference mass* scheme is not well defined when fitting through a reweighting technique (explained later in 4.7) because two distributions vary at the same time. Therefore a different type of fit, using a Breit-Wigner function for example, is needed in the intermediate steps.

At the end, the *Angles* scheme combined with the *Window 1* cut is chosen as jet pairing algorithm, since it is the one which provides the smallest error and has a simple implementation.

The number of signal and background events fulfilling the conditions for the jet pairing are shown in tables 4.2 and 4.3 respectively.

Process	$W^+W^- \to 4q$	$W^+W^- \to 2q\ell\nu$	$W^+W^- \to 2\ell\nu$
Generated events	45845	43070	11083
Class 16	45761	42897	115
N.N. cut	37780	276	0
Convergence fit	37743	253	0
Pairing & window	35231	229	0
Efficiency (%)	76.85 ± 0.20	0.53 ± 0.03	0
σ^{eff} (pb)	4.43	0.03	0.

Table 4.2: Number of events surviving cuts, final efficiencies and effective cross-sections for the three W^+W^- decays: $4q$ hadronic, $2q\ell\nu$ semileptonic and $2\ell\nu$ leptonic channels. The events are generated with a $M_W = 80.25\,\mathrm{GeV}/c^2$ 4f-KORALW Monte Carlo.

Process	$q\bar{q}(\gamma)$	Z^0Z^0	Z^0ee	2-γ	τ pairs
Generated events	475000	13056	7000	200000	5000
Class 16	435456	8934	2327	1992	1295
N.N. cut	4784	427	11	0	0
Convergence fit	4585	414	7	0	0
Pairing & window	3967	352	6	0	0
Efficiency (%)	0.84 ± 0.01	2.70 ± 0.14	0.09 ± 0.04	0	0
σ^{eff} (pb)	1.02	0.08	0.01	0.	0.

Table 4.3: Number of events surviving cuts, final efficiencies and effective cross-sections for different background processes.

4.7 W mass determination method

Once the invariant mass distributions are obtained by direct reconstruction different methods for extracting the W mass are possible.

(i) Breit-Wigner method.

The simplest method makes use of a Breit Wigner relativistic probability density function:

$$F(m) = \frac{M_W \, \Gamma_W}{(m^2 - M_W^2)^2 + M_W^2 \, \Gamma_W^2} \tag{4.4}$$

which uses the information about M_W contained in the two event-by-event resontructed invariant masses of W-pair events.

Fitting this distribution to the reconstructed invariant mass distribution of the data, the mass of the W boson is measured. As the invariant mass distribution in data is not exactly a Breit Wigner distribution due to phase space restrictions, detector resolution, radiation losses, background contamination, etc., which distort it relative to the true invariant mass distribution, a calibration is needed (the reconstructed mass of a Monte Carlo sample generated with a known input W mass is not the same as the input mass itself). In this sense, it is not easy to find a probability density function describing correctly the experimental distribution. This makes this method not optimal in what the expected error is concerned. Nevertheless it is worth for cross-checking the result obtained by other techniques.

(ii) First generation fitting formula.

(iii) Second generation fitting formula.

Another more sophisticated method is the one which uses a second generation fitting formula. The fit is done to a probability density function which uses not only the information of the W mass contained in the invariant mass distributions but in the angular variables such as the polar W production angle or the di-jet angles as well, thus making an optimal use of all the information of the W boson contained in the W-pair events. The method gives a very competitive result. The details of this method are described in [87].

(iv) The reweighting method.

The method to which this thesis is devoted is the reweighting technique explained below.

Reweighting method

Relying on Monte Carlo simulation, the probability density function (*p.d.f.*) can be extracted from simulated events. This has the advantage that all of the effects distorting the invariant mass distributions are accounted for in the fit, but there is also the caveat that the effects must be correctly implemented in the Monte Carlo. This problem is present in all methods studied so far.

To avoid having to generate large Monte Carlo samples at many different input W masses, a Monte Carlo event reweighting technique is used. A large amount of Monte Carlo events at a reference W mass value, M_{W}^{ref}, (e.g. $M_{\mathrm{W}}^{ref} = 80.25\,\mathrm{GeV}/c^2$) is generated and their invariant mass distributions (one per each W) are reweighted to produce reconstructed invariant mass distributions for any W mass , M_{W}, and W width, Γ_{W}, with the ratio of squared matrix elements:

$$w_i(M_{\mathrm{W}}, \Gamma_{\mathrm{W}}) = \frac{|\mathcal{M}(M_{\mathrm{W}}, \Gamma_{\mathrm{W}}, p_i^1, p_i^2, p_i^3, p_i^4)|^2}{|\mathcal{M}(M_{\mathrm{W}}^{ref}, \Gamma_{\mathrm{W}}^{ref}, p_i^1, p_i^2, p_i^3, p_i^4)|^2}, \tag{4.5}$$

where p_i^j denoted the four-momentum of the jth outgoing fermion for a particular event i, and $\mathcal{M}(M_{\mathrm{W}}, \Gamma_{\mathrm{W}}, p_i^1, p_i^2, p_i^3, p_i^4)$ is the matrix element of the process $\mathrm{e^+e^-} \rightarrow \mathrm{W^+W^-} \rightarrow \mathrm{f_1\bar{f}_2f_3\bar{f}_4}$. The matrix element $\mathcal{M}$ is evaluated for the so-called CC03 diagrams (2.1) which correspond to the three Feynman diagrams that contribute

to the W-pair production at tree level [88]. Only the invariant mass distributions of both reconstructed W's per event are considered and reweighted in this analysis, even though other distributions containing information of the W mass could be as well used and reweighted with the same weight, w_i.

In this analysis the W width is fixed to the Standard Model prediction. The probability density function for an event to have a certain invariant mass, m, between two bins, i and $i+1$, with a given W mass, M_{W}, is given by:

$$p.d.f.\ (m_i \leq m < m_{i+1} \mid M_{\mathrm{W}}) = \frac{\rho_s(M_{\mathrm{W}})\ N_s^i(M_{\mathrm{W}})\ +\ \rho_b(M_{\mathrm{W}})\ N_b^i}{\Delta m_i\ N_{TOT}}, \tag{4.6}$$

where Δm_i is the size of the bin: $m_{i+1} - m_i$, ρ_s is the signal purity, the purity of the background is $\rho_b = 1 - \rho_s$, $N_s^i(M_{\mathrm{W}})$ is the weighted number of signal events from the reference Monte Carlo in the reconstructed mass bin, i:

$$N_s^i(M_{\mathrm{W}}) = \sum_{j=1}^{n_s^i} w_j(M_{\mathrm{W}}) \tag{4.7}$$

(n_s^i being the number of signal events from the reference Monte Carlo found in bin i) and N_b^i is the total number of background events found in the same bin. Background events do not depend on W mass, therefore the shape and absolute normalisation of the non-WW background do not change in the reweighting procedure. N_{TOT} is the weighted sum of the reference Monte Carlo events:

$$N_{TOT} = \sum_{i=1}^{N_{bin}} \left(\rho_s(M_{\mathrm{W}}) \sum_{j=1}^{n_s^i} w_j(M_{\mathrm{W}}) + \rho_b(M_{\mathrm{W}})\ N_b^i \right), \tag{4.8}$$

where N_{bin} is the number of reconstructed mass bins.

The main dependence on the W mass is given by the weights, but there is a residual dependence on M_{W} through the purity of the selection. Assuming that the selection efficiency does not depend on M_{W} (see figure 4.3) there is only a marginal dependence due to the $\mathrm{W^+W^-}$ cross section, $\sigma_s(M_{\mathrm{W}})$. This dependence is parameterised (by using the GENTLE package [89]) with a simple parabola restricted to the region nearby the reference mass, giving the following expression:

$$\sigma_s(M_{\mathrm{W}}) = \sigma_s(M_{\mathrm{W}}^{ref}) \left(1 - 0.063(M_{\mathrm{W}} - M_{\mathrm{W}}^{ref}) - 0.0080(M_{\mathrm{W}} - M_{\mathrm{W}}^{ref})^2\right). \tag{4.9}$$

Denoting the efficiency of the selection for signal as ϵ_s and the background efficiency as ϵ_b, the purity depending on M_{W} can be written as:

$$\rho_s(M_{\mathrm{W}}) = \frac{\epsilon_s \, \sigma_s(M_{\mathrm{W}})}{\epsilon_s \, \sigma_s(M_{\mathrm{W}}) \; + \; \epsilon_b \, \sigma_b}. \tag{4.10}$$

The size of the reconstructed mass bins of the reference Monte Carlo (signal and background) as well as of the data is the same. The bin widths are obtained from the amount of reference Monte Carlo in order to have a statistical precision approximately constant along the invariant mass distribution: Δm_i is chosen to be narrower near the invariant mass peak ($\sim 10\,\mathrm{MeV}/c^2$) and broader in the tails ($\sim 100\,\mathrm{MeV}/c^2$).

The compatibility of the Monte Carlo and data invariant mass distributions is calculated with a likelihood procedure, and the best estimator of the W mass is the one that maximizes the likelihood function:

$$\mathcal{L}(M_{\mathrm{W}}) = \prod_{i=1}^{N_{evt}} p.d.f.(m_i \mid M_{\mathrm{W}}) \tag{4.11}$$

N_{evt} being the number of selected events which enter in the minimization. The reweighting method uses a rather large number of reference Monte Carlo events compared to data. Typically between 15 and 20 times the data luminosity.

Weighted events have a limited statistical power. For a set of n events the sum of the weights, S, and the statistical error of the sum, σ_S, are given by:

$$S = \sum_{i=1}^{n} w_i \quad \text{and} \quad \sigma_S = \left(\sum_{i=1}^{n} w_i^2 \right)^{1/2}. \tag{4.12}$$

The effective number of generated events, n_{eff}, can be obtained by:

$$n_{eff} = \frac{\left(\sum_{i=1}^{n} w_i \right)^2}{\left(\sum_{n=1}^{n} w_i^2 \right)}. \tag{4.13}$$

If n_{eff} is small compared to the true number n of generated events, the weight distribution has a large RMS (see figure 4.6) and the Monte Carlo simulation is inefficient. The effective number of events when reweighting a Monte Carlo with

M_{W} (GeV/c^2)	n_{eff}	n
79.25	16099.99	0.457
79.75	28094.18	0.797
80.00	33208.92	0.943
80.25	35231.00	1.000
80.50	33196.98	0.942
80.75	28015.71	0.795
81.25	15796.37	0.448

Table 4.4: Number of effective of events, n_{eff}, when reweighting a Monte Carlo with $M_{\mathrm{W}}^{ref} = 80.25\,\mathrm{GeV}/c^2$ to different W masses, and the ratio n_{eff}/n (n being the number of events reweighted).

$M_{\mathrm{W}}^{ref} = 80.25\,\mathrm{GeV}/c^2$ to different W masses, as well as the ratio n_{eff}/n (n: number of reference Monte Carlo events) is shown in table 4.4.

It is important to note that going away $1\,\mathrm{GeV}/c^2$ from the reference value, only less than half per cent of the events are effectively taken into account.

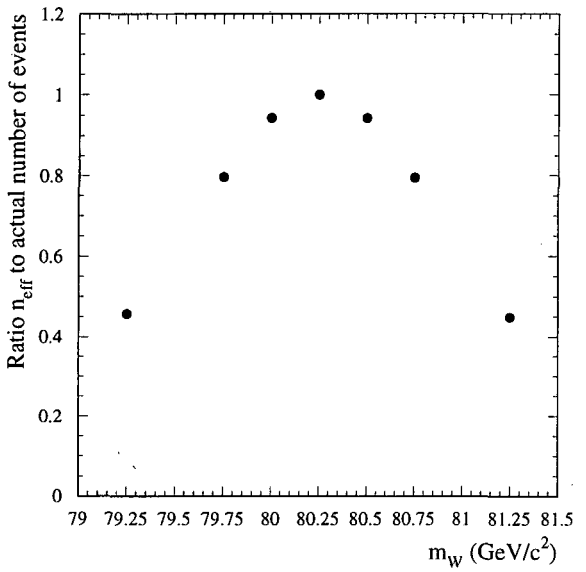

Figure 4.5: Ratio of effective number of events to actual number of events for different W masses. Effectively, half of the events are lost when going from $M_{\mathrm{W}} = 80.25\,\mathrm{GeV}/c^2$ to $M_{\mathrm{W}} = 81.25\,\mathrm{GeV}/c^2$.

Figure 4.6 shows the distributions of weights when the reference sample with $M_{\mathrm{W}}^{ref} = 80.25\,\mathrm{GeV}/c^2$ is reweighted to other masses. This shows that the farther away M_{W} is from M_{W}^{ref}, the more different from unity the weights become (see table 4.4).

As a large effective reference Monte Carlo sample is needed in the reweighting method, the fit to the data will be obtained by using a reference sample with the W mass the closest to the fitted mass.

Figure 4.7 shows how the reweighting method changes the invariant mass distribution from a reference value ($M_{\mathrm{W}}^{ref} = 80.25\,\mathrm{GeV}/c^2$) to two different M_{W}: 79.25 and $81.25\,\mathrm{GeV}/c^2$. All the distributions are normalised to the same number of events.

When the Z^0 mass was measured at LEP1, a mass definition corresponding to a propagator including an s-dependent width was used, whereas in the formulae and Monte Carlo used to extract the W mass, a Breit-Wigner propagator with fixed width is used, as suggested in Ref. [18]. To make both measurements consistent with each other, a positive shift of $27\,\mathrm{MeV}/c^2$ is applied throughout on the measured W mass.

4.8 Monte Carlo expectations and checks

In this section checks with Monte Carlo such as a calibration curve, expected correlations between masses as well as the expected error are shown.

4.8.1 Correlation between reconstructed masses

Two masses, one per di-jet, are reconstructed per event. Figure 4.8 shows how these two masses are distributed in the range (74,86) GeV/c^2. The plot corresponds to approximately $4000\,\mathrm{pb}^{-1}$ of signal and background Monte Carlo events. The correlation between the two masses is found to be: $66.7 \pm 0.3\%$.

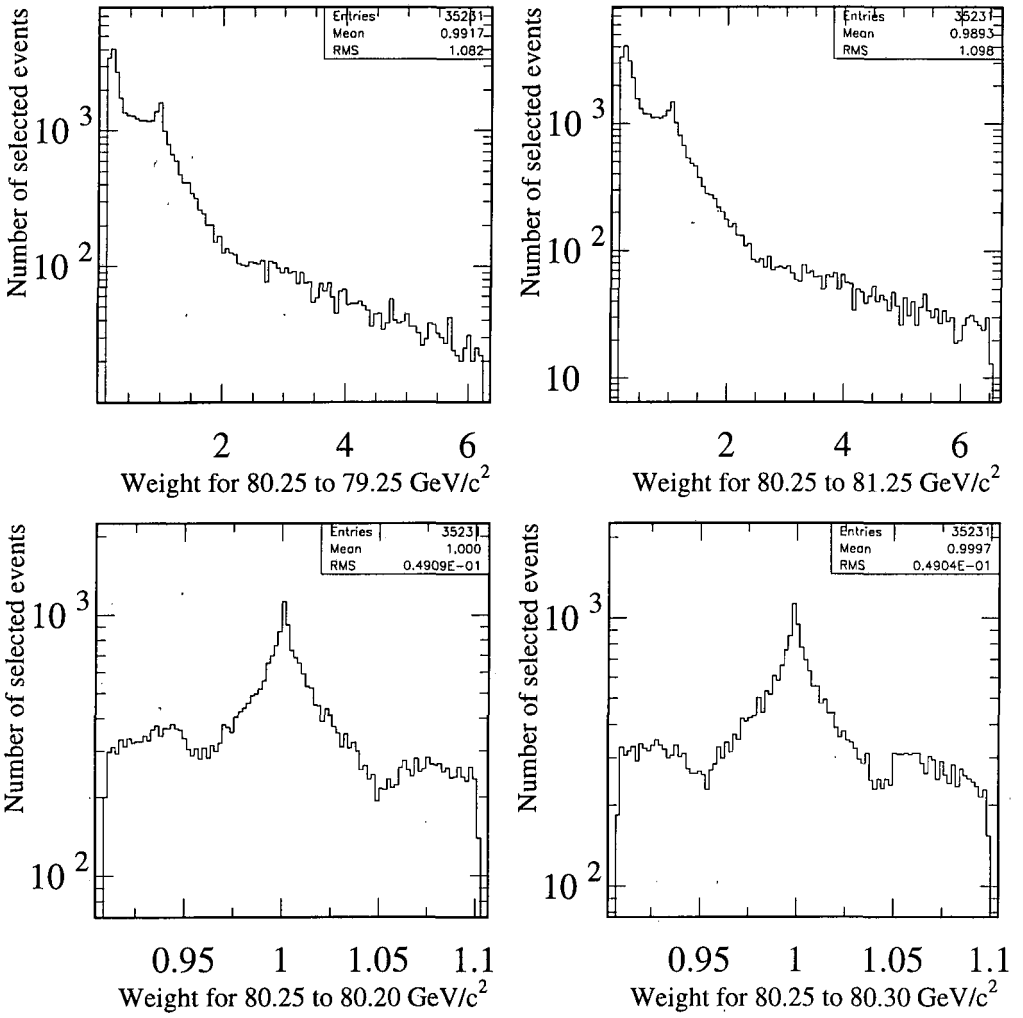

Figure 4.6: Event weights when WW $\rightarrow$ 4q events at $M_W = 80.25\,\mathrm{GeV}/c^2$ are reweighted to $M_W = 79.25$, 81.25, 80.20 and $80.30\,\mathrm{GeV}/c^2$ respectively.

4.8.2 Expected error

Due to the small size of the data sample (10.65 pb^{-1} from which 65 events are selected) the statistical error obtained from the fit has a large uncertainty. Three hundred independent Monte Carlo samples of the size of the data, such that they contain the *expected* number of events, are used to obtain an estimation of the

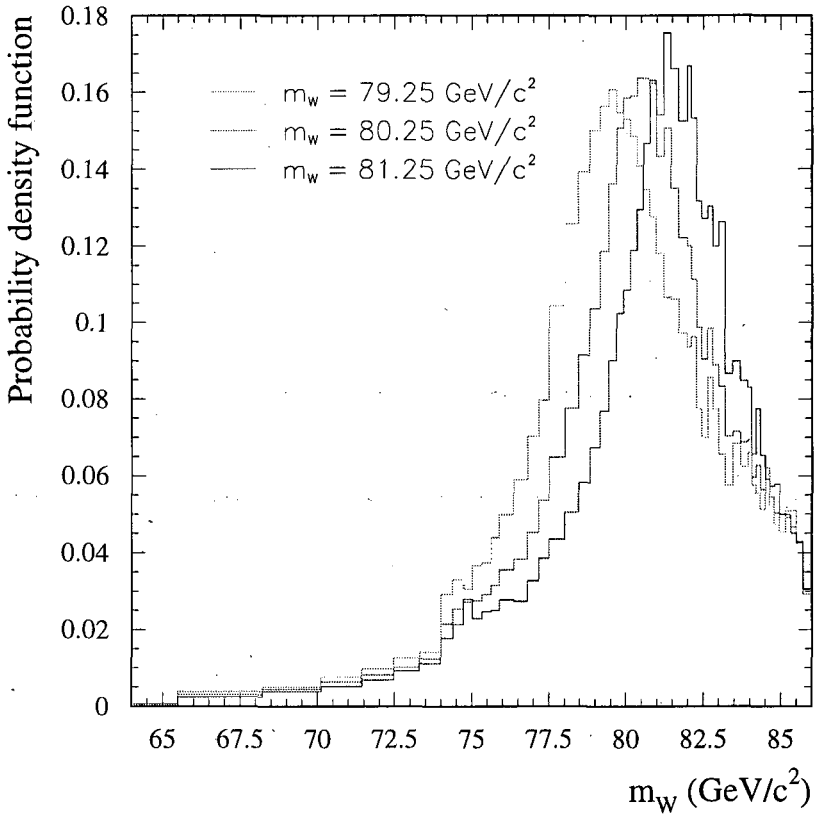

Figure 4.7: Invariant mass distributions for different M_W: 80.25 GeV/c^2 and the reweighted ones to 79.25 and 81.25 GeV/c^2. All distributions are normalised to the same number of events.

statistical error. Figure 4.9 shows the distribution of one of the mass estimators as well as the distribution of the corresponding positive and negative errors. The agreement between the RMS (root mean square) of the mass estimator distributions and the mean value of the errors distributions is good. Since the uncertainty on the mean value of the mass error distribution is smaller than the uncertainty on the RMS of the mass distribution, the value of 0.58 GeV/c^2, is taken as expected error for a sample of the size of the data, for each of the two hadronic masses. Note that there is no discrepancy between the expectation for both estimators, $\hat{m}_1$ and $\hat{m}_2$.

4.8.3 Calibration curves

A test that ensures that the fitted mass is not biased is the calibration curve, the fits of various Monte Carlo samples with different W mass should match with the input W masses. The linearity of the fitted mass with respect to the true input

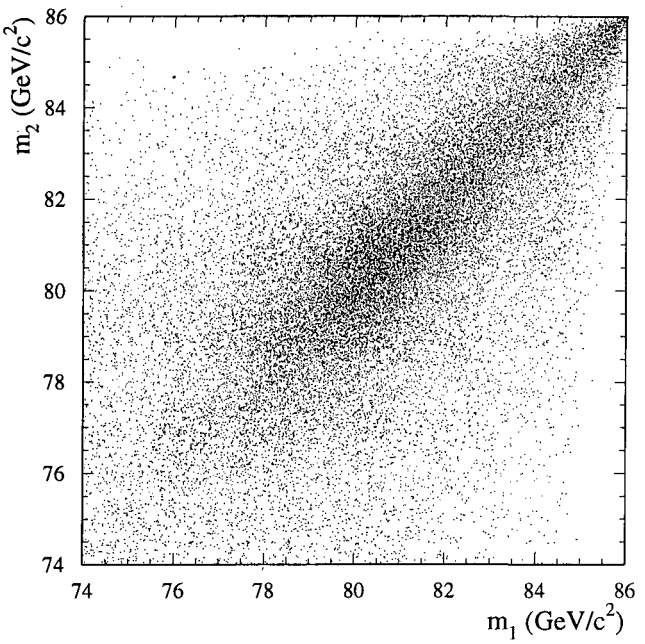

Figure 4.8: Correlation between the two event-by-event reconstructed masses for Monte Carlo events.

mass is studied using seven independent Monte Carlo samples (of $500\,\mathrm{pb}^{-1}$ each) with different input masses (the samples contain signal and background events in the adequate proportion). Figure 4.10 shows the two fitted masses as a function of the generated ones. A straight line, $\hat{m} = P_1 + P_2(M_{\mathrm{W}}^{true} - 80.25)$, is fitted to the points. The result of the fit together with the ideal line, $\hat{m} = M_{\mathrm{W}}^{true}$, are shown. The fitted lines are compatible with the ideal lines with slope value consistent with one and no significant offsets.

4.8.4 Event selection and mass range dependence

The events are selected by requiring the neural network output to be larger than -0.3. The stability of the result as a function of this cut is studied by using a single sample of $500\,\mathrm{pb}^{-1}$ Monte Carlo events. Figure 4.11 (top plot) shows the fitted mass as a function of the neural network output. The errors on the points are highly correlated because the same single sample is used for all the points. The

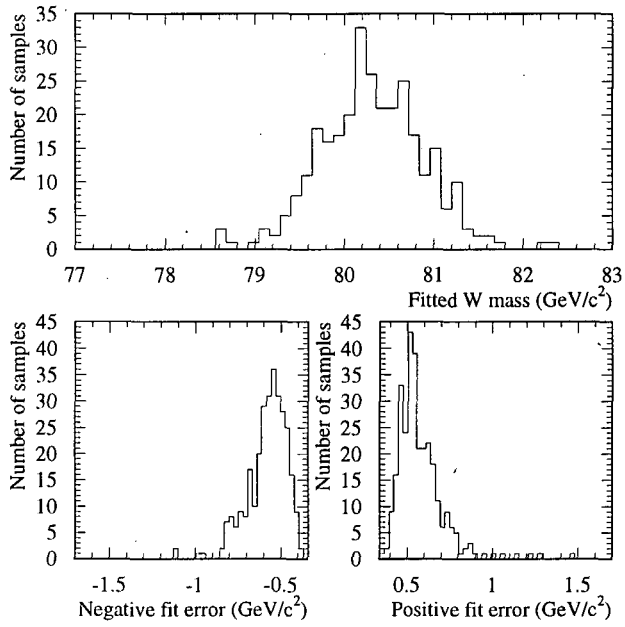

Figure 4.9: Distributions of one of the fitted masses with their positive and negative errors for 300 Monte Carlo samples of the same size of the data.

bottom plot in the same figure shows the expected error as a function of the cut. No statistically significant differences are observed in the fitted mass.

By doing the same in the selected data events, figure 4.12 is obtained. The same conclusion as before is reached.

The stability of the result as a function of the mass range used for the fit is checked also, using both data and the sameMonte Carlo samples as before. Changing the lower limit of the acceptance window and keeping the higher limit fixed at $86\,\mathrm{GeV}/c^2$, no significant mass range dependence on the fit neither on the expected error is observed, and the agreeement between data and Monte Carlo is good (figures 4.13 and 4.14).

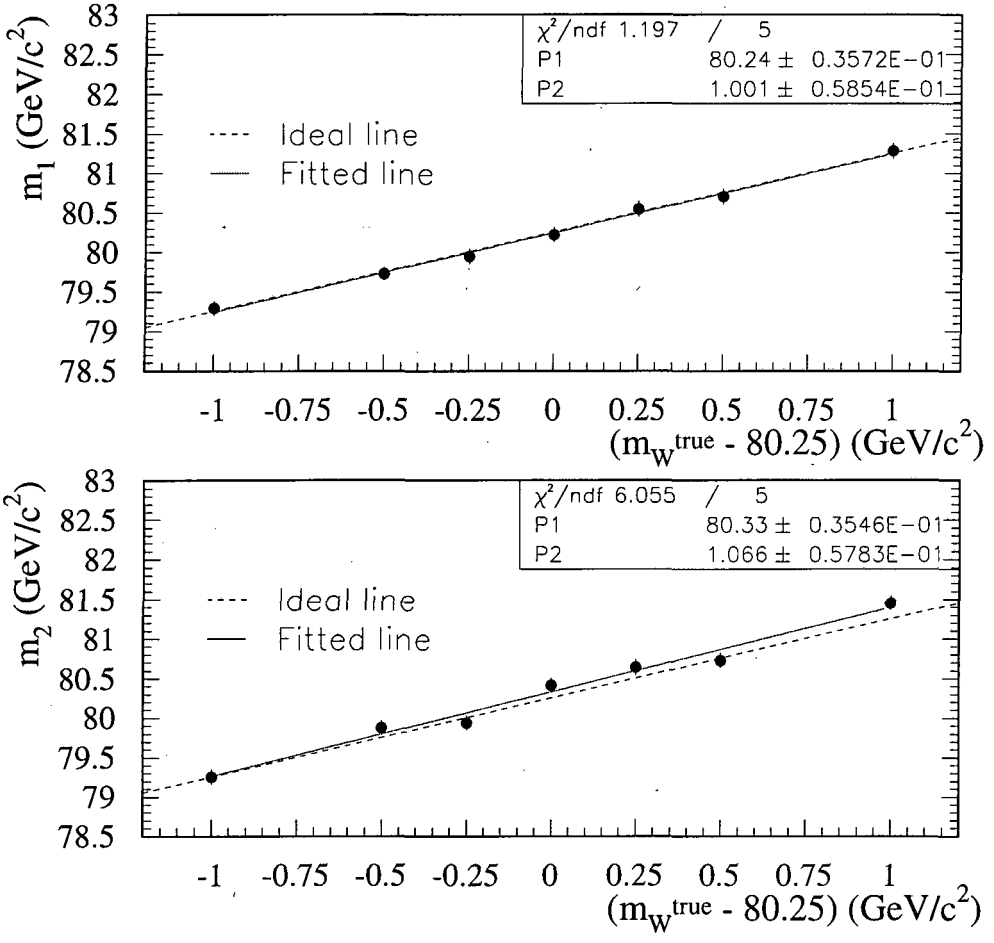

Figure 4.10: Fitted mass versus generated mass for seven Monte Carlo samples of 500 pb^{-1} each. The fill lines correspond to the result of the fit and the dashed ones to the ideal case ($m = M_W^{true}$). The two plots correspond to the two fitted masses per experiment.

4.8.5 Mass measurement using a Breit-Wigner fit

As a cross-check of the reweighting method, a simple relativistic Breit-Wigner function is fitted to the observed invariant mass distributions. In this method, the distortions described at the beginning of this section, introduce a bias in the fitted mass which must be corrected for. This bias is found to be a linear function of the true input mass and is determined by fitting a stright line to the fitted mass versus

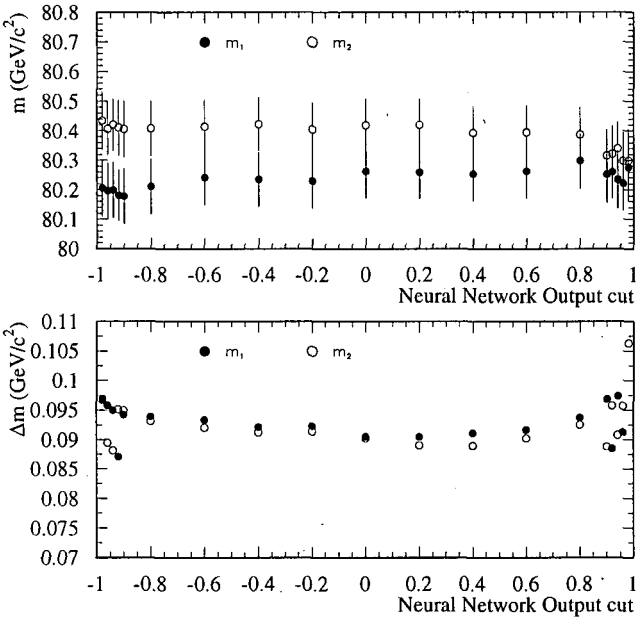

Figure 4.11: Fitted mass (top plot) and expected error (bottom plot) as a function of the neural network output cut for a sample of $500\,\mathrm{pb}^{-1}$ Monte Carlo events.

the true mass, using the seven Monte Carlo samples generated with different M_{W} values. The straight line function is known as the *calibration curve.*

Taking the Monte Carlo generated with $M_{\mathrm{W}} = 80.25\,\mathrm{GeV}/c^2$ as the reference Monte Carlo , the fit results for the selected 65 data events which fall in the mass window (74,86) GeV/c^2 are:

$$\begin{aligned} \hat{m}_1 &= 81.45 \pm 0.33\,\mathrm{GeV}/c^2 \\ \hat{m}_2 &= 81.32 \pm 0.35\,\mathrm{GeV}/c^2. \end{aligned}$$

The expected error for a sample of the size of the data is $0.45\,\mathrm{GeV}/c^2$ (before calibration) and the correlation between the two mass estimators ($\hat{m}_1$ and $\hat{m}_2$) is (47.1 ± 4.2) %.

Calibration curves to correct the fitted value and the expected mass error are built using the seven mass points with 52 samples of the size of the data each. A

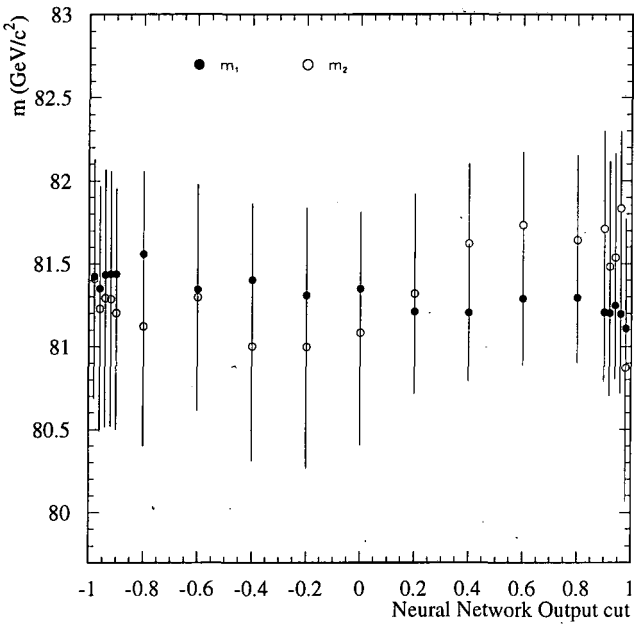

Figure 4.12: Fitted mass as a function of the neural network output cut for the selected data events.

straight line is fitted to each of these curves with the following results:

$$\hat{m_1} = (80.682 \pm 0.024) + (0.715 \pm 0.037) \times (M_{\mathrm{W}}^{true} - 80.25) \ \ (\mathrm{GeV/c^2})$$
$$\hat{m_2} = (80.689 \pm 0.022) + (0.745 \pm 0.034) \times (M_{\mathrm{W}}^{true} - 80.25) \ \ (\mathrm{GeV/c^2}).$$

$\hat{m} = (80.68 \pm 0.02) + (0.73 \pm 0.04) \times (m_{\mathrm{W}}^{true} - 80.25)$ (GeV) is taken as calibration curve for both masses. After calibration, the expected error for the masses is 620 MeV and the corrected values for the masses are:

$$\hat{m_1} = 81.30 \pm 0.62 \ \mathrm{GeV}/c^2$$
$$\hat{m_2} = 81.14 \pm 0.62 \ \mathrm{GeV}/c^2$$

which combined with the expected correlation (47.1%) give a final result for the W mass of:

$$\hat{M}_{\mathrm{W}} = 81.22 \pm 0.53 \ \mathrm{GeV}/c^2$$

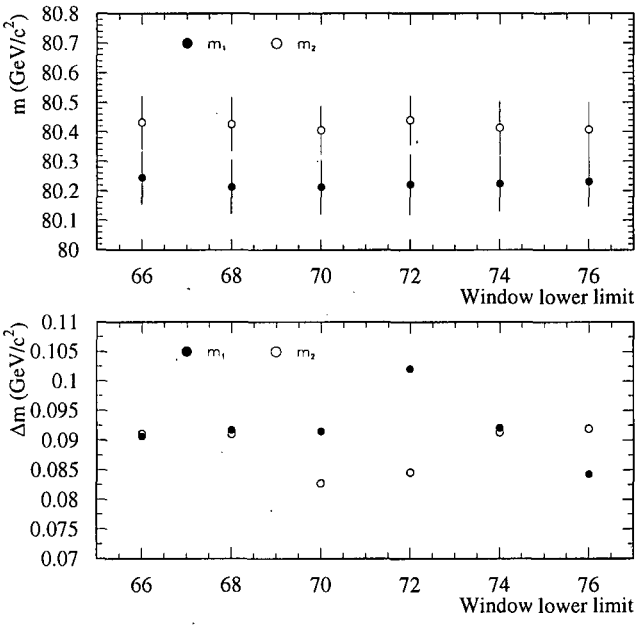

Figure 4.13: Fitted mass (top plot) and expected error (bottom plot) as a function of the acceptance window lower limit for a sample of 500 pb^{-1} Monte Carlo events.

in good agreement with the result obtained with the reweighting technique (see 4.14).

4.9 Results

To extract the W boson mass, the invariant mass distribution of reweighted Monte Carlo events is fitted to the data events distribution.

The number of selected events after all the requirements described in the previous sections is 65. The Monte Carlo predicts 56 events (44 of signal and 12 of background). Figure 4.15 shows the reconstructed event-by-event masses in the range (74,86) GeV/c^2. Their correlation is found to be 63.5 $\pm$ 7.4 %, in good agreement with the Monte Carlo expectation (66.7 $\pm$ 0.3 %).

The resuls of the fit for the selected events (falling in the mass window (74,86)

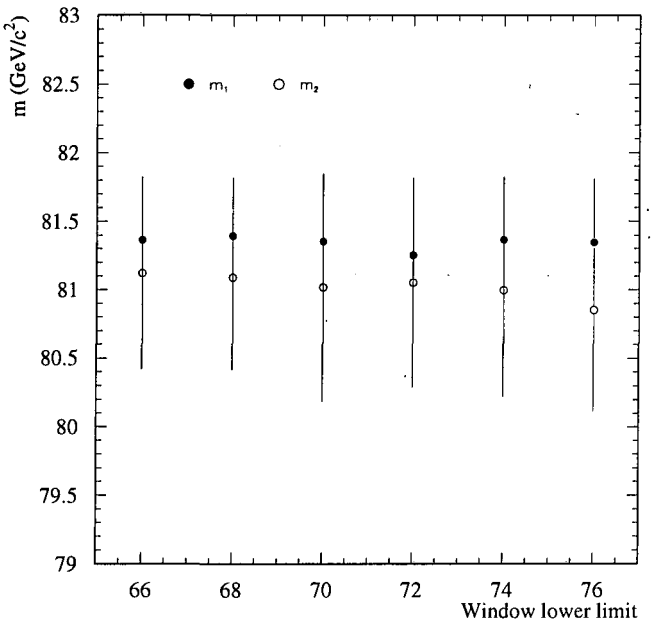

Figure 4.14: Fitted mass as a function of acceptance window lower limit for the selected data events.

GeV/c^2) using the reference Monte Carlo generated with $M_{\mathrm{W}} = 80.25\,\mathrm{GeV}/c^2$, are:

$$m_1 = 81.23^{+0.51}_{-0.56}\ \mathrm{GeV}/c^2$$
$$m_2 = 81.13^{+0.74}_{-0.72}\ \mathrm{GeV}/c^2$$

in agreement with the Breit-Wigner check.

As the fitted masses are closer to $81.25\,\mathrm{GeV}/c^2$ than to $80.25\,\mathrm{GeV}/c^2$, the final result is given using a Monte Carlo reference sample generated at $81.25\,\mathrm{GeV}/c^2$ instead. The results of the fitted masses are:

$$m_1 = 81.43^{+0.52}_{-0.53}\ \mathrm{GeV}/c^2$$
$$m_2 = 81.16^{+0.56}_{-0.62}\ \mathrm{GeV}/c^2$$

The combination of these two measurements using the Monte Carlo expected mass uncertainty ($0.58\,\mathrm{GeV}/c^2$) and correlation between estimators (33.2%) gives:

$$M_{\mathrm{W}} = 81.30 \pm 0.47\,\mathrm{GeV}/c^2 \qquad (4.14)$$

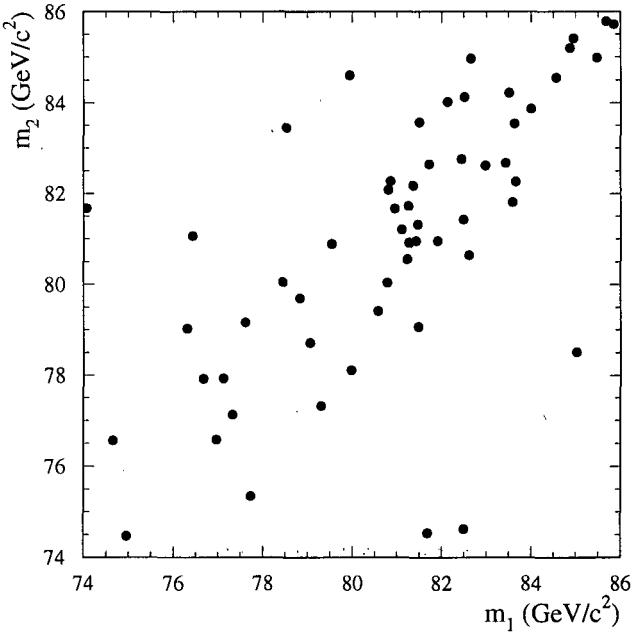

Figure 4.15: Correlation between the two event-by-event reconstructed masses for the data selected events.

Figure 4.16 shows the mass distribution (m_1 and m_2 combined) for the selected data events (points and error bars). The Monte Carlo distributions (signal+background) for the fitted mass, $M_W = 81.30\,\mathrm{GeV}/c^2$, as well as the background Monte Carlo distribution are also shown.

4.10 Systematic uncertainties

4.10.1 Finite reference Monte Carlo Statistics

Having a finite number of Monte Carlo events at the reference mass and using them in the reweighting technique contributes to a systematic uncertainty in the W mass measurement. The procedure used to study this effect consists of dividing the reference sample (signal and background) into smaller samples (10, 20, 30, 40 or 50 samples) of equal size. Each of these samples are then fitted to the same data. The RMS of the fitted masses scales as the square root of the number of samples (N_S)

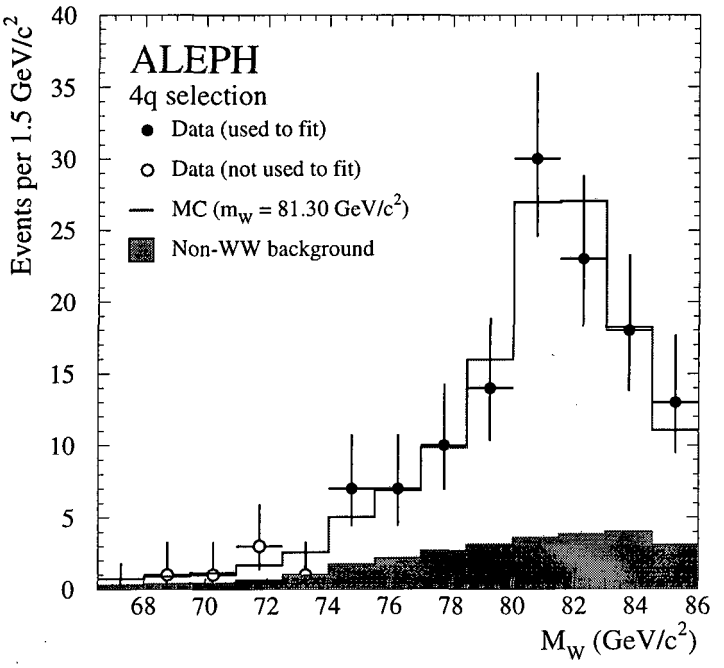

Figure 4.16: Mass distribution (m_1 and m_2) for hadronic data (points with error bars), background Monte Carlo (shaded area) and signal+background Monte Carlo for the best fit to the data taken at 172 GeV (empty histogram).

that the reference is divided into:

$$\mathrm{RMS} = \Delta M_{\mathrm{W}} \sqrt{N_S}.$$

Using this method, the systematic error coming from Monte Carlo statistics is estimated to be $\Delta M_{\mathrm{W}} = 40\,\mathrm{MeV}/c^2$.

4.10.2 Monte Carlo fragmentation parameters

The main Monte Carlo fragmentation parameters in JETSET ($\Lambda, M_{min}, \sigma, B$ and baryon production) are varied independently to extreme values, typically four standard deviations from their measured values [90]. With each variation, a new reference sample is made. The effect of these variations on the fitted mass is $\Delta M_{\mathrm{W}} = 10\,\mathrm{MeV}/c^2$ and is quoted as systematic error due to the uncertainty

on the Monte Carlo fragmentation parameters.

4.10.3 Diagrams in Monte Carlo reference

The matrix element used in this analysis corresponds to the CC03 diagrams instead of the complete matrix element which corresponds to all possible diagrams producing four fermions in the final state. The effect of this approximation is studied by comparing the weights derived from the CC03 matrix element with those derived from the complete matrix element as given by EXCALIBUR [91]. The contribution of the non-CC03 diagrams after the event selection is negligigle. Using the four-fermion matrix element to weight the Monte Carlo events, the fitted mass from the data differs from the original one by only $3\,\mathrm{MeV}/c^2$ [4].

4.10.4 Selection efficiency

The selection efficiencies are varied by $\pm 2\sigma$ of their statistical uncertainty, where $\sigma = 0.20\%$. In addition, the mass dependence of the selection efficiency (assumed to be independent on the W mass in this analysis) is studied over a $2\,\mathrm{GeV}/c^2$ mass range using the seven Monte Carlo samples with different M_W values, where maximal differences of $1.7 \pm 0.9\%$ are observed for the selection efficiency. A linear dependence as a function of mass is implemented in the fit with the slope obtained from the above studies. Both variations have a negligigle effect on the fitted results, hence giving no systematic uncertainty due to the selection efficiency.

4.10.5 Background contamination

The expected background remaining after the selection is about 20% of the sample. The small size of the data sample does not allow a detailed comparison of its properties (background shape and normalisation) with the ones predicted by the Monte Carlo samples used. To overcome this problem, a technique using Z^0 peak

[4] Since the use of the four-fermion matrix element implies an increase of two orders of magnitude in the CPU time needed to perform the fit, the result obtained using only CC03 diagrams is kept and a systematic uncertainty of $\Delta M_\mathrm{W} = 3\,\mathrm{MeV}/c^2$ due to this approximation is quoted.

data is developed to evaluate the systematic uncertainty coming from the background estimation [92]. High statistics Z^0 data taken in 1994 are compared to $q\bar{q}$ Monte Carlo to evaluate the effect of any discrepancies in the background shape and normalisation.

Background shape

A selection similar to the preselection of this analysis (making cuts on total visible energy, missing momentum, number of energy-flow objects, number of charged tracks, etc.), but scaled down according to beam energy, are applied to both Z^0 peak data and $q\bar{q}$ Monte Carlo simulated events. Figures 4.17 and 4.18 show the discrepancies between data and Monte Carlo in total energy, number of energy-flow objects and number of charged tracks.

The observed disagreements at LEP1 energies are applied as correction factors to the expected background in the 172 GeV analysis. The resulting observed shifts in the fitted W mass are then evaluated, and the largest mass shift is taken as systematic uncertainty due to the deficient modelling of the background. The systematic uncertainty is found to be $\Delta M_{\mathrm{W}} \sim 20\,\mathrm{MeV}/c^2$.

Background normalisation

The uncertainty in the background normalisation is estimated by comparing the effect in the fit of the W mass when taking into account the difference between the number of data and the expected number of Monte Carlo ($< 10\%$ difference). The effect is negligible (less than $10\,\mathrm{MeV}/c^2$).

4.10.6 Detector calibration

Some studies [93] indicate that there are differences between data and Monte Carlo in the energy calibrations of the electromagnetic (ECAL) and hadronic (HCAL) calorimeters of up to 1.5% and 4% respectively. The effect of these discrepancies is estimated by globally rescaling the ECAL energy by $\pm 1.5\%$ and the HCAL energy by $\pm 4\%$ at the event reconstruction level (by recomputing the energy-flow objects) in the data. The fit is redone for all the cases (ECAL +1.5%, ECAL −1.5%,

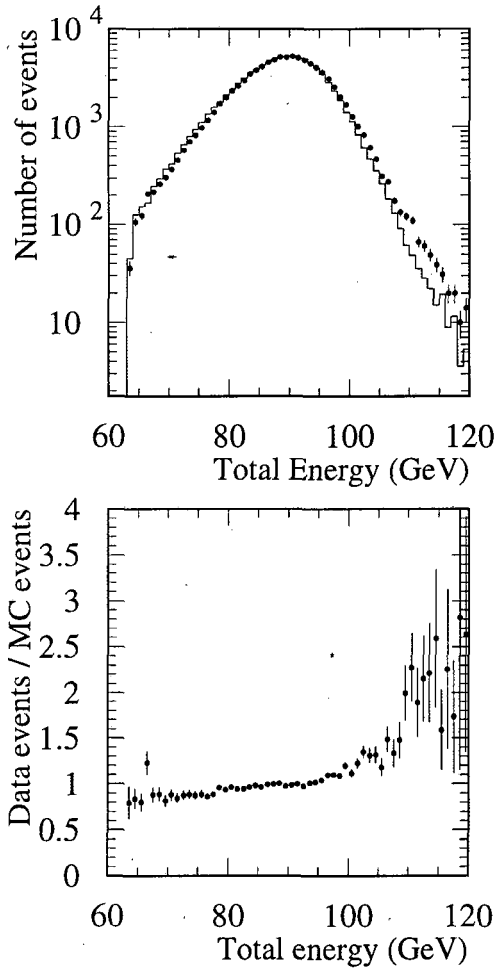

Figure 4.17: Top plot: total energy distribution for 94 data (points) and $q\bar{q}$ Monte Carlo (histogram). Bottom plot: ratio data over Monte Carlo.

HCAL +4%, HCAL −4%). Using the biggest change in both cases, the ECAL and HCAL errors are combined in quadrature to give a final uncertainty of: $\Delta M_W = 56\,\mathrm{MeV}/c^2$.

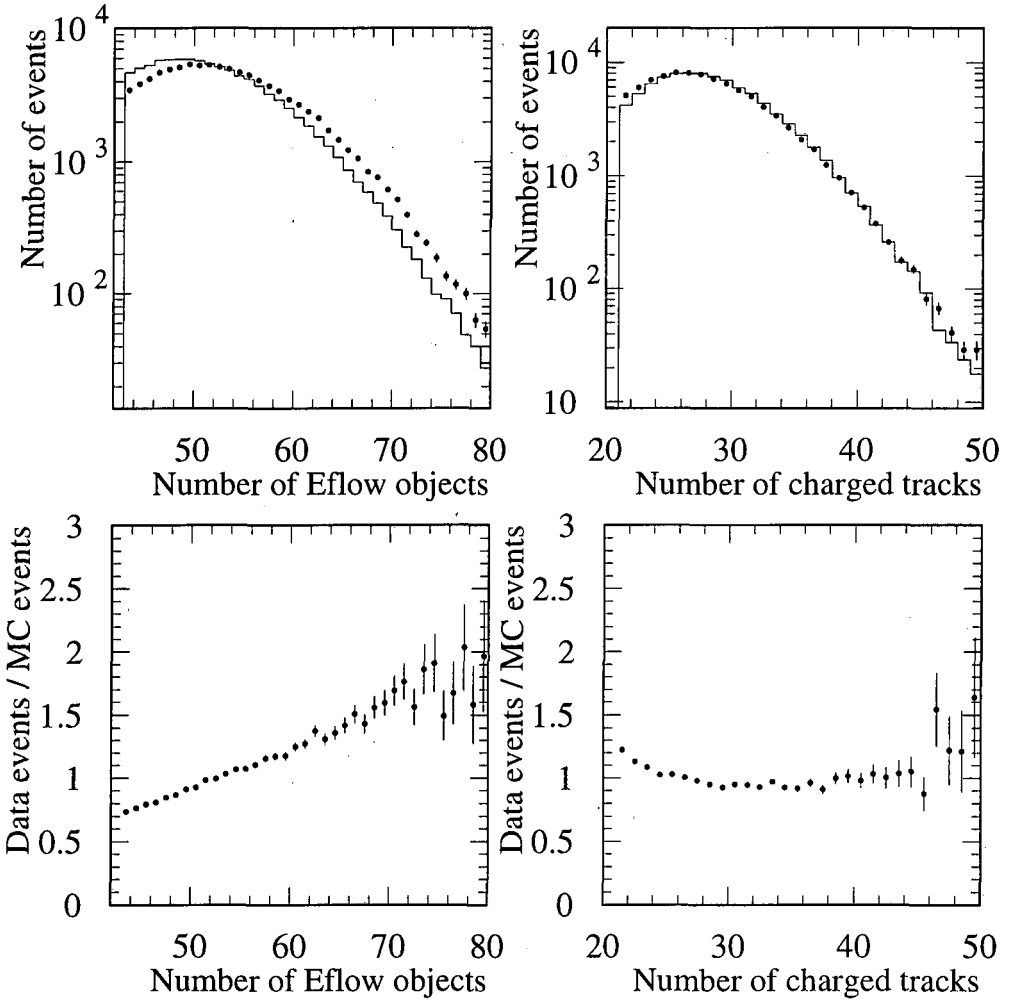

Figure 4.18: Top plots: number of energy-flow objects and number of charged track distributions for 94 data (points) and $q\bar{q}$ Monte Carlo (histogram). Bottom plots: ratio data over Monte Carlo.

4.10.7 Jet corrections in the kinematical fit

Using the expression 4.1 described in Section 4.5, the measured jet momenta ($|\vec{p_j^m}|$) are modified to allow global momentum rescalings and shifts in θ and ϕ. If the reconstruction were perfect, a_j would be 1, while b_j and c_j would be 0. Since the reconstruction is not perfect because of detector effects, the expected values and res-

olutions of these parameters depend on both the jet energy and polar angle. These correction factors are computed from Monte Carlo by comparing the reconstructed jets to the original parton quadrimomenta at a given mass. However, the Monte Carlo is known not to reproduce correctly the angular dependence of the energy-flow calibration: from hadronic Z^0 studies [94] jet energy corrections required for the data differ from those in the Monte Carlo by 30% in the region $\cos\theta_T \geq 0.95$ where θ_T is the angle between the beam axis and the thrust axis of the Z^0 di-jet.

To have an estimate of these effects, the correction factors are simultaneously increased/decreased by 30% of the difference of their expected values and used to fit the data. The maximum variation between fitted masses of $\Delta M_W = 40\,\mathrm{MeV}/c^2$ is taken as systematic uncertainty.

4.10.8 W boson width variation

The value of the W mass obtained from the fit is studied as a function of the W width. The width is varied around its central value by the known experimental error $\pm\sigma = 0.07\,\mathrm{GeV}$ [95]. The difference in the fitted mass is $\sim 10\,\mathrm{MeV}/c^2$ as is taken as systematic uncertainty.

4.10.9 Initial State Radiation

KORALW [96], the main event generator used in the studies, features QED initial state radiation up to $\mathcal{O}(\alpha^2 L^2)$, i.e. up to second order in the leading-log approximation, in the YFS style [97]. The effect of the missing terms on the W mass measurement is studied at generator level in [98] by degrading KORALW to $\mathcal{O}(\alpha^1 L^1)$ and checking the size of the pure $\mathcal{O}(\alpha^2 L^2)$ correction. A systematic effect on the W mass coming from the missing higher order terms of $15\,\mathrm{MeV}/c^2$ is quoted.

However, a check is performed by using the selection/reconstruction/fitting procedure applied to the 172 GeV data and explained in this section. Two different soft photon exponentiation, GKF [99] and YFS [97] are compared. The differences observed when degrading $\mathcal{O}(\alpha^2 L^2)$ to $\mathcal{O}(\alpha^1 L^1)$ are smaller than $15\,\mathrm{MeV}/c^2$. A conservative systematic error of $\Delta M_W = 15\,\mathrm{MeV}/c^2$ from Initial State Radiation is assigned.

4.10.10 LEP energy

The relative uncertainty on the LEP energy translates into the same relative uncertainty on the fitted mass, since the beam energy is directly used in the kinematic fit (4C + Rescaling):

$$\Delta M_{\mathrm{W}} = M_{\mathrm{W}} \frac{\Delta E_b}{E_b}. \tag{4.15}$$

For the quoted LEP beam energy uncertainty of $\Delta E_b = 30\,\mathrm{MeV}$ [100], a systematic uncertainty of $\Delta M_{\mathrm{W}} \sim 30\,\mathrm{MeV}/c^2$ due to LEP energy uncertainty is assigned.

4.10.11 Colour Reconnection effect

In hadronic events, the possible existence of colour reconnection (CR) effects between the two W's is pointed out as a source of systematic error on the W mass determination. Some studied [101, 102, 103, 104], quote large uncertainties. However, the size of the effect is likely to be sensitive to the topology of the selected events and to the actual procedure used to extract the W mass.

The colour reconnection effect is studied using two Monte Carlo samples generated with `EXCALIBUR` [91], one with a colour reconnection implementation, following the ansatz of [103], and the other one without. The 4-quark events in both samples are the same at the parton level. The selected events from both Monte Carlo samples are used as data, and the `KORALW` Monte Carlo sample with $M_{\mathrm{W}} = 80.25\,\mathrm{GeV}/c^2$ is used as a reference to fit the W mass.

The difference when fitting the common selected events ($\sim$ 3200 events) of both `EXCALIBUR` Monte Carlos (the presence of colour reconnection slightly affects the event selection) is shown in table 4.5.

	M_{W} with C.R.	M_{W} without C.R.	$M_{\mathrm{W}}^{C} - M_{\mathrm{W}}^{NC}$
m_1 (GeV/c^2)	80.266	80.295	−0.029
m_2 (GeV/c^2)	80.273	80.261	+0.012

Table 4.5: Fitted M_{W} with and without colour reconnection and mass differences.

In order to estimate the statistical error on the mass difference, the selected events are divided into 30 subsamples and the scaled RMS of the distribution of difference of estimators is found to be: $\frac{\text{RMS}}{\sqrt{30}} = 50\,\text{MeV}/c^2$. A systematic uncertainty of $\Delta M_\text{W} = -20 \pm 50\,\text{MeV}/c^2$ due to colour reconnection effects is quoted. The statistical error is taken as the systematic error.

4.10.12 Bose-Einstein effect

The possible existence of Bose-Einstein correlation effect (BE) between the two W's is pointed out as a source of systematic error on the W mass measurement in [104].

In order to determine the uncertainty coming from this effect of systematic, a global event weighting method described in [105] and implemented in a subroutine [106] as a weight per each event (w_i^{BE}), is developed.

To take into account this weight, the log-likelihood function is modified to be:

$$\mathcal{L}(M_\text{W}) = \sum_{i=1}^{N} w_i \cdot \log P_i \tag{4.16}$$

where $w_i = 1/w_i^{BE}$ and P_i are the reciprocal of the BE weight and the probability density function for the ith event as described in 4.6, respectively.

A sample of $\sim$ 7000 KORALW common selected events are fitted with and without Bose-Einstein effect. The results obtained are shown in table 4.6.

	M_W with BE	M_W without BE	$M_\text{W}^{BE} - M_\text{W}^{NBE}$
m_1 (GeV/c^2)	80.228	80.203	+0.025
m_2 (GeV/c^2)	80.325	80.297	+0.028

Table 4.6: Fitted W mass with and without BE reweighting and mass differences.

Similarly as for the colour reconnection systematic, the selected sample is divided into 50 subsamples in order to estimate the statistical error on the mass difference. The value obtained is: $\frac{\text{RMS}}{\sqrt{50}} = 40\,\text{MeV}/c^2$. A systematic uncertainty of $+26 \pm 40\,\text{MeV}/c^2$ is quoted. The largest error, the statistical, is taken as systematic error coming from Bose-Einstein effect: $\Delta M_\text{W} = 40\,\text{MeV}/c^2$.

For both colour reconnection and Bose-Einstein effects, the systematic error quoted is the statistical uncertainty of the estimated difference rather than the specific value of the difference observed.

Systematics summary

The different sources of systematic errors investigated in this analysis are summarised in table 4.7.

Source	ΔM_{W} (MeV/c^2)
Correlated errors	
MC fragmentation	10
Reference MC diagrams	3
Detector calibration	56
Jet corrections	40
W width	10
Initial State Radiation	15
LEP energy	30
Uncorrelated errors	
Reference MC statistics	30
Background contamination	20
Colour reconnection	-20 ± 50
Bose-Einstein effects	$+26 \pm 40$
Total	107

Table 4.7: Summary of systematic errors. The total systematic error is computed adding in quadrature all different sources.

4.11 Conclusions

A method to extract the W mass from W-pair events by reweighting Monte Carlo is proposed. The method is based on the direct comparison of the data mass distributions with those from Monte Carlo weighted events, thus providing the correct parameter to be identified with the W mass with no need of calibration.

Fully hadronic decays are selected by means of neural network techniques with high efficiency and low background contamination. The events are forced into four

jets and two invariant masses, one per di-jet, are reconstructed. A four-constraint plus rescaling fit is applied to improve the mass resolution. After choosing a jet pairing, the mass distributions are compared with reweighted Monte Carlo events, and the value of the W mass is extracted in a binned log-likelihood fit. extract the value of the W mass.

With $10.65\,\mathrm{pb}^{-1}$ collected by ALEPH in November 1996 and using only fully hadronic events, the W mass is measured to be:

$$81.18 \pm 0.47\,(\mathrm{stat}) \pm 0.10\,(\mathrm{syst})\ \mathrm{GeV}/c^2 \tag{4.17}$$

and it is published in [110].

Another method that was used was the second generation fitting formula [87]. The result is very much compatible with the one presented here, and has a 10% improvement in the statistical error. The method uses an optimal treatment of the combinatorial information, which is supposed to be the reason for the improvement.

Chapter 5

W mass measurement at 183 GeV

5.1 Introduction

A new energy of 183 GeV was reached by LEP in 1997. The integrated luminosity of 56.81 pb^{-1} collected by ALEPH at this unprecedent energy is used to precisely measure the mass of the W boson. It is obtained from reconstructed invariant mass distributions in W pair events. The method is similar to the one used for 172 GeV data: the direct reconstruction method using the reweighting technique. An improved jet pairing and a two-dimensional fit instead of one-dimensional fit are the new features from 172 GeV analysis of the previous chapter. The improvement are discussed in detail.

A more detailed study of colour reconnection and Bose Einstein W mass systematics are done trying to improve the systematic uncertainty.

The first section is devoted to the Monte Carlo samples used followed by the event selection. The clustering algorithm with the kinematical fitting are described in section 5.4. The extraction of the W mass as well as the detailed study of consitency checks and systematics studies come at the end of this chapter.

5.2 Monte Carlo samples

The same Monte Carlo packages as the ones used for the 172 GeV analysis are used. Slightly differently KORALW Monte Carlo (version 1.21), used to produce the

reference signal events with the complete set of four-fermion diagrams, is used with s-dependent running W and Z widths instead of fixed widths. As it was discussed in chapter 2, this implies a different definition of the W boson mass, and it has to be taken into account when producing the final W mass measurement for this data, to be able to combine both 172 and 183 GeV W mass measurements. The reference W mass value at which a big W^+W^- Monte Carlo production (400k events at a centre-of-mass of 183 GeV) is done is chosen to be as close as possible to the world average value: $80.35\,\mathrm{GeV}/c^2$. At this mass the decay width is calculated from Standard Model predictions with $\alpha_s = 0.118$. Four additional samples of 50k events each were generated with W masses of 79.85, 80.10, 80.60 and $80.85\,\mathrm{GeV}/c^2$ for checking ths stability of the results.

(20k of the production at $M_W = 80.35\,\mathrm{GeV}/c^2$ are used to train the neural network).

In addition, an independent sample of 100k signal events was generated with KORALW restricted to the doubly resonant CC03 diagrams with a cross-section of 15.71 pb.

Monte Carlo samples at 183 GeV with integrated luminosities corresopnding to at least 80 times that of the data, were fully simulated for all background reactions. PYTHIA was used to generate 500k $e^+e^- \to q\bar{q}(\gamma)$ events with a cross-section of 107.6 pb and also 20k Z^0Z^0 and 60k Z^0ee events. Events with a flavour content that could originate from W^+W^- production are explicitly rejected from the Z^0Z^0 sample to avoid double counting with the KORALW four-fermion production. The $e^+e^- \to We\nu$ process was simulated by PYTHIA with the electrons generated to smaller angles than the acceptance cut used in the production of the four-fermion events.

5.3 Event selection

At 183 GeV the main source of background in the hadronic channel is still $e^+e^- \to q\bar{q}(\gamma)$ production, followed by the Z^0Z^0 and $e^+e^- \to W^+W^- \to \ell\nu q\bar{q}$ processes.

The same initial requirements that were asked for the 172 GeV analysis called class 16 are applied as well in this analysis. However, the preselection is slightly

different. It has been optimized for The preselection cuts applied in this analysis are:

i. The longitudinal momentum p_L relative to the beam axis must satisfy: - $|p_L| \leq 0.95\ (M_{vis} - M_Z)$ where M_{vis} is the reconstructed invariant mass of all observed energy-flow objects (defined in 3.3.2) and M_Z is the mass of the Z boson;

ii. The sphericity (defined in appendix A.2) must be larger than 0.03;

The events are then forced into four jets using the DURHAM-P jet clustering algorithm (see Appendix A.1). Further preselection cuts are applied to these jets:

iii. The value of y_{34} (y_{cut} value when a four-jet event becomes three-jet) must be greater than 0.001;

iv. The fraction of electromagnetic to total energy in each jet has to be less than 0.95.

The first cut mainly acts against events with a real Z^0 and large initial state radiation (called radiative returns to the Z^0 events). The cut on sphericity takes into account that the global shape of a W^+W^- hadronic event is more spherical than $e^+e^- \to q\bar{q}(\gamma)$ events. The last cut allows to eliminate events with an initial state radiation photon emitted within the detector acceptance.

The main selection is based on a neural network as it was for the 172 GeV analysis. The neural network is updated and optimized for 183 GeV and trained using the new Monte Carlo samples. It uses 19 input variables (instead of 21), 17 hidden units and one output unit (19-17-1). The neural network output ranges from -1, assigned to background events, and $+1$, assigned to signal events. The full set of variables together with their discriminant power (defined in Appendix A.4) is given below:

Global event properties (definitions in A.2):

– Missing energy in the event; (4.4%)
– Sum of squared momenta of all charged tracks in the event; (4.1%);
– Sphericity; (3.9%)

– Fox-Wolfram moment H0; (4.4%)
– Fox-Wolfram moment H2; (4.7%)
– Fox-Wolfram moment H4. (10.1%)

Heavy Flavour tagging:

– Sum of the b-tag probabilities [1] for the four jets. (5.7%)

The following jet related variables are determined from kinematically fitted jet momenta (see section 5.4) leading to an improvement in discriminating power of the network.

Properties of Jets:

– Number of good tracks [2] in the most energetic jet; (6.1%)
– Largest energy fraction carried by one energy-flow object in the most energetic jet; (3.7%)
– Largest energy fraction carried by one energy-flow object in the second most energetic jet; (4.6%)
– Largest energy fraction carried by one energy-flow object in the third most energetic jet; (4.7%)
– Sum of angles between the leading track and all the tracks in the most energetic jet; (5.5%)
– Sum of angles between the leading track and all the tracks in the second most energetic jet. (3.6%)

W^+W^- Kinematics:

– Total energy of the most energetic jet; (8.1%)
– Total energy of the second most energetic jet; (3.8%)
– Momentum of the most energetic jet; (5.5%)
– Sum of the cosines of the six angles between the jets; (8.7%)
– Cosinus of the angle between the second and the third most energetic jets; (4.6%)
– Asymmetry between the second and the third most energetic jets. (3.8%)

[1] The b-tag probability was defined in section 4.3.
[2] A good track was already defined in section 4.3.

As the goal is to reconstruct di-jet invariant masses, none of the input variables of the neural network depend on them.

The separation between signal and background performed by the neural network output is shown in figure 5.1. By requiring the neural network output larger than -0.3, the signal events are selected with an effiency of 88.9% and a purity of 82.1%.

Figure 5.2 shows the selection efficiency from the total sample of W^+W^- events as a function of the W mass. As it was in the analysis of 172 GeV , there is no dependence as wanted.

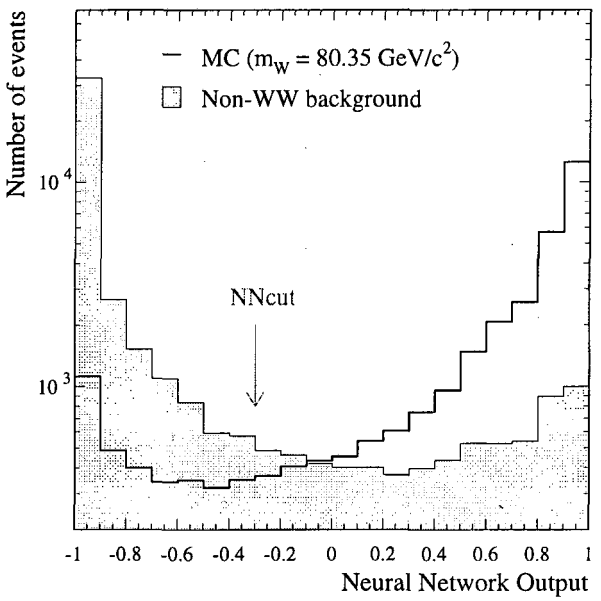

Figure 5.1: Neural network output for signal events generated with a $M_W = 80.35\,\mathrm{GeV}/c^2$ (open histogram) and background events – $q\bar{q}(\gamma)$, Z^0Z^0 – (full histogram). Both histograms are normalised to the same luminosity. The arrow indicates where the cut to select $e^+e^- \to W^+W^- \to 4q$ events is applied to the neural network output: -0.3.

Tables 5.1 and 5.2 gives the number of events surviving the class 16 requirements as well as the events surviving the neural network cut for the different W^+W^- channels and for the background respectively.

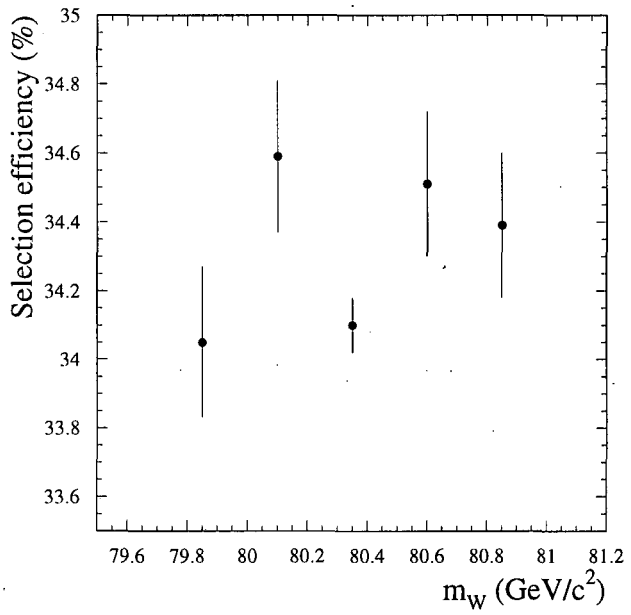

Figure 5.2: Selection efficiency as a function of the W mass.

5.4 Jet clustering and kinematical fit

Following the same procedure developed previously for the 172 GeV analysis, the DURHAM-PE jet clustering algorithm is used to find four jets in the event and a 4C + Rescaling kinematical fit is used to improve their resolution. The MATHKINE package where the parametrization is recalculated using the Monte Carlo at 183 GeV , is again used to do the fit.

A study done with the high statistics of $Z \rightarrow q\bar{q}$ events from LEP1 enables the simulation of the response of the detector to be determined for jet energies which lie in the medeian range of those reconstructed from W^+W^- hadronic decays before kinematic fitting is applied. These studies show that 46 GeV jets are well simulated at all values of θ with the largest discrepancy ($\sim 1.5\%$) being in the overlap region between barrel and endcaps (see figure 5.3). Avarage correction coefficients derived from these Monte Carlo studies are then applied to the measured jet momenta and directions before the fit. The corrections are most significant in the regions of the detector close to the beam axis. In the fitting procedure, these coefficients are allowed to vary from their average values and have been defined so that for each bin in jet energy and θ the deviations are Gaussian with minimal correlations.

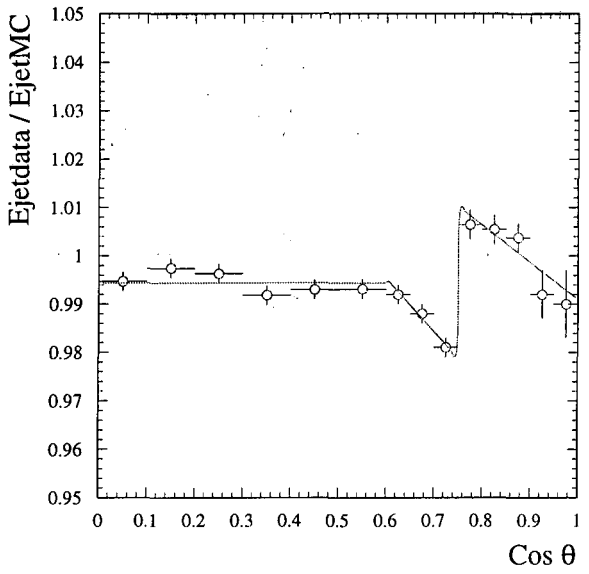

Figure 5.3: Avarage correction to be applied to the measured jet momenta and directions of the jets in the Monte Carlo.

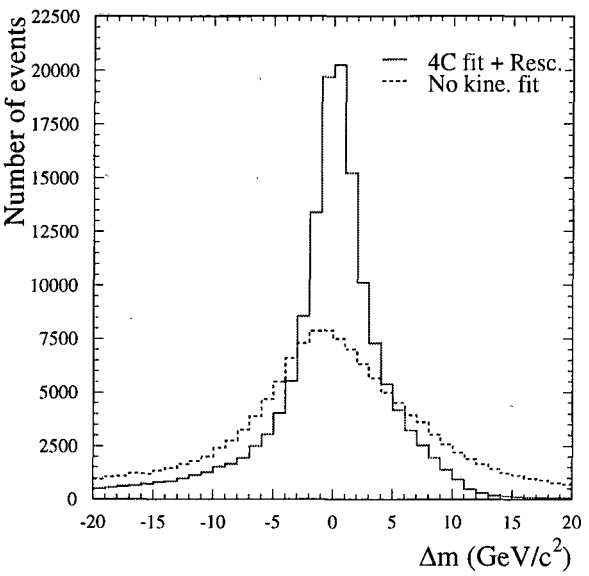

Figure 5.4: W mass resolution (reconstructed mass minus generated mass) when not doing any kinematical fit and when applying a 4C+R fit. The reconstructed masses correspond to the correct di-jet pair.

The improvement of the fit is shown in figure 5.4 where a comparison between the difference of truth and reconstructed masses without fitting and with the 4C+R fit is done.

In tables 5.1 and 5.2 the number of signal and background events for which the fit has converged are shown. Most of the events in the semileptonic W^+W^- channel that has survived the neural network cut, do not fit because they are not natural four jets and they have missing energy.

5.5 Jet pairing

One of the three ways in which the four jets of the selected events can be coupled into two-jets is chosen. The way found to be the most efficient of correct di-jet pairs assignment is a jet pairing improved from the one that was used in the previous analysis.

This jet pairing algorithm is an improved 'Angles' scheme (see section 4.6) that makes use of the second best combination when the first one does not fulfill the requested conditions.

The selected jet pairing is the combination with the smallest difference between the two rescaled masses unless this combination has the smallest sum of the two di-jet opening angles. In such a case, the combination with the second smallest mass difference is selected. The combination with the third smallest mass difference is never considered. Both masses for the selected combination must lie within a mass window 60-86 GeV/c^2 and at least one of the two masses must be between 74 and 86 GeV/c^2. If this condition fails then the second combination is accepted instead provided its two masses satisfy the window criteria; otherwise the event is rejected.

The combination is selected using the following algorithm:

1. The combination with the smallest difference between the two rescaled masses.
   (a) In the case this combination does not coincide with the one having the smallest sum of the two di-jet opening angles, it is chosen.
   (b) On the contrary, the combination with the second smallest mass difference is chosen.

2. A second condition involving both masses of the selected combination is required:

   (a) Both masses must lie within the mass window 60-86 GeV/c^2 and at least one of them in the window 74-86 GeV/c^2.

   (b) If (a) fails then:

      i. In the case of first combination: the second one is chosen if it fulfills the window masses conditions (a) and do not have the smallest sum of angles. If not, the event is rejected

      ii. Otherwise, the event is rejected.

This jet pairing happens to have minimal systematic bias on the final W mass value. The fraction of kinematically fitted signal Monte Carlo events surviving these criteria is 87%, of which 76% are found to have the correct combination.

The order of the two masses in the selected combination is then randomised to avoid correlation arising energy ordering effects in the analysis.

The number of events surviving the jet pairing criteria for W^+W^- events and background events are shown in tables 5.1 and 5.2 respectively. A final efficiency of 74% and purity of 86% is obtained after all the selection process.

Process	$W^+W^- \to 4q$	$W^+W^- \to 2q\ell\nu$	$W^+W^- \to 2\ell\nu$
Generated events	173967	164503	41530
Class 16	173416	163908	515
N.N. cut	148238	1608	0
Convergence fit	148213	853	0
Jet Pairing	128946	641	0
Efficiency (%)	74.12 ± 0.11	0.39 ± 0.02	0
σ^{eff} (pb)	5.41	0.03	0.

Table 5.1: Number of events surviving cuts, final efficiencies and effective cross-sections for the different W decays: $4q$ hadronic, $2q\ell\nu$ semileptonic and $2\ell\nu$ leptonic channels. The events are generated with a $M_W = 80.35\,\mathrm{GeV}/c^2$ four fermion KORALW Monte Carlo.

Process	$q\bar{q}(\gamma)$	Z^0Z^0
Generated events	500000	20000
Class 16	449742	13988
N.N. cut	5589	1280
Convergence fit	5530	1275
Jet pairing	3882	853
Efficiency (%)	0.78 ± 0.01	4.27 ± 0.14
σ^{eff} (pb)	0.84	0.13

Table 5.2: Number of events surviving cuts, final efficiencies and expected observable cross-sections for the most important background processes. Other processes are negligible after the selection.

5.6 Extraction of the W mass

A binned Monte Carlo reweighting procedure developed in the previous analysis and explained in section 4.7 is employed to find the value of M_W which best fits the observed invariant mass distributions. Selected Monte Carlo signal events from the large four fermion KORALW Monte Carlo sample are reweighted using CC03 matrix elements according to the single parameter to be fitted, M_W. The W width is set to $2.09\,\mathrm{GeV}/c^2$ for a mass of $80.35\,\mathrm{GeV}/c^2$ and varies with M_W as described in equation 2.6. Background Monte Carlo samples are included in the fit.

In the analysis at 172 GeV data, the reweighting procedure was applied to two rescaled mass distributions independently (denoted the 1-D method). The final mass was the weighted average taking into account the correlation between the two fitted masses obtained from a large number of Monte Carlo subsamples.

The higher statistics at 183 GeV allow a 2-dimensional reweighting to be performed with the two rescaled masses per event (denoted the 2-D method). The event-by-event correlations in the data are then properly accounted for and lead to an improvement in statistical precision discussed later 5.8.1. Using a binned 2-dimensional probability density function, a log-likelihood fit is now performed to the data within the mass wndows of 60-86 GeV/c^2 defined by the pairing algorithm. The small residual background (0.4%) of semileptonic events is also reweighted.

The probability density function for an event having two masses: m_1 between

bins i and $i+1$, and m_2 between bins j and $j+1$ is given by:

$$p.d.f.(m_i \leq m_1 < m_{i+1}, m_j \leq m_2 < m_{j+1} | M_{\mathrm{W}}) = \rho_s(M_{\mathrm{W}}) \frac{N_s^{ij}(M_{\mathrm{W}})}{\Delta m_i \Delta m_j N_{TOT}^s} + \rho_b(M_{\mathrm{W}}) \frac{N_b^{ij}}{\Delta m_i \Delta m_j N_{TOT}^b} \tag{5.1}$$

where Δm_i and Δm_j are the sizes of the bins: $m_{i+1} - m_i$ and $m_{j+1} - m_j$ respectively, ρ_s is the signal purity, ρ_b is the purity of the background, $N_s^{ij}(M_{\mathrm{W}})$ is the weighted number of signal events from the reference Monte Carlo in the reconstructed 2D mass bin, ij:

$$N_s^{ij}(M_{\mathrm{W}}) = \sum_{k=1}^{n_s^{ij}} w_k(M_{\mathrm{W}}) \tag{5.2}$$

(n_s^{ij} being the number of signal events from the reference Monte Carlo found in bin ij) and N_b^{ij} is tht total number of background events found in the same bin. N_{TOT}^s and N_{TOT}^b are respectively:

$$N_{TOT}^s = \sum_{i=1}^{N_{bin}^1} \sum_{j=1}^{N_{bin}^2} N_s^{ij}(M_{\mathrm{W}}); \qquad N_{TOT}^b = \sum_{i=1}^{N_{bin}^1} \sum_{j=1}^{N_{bin}^2} N_b^{ij} \tag{5.3}$$

where N_{bin}^1, N_{bin}^2 are the number of bins in the two reconstructed mass dimensions.

The purity is defined as in equation 4.10 where the dependence of the cross section on the W mass is parametrised using the GENTLE package as:

$$\sigma_s(M_{\mathrm{W}}) = \sigma_s(M_{\mathrm{W}}^{ref}) \left(1 - 0.0071(M_{\mathrm{W}} - M_{\mathrm{W}}^{ref}) - 0.0025(M_{\mathrm{W}} - M_{\mathrm{W}}^{ref})^2\right). \tag{5.4}$$

The likelihood function to be minimized in order to obtain the W mass which best fits the data is:

$$\mathcal{L}(M_{\mathrm{W}}) = \prod_{k=1}^{N_{evt}} p.d.f.(m_1^k, m_2^k \mid M_{\mathrm{W}}) \tag{5.5}$$

N_{evt} being the number of selected events which enter in the minimization and have m_1^k and m_2^k invariant masses.

The size of the binning needs a more careful study as the 2D probability density functions suffer more from statistical fluctuations than the 1D one. For this reason, as both mass distributions m_1 and m_2 are the same (and randomized), double events: m_1 vs. m_2 and m_2 vs. m_1 are accounted in the 2D mass distribution. Detailed checks are explained below.

5.6.1 Binning of the 2D mass distribution

In figure 5.5 the two dimensional distribution for KORALW Monte Carlo signal events is shown. The way to bin this distribution takes into account the fact that there are three differently populated regions:

- $74 \leq m_1 < 86$ and $74 \leq m_2 < 86$ is the most populated region.
- $60 \leq m_1 < 74$ and $74 \leq m_2 < 86$ is not as populated as the first one and it is called 'wing region 1'.
- $74 \leq m_1 < 86$ and $60 \leq m_2 < 74$ is as populated as 'wing region 1' and it is called 'wing region 2'.

The binning used in the 2D mass distribution is a projection in both dimensions of the binning found in the 1D mass distributions. The 1D binning is obtained by projecting independently the 2D mass distributions of the three different regions and requiring the same amount of events in each 1D bin. The binning is obtained for signal and for summed background ($q\bar{q}(\gamma)$ and Z^0Z^0) independently.

In figure 5.6 the binning of all the regions for signal and background are shown. It is important to note that for the background, the regions are similarly populated as, by definition, the background does not depend on the W mass. Consequently, the binning is similar in all the regions. It is not the same case for the signal and the most populated region has the thinest binning.

The binning projection into 2D is shown in figure 5.7 for both signal and background.

The requirement to this binning in order to have a reliable calculation of the probability density function is to have a minimum number of events per each 2D bin. Some Monte Carlo studies have been performed in order to know this number.

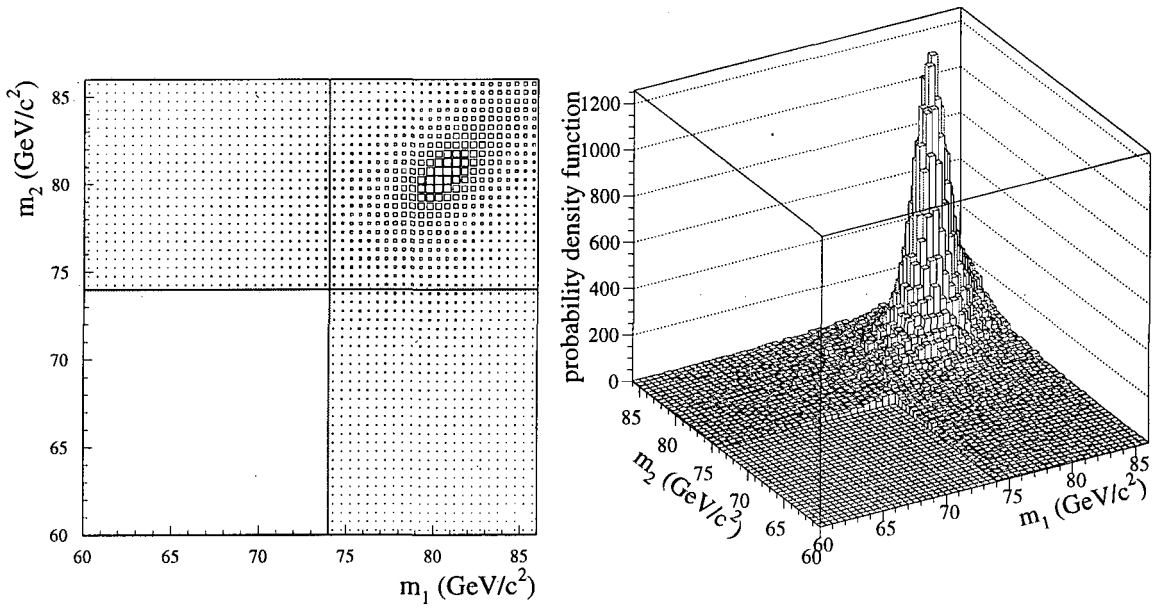

Figure 5.5: Two dimensional reconstructed mass distribution for four fermion KORALW Monte Carlo generated with a $M_W = 80.35\,\mathrm{GeV}/c^2$ selected events.

A study of the expected statistical error (RMS spread) by doing the fit of 200 independent Monte Carlo subsamples each with the same number of events as the data taken is performed depending on the number of minimum events required per each bin. The plot is shown in figure 5.8. The error is stable from a required minimum number of events of 60.

Another check has been done by looking to the linearity of the method. The slope and the origin coordinate of the calibration curve are computed in terms of this minimum number of events, with the same conclusion (figures 5.9).

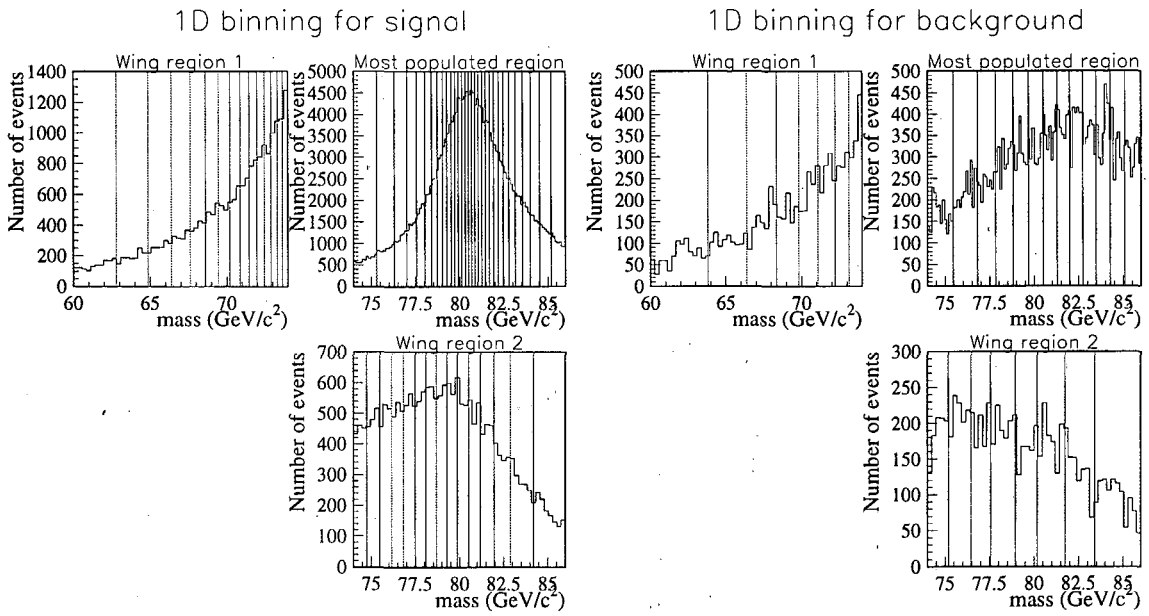

Figure 5.6: One dimensional binning to be projected into the 2D mass distribution per each region: on the left, for the signal events and on the right, for background events.

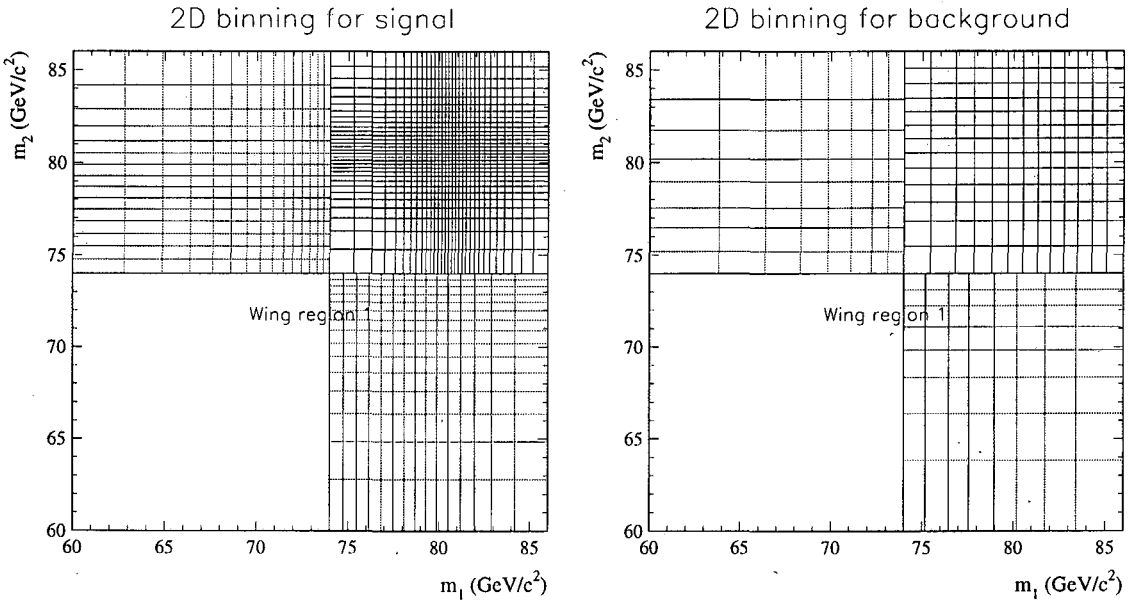

Figure 5.7: Variable binning applied to the 2D reconstructed mass distribution to compute the probability density function. On the left, the variable binning applied to the signal, and on the right to the background.

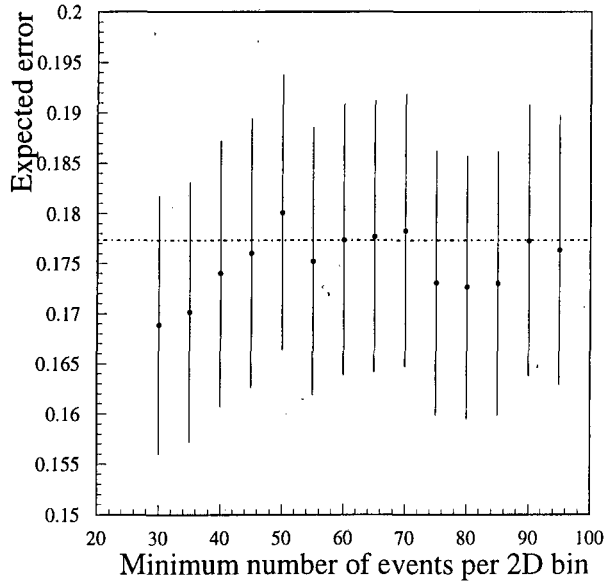

Figure 5.8: Expected error distribution in terms of the minimum number of events per 2D bin required.

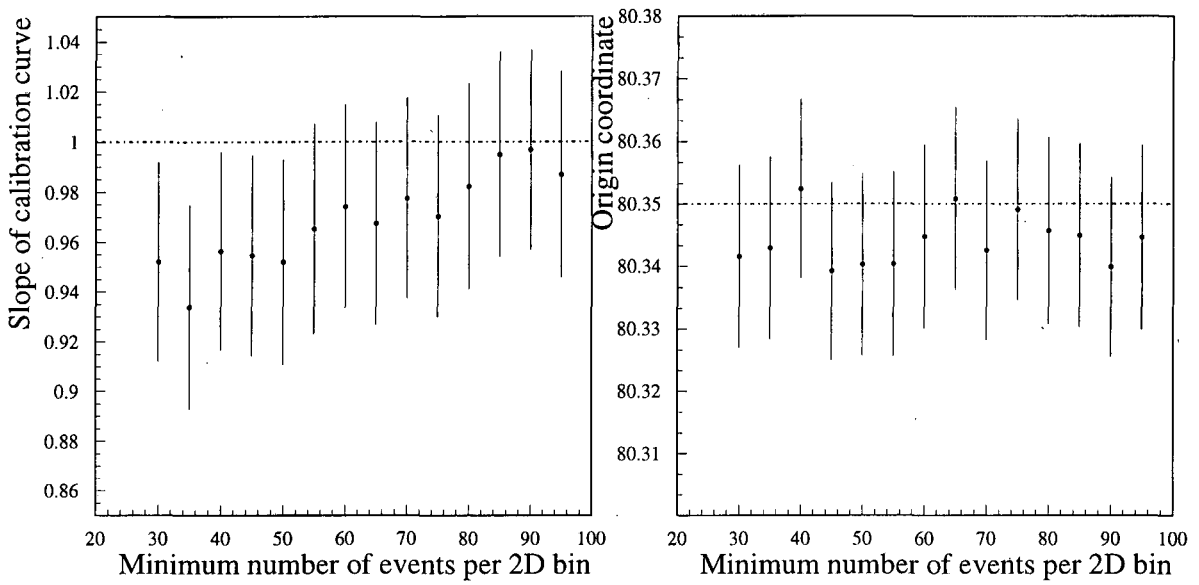

Figure 5.9: Slope and origin coordinate of the calibration curve in terms of the minimum number of events per 2D bin required.

5.7 Monte Carlo expectation

5.7.1 Expected error

The statistical error in M_W is computed from the single fit to the data distribution. Also, a large number of Monte Carlo subsamples are studied, each with the same

number of events as the data, to evaluate the expected error from the RMS spread of fitted masses and the ditribution of fit errors obtained.

5.7.2 Calibration curve

The amount of bias is checked by using five independent Monte Carlo samples generated with different M_{W} (over the range $79.85-80.85\,\mathrm{GeV}/c^2$) with background events in the adequate proportion. Figure 5.10 shows the fitted masses as a function of the generated ones. A straight line, $\hat{m} = P_1 + P_2(M_{\mathrm{W}}^{true} - 80.35)$, is fitted to the points. The result of the fit together with the ideal line, $\hat{m} = M_{\mathrm{W}}^{true}$ are shown as well. The fitted line is compatible with the ideal line, checking the linearity of the method.

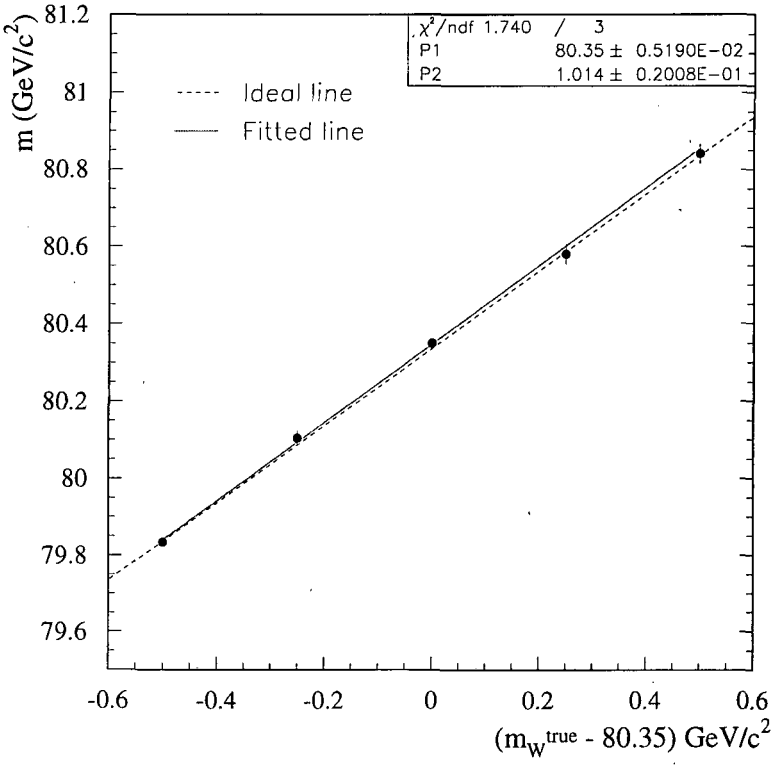

Figure 5.10: Fitted mass versus generated mass for five Monte Carlo samples of $1450\,\mathrm{pb}^{-1}$ each.

5.8 W mass measurement

The 2D invariant mass distribution is reweighted to best fit the selected events of the data collected at 183 GeV.

The number of selected events of the data following the selection described in the previous sections is 383, compared with 367.5 Monte Carlo predicted events (312.9 signal and 54.6 background events). The 2D reconstructed mass distribution for the selected data is shown in figure 5.11. Their correlation is found to be $(21.2 \pm 4.9\%)$. When taking only the range where both masses are in the window $74 - 86\,\mathrm{GeV}/c^2$, the correlation is found to be $(30.7 \pm 5.2\%)$.

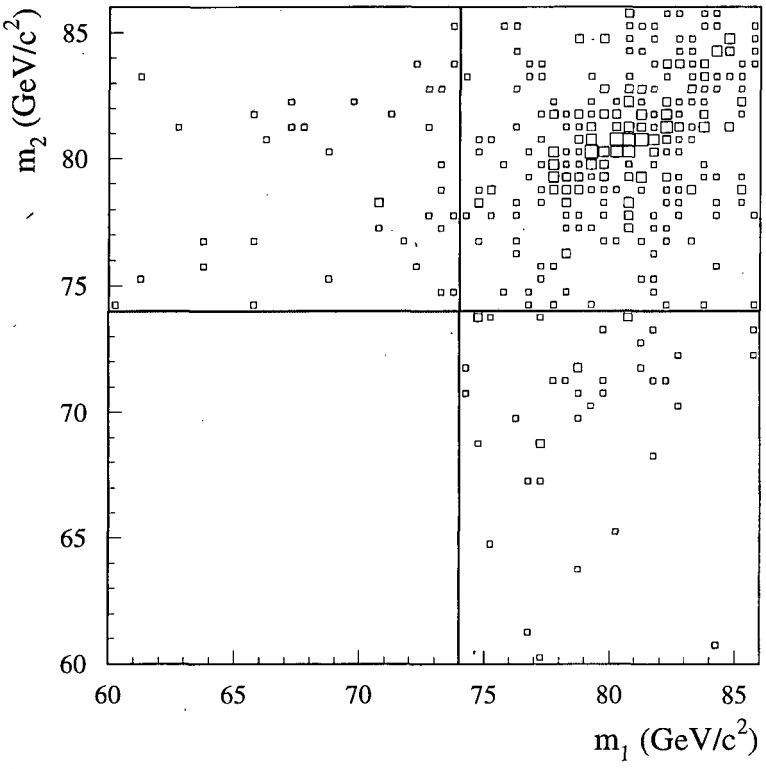

Figure 5.11: 2D invariant mass distribution for the selected data.

The mass value with statistical error obtained from the fit of this 2D distribution

to the one reweighted from a reference Monte Carlo generated at 80.35 GeV/c^2 is:

$$M_{\mathrm{W}} = 80.410 \pm 0.178\,\mathrm{GeV}/c^2 \tag{5.6}$$

5.8.1 Check with the 1D method

A check is performed by using the 1D method. Both m_1 and m_2 values are found to be:

$$\begin{aligned} m_1 &= 80.395 \pm 0.246\,\mathrm{GeV}/c^2 \\ m_2 &= 80.422 \pm 0.277\,\mathrm{GeV}/c^2 \end{aligned}$$

with an expected correlation of 27%. Combining both results with this correlation, the W mass value obtained is:

$$m = 80.406 \pm 207\,\mathrm{GeV}/c^2.$$

Comparing the statistical error using this 1D method, with the one using the 2D method, an improvement of $\sim$ 15% using the 2D method is obtained. The W mass result from both methods are compatible.

Figure 5.12 shows the 1D mass distribution (m_1 and m_2 combined) for the selected data events. The Monte Carlo distributions for the fitted mass, $M_{\mathrm{W}} = 80.41\,\mathrm{GeV}/c^2$ as well as the background Monte Carlo distribution are shown.

5.8.2 Checks of the mass window and the neural network output cut

Some checks of the stability of the result as a function of the neural network cut output and as a function of the window mass of the pairing have been performed. Concerning the checks of the fit of the data as a function of the window mass, some different checks have been done: depending on the low mass of the first window ([74−86]), depending on the low mass of the second window ([60-86]), and depending on the windows high mass. Consistent results have been obtained for each of these checks. Figure 5.13 shows the check of the data fit and the expected

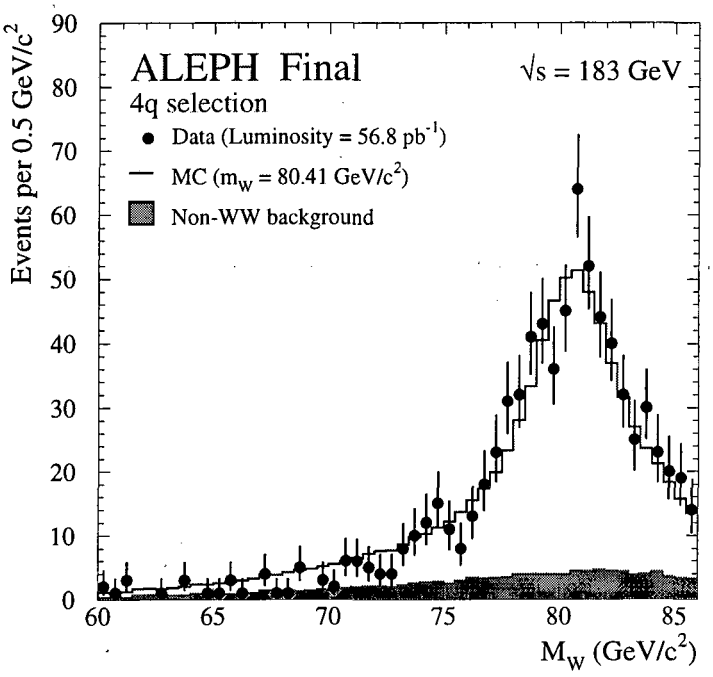

Figure 5.12: Mass distribution (m_1 and m_2) for hadronic data (points with error bars), background Monte Carlo (shaded area) and signal+background Monte Carlo for the best fit to the data taken at 183 GeV (empty histogram).

error when changing the minimum mass of the first window. It has been checked as well that consistent results are obtained when changing the neural network output cut (see figure 5.13).

5.9 Systematic uncertainties

5.9.1 Finite reference Monte Carlo statistics

The finite number of Monte Carlo events used as a reference in the reweighting method contributes a systematic uncertainty. The method used in the 172 GeV analysis subdivides the Monte Carlo reference sample into smaller samples of equal size and then used as reference and fitted to the same data. However, the result

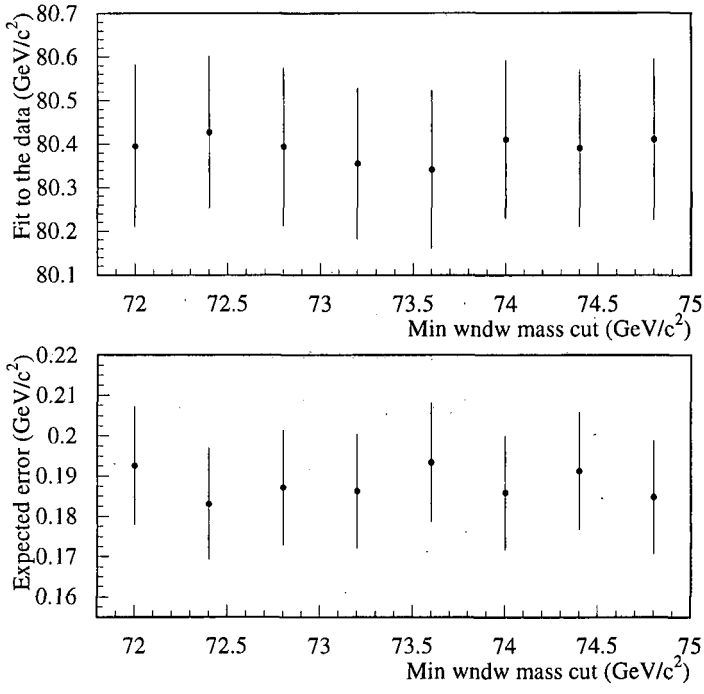

Figure 5.13: Dependence of the fit of the data and the expected error on the minimum window mass cut.

relies upon an extrapolation to one sample and is less precise than a second method based on a calculation of the statistical uncertainty in M_W evaluated from the atual number of Monte Carlo events used. Since the Monte Carlo events are used in bins, this calculation has been performed by combining the uncertainty that is obtained in each bin, taking into accoun bin-by-bin efficiencies after all analysis steps and the effective number of events allowing for the reweighting procedure. The formula of these procedure are explained in detail in appendix B. The systematic uncertainty obtained using this method is $\Delta M_W = 10\,\mathrm{MeV}/c^2$. This number is found to be compatible with the one computed by doing subsampling.

5.9.2 Monte Carlo fragmentation parameters

Different Monte Carlo fragmentation packages are used to study this systematic: `JETSET` and `HERWIG`. By changing the `JETSET` fragmentation parameters an effect of $\leq 10\,\mathrm{MeV}/c^2$ is obtained. However, a more significant effect is found when replacing

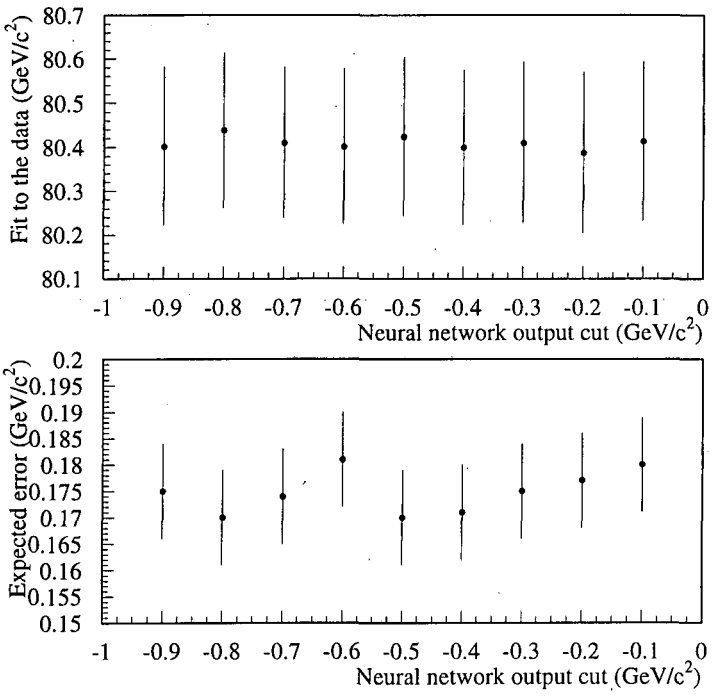

Figure 5.14: Dependence of the fit of the data and the expected error on the neural network output cut.

JETSET by HERWIG to hadronise the partons generated in an independent sample of 400k W^+W^- events. The HERWIG fragmentation parameters are optimised at the Z by using all hadronic events without flavour selection. This new reference sample of HERWIG events is then compared with the default JETSET sample in the reweighting procedure. A large number of Monte Carlo subsamples of the same size as the data are used and the fitted masses obtained reweighting with each reference sample above are compared. The average shift is quoted as the systematic error. The subsamples are derived from the primary reference of 380k W^+W^- events. A systematic uncertainty of 35 MeV/c^2 is found.

5.9.3 Background estimation

The method to quote this systematic is the same as the one used for 172 GeV data. In this case, the expected background contamination after all analysis cuts is 15%, and the background shape is almost flat (see figure 5.12). By re-applying

the discrepancies found in the comparison between Monte Carlo and data at the Z peak, to the 2D mass distribution, an uncertainty of $10\,\mathrm{MeV}/c^2$ is obtained. Both background shape and normalization uncertainties are taken into account.

5.9.4 Calorimeter calibrations

The uncertainties in the global calibrations of ECAL and HCAL energy were assessed to be $\pm 0.9\%$ and $\pm 2\%$ respectively. The energy-flow depositions in the data are varied in each direction by these uncertainties. The maximum shifts seen in M_{W} for each calorimeter adjustment for the common selected data sample are added in quadrature. The systematic uncertainty obtained is $\Delta M_{\mathrm{W}} = 22\,\mathrm{MeV}/c^2$.

5.9.5 Jet corrections before the kinematic fit

To estimate this systematic error, two modified parametrisations which accomodate $\pm 1\sigma$ errors in the discrepancies found in matching reconstructed Monte Carlo jets to data ($\pm 1\sigma$ of the function in figure 5.3), are evaluated. By applying these modified parametrisations to correct jet energies to the data, different M_{W} values are obtained. The largest shift observed between these values and the one with no corrections, is taken as the systematic uncertainty. Common selected data events are used to fit. An error of $\Delta M_{\mathrm{W}} = 10\,\mathrm{MeV}/c^2$ is obtained.

5.9.6 Initial state radiation

The same method used in the 172 GeV data is appied in here. A sample of KORALW events is fitted with a weight per event corresponding to the ratio of first to second order squared matrix elements: $\mathcal{O}(\alpha^1 L^1)/\mathcal{O}(\alpha^2 L^2)$. This value is compared to M_{W} value obtained with unweighted events, and a shift of $\Delta M_{\mathrm{W}} = 10\,\mathrm{MeV}/c^2$ is found and taken as systematic uncertainty.

5.9.7 Colour reconnection

The colour reconnection effect is studied by using Monte Carlo models based on variants of the parton evolution schemes JETSET and HERWIG both of which have

been optimised at the Z. The different models are explained in detail in section 2.6.1.

PYTHIA models

For the JETSET study, a sample of 45k $W^+W^- \rightarrow 4q$ is generated (with the EXCALIBUR Monte Carlo) and then hadronised in different ways to create:

1. a fully simulated sample with no colour reconnection;
2. three other samples labelled types I, II and II' (following the description of section 2.6.1).

In type I, all events are reconnected according to the degree of string overlap. A reconnection probability, $\mathcal{P}_{reco}$, is defined as [28]:

$$\mathcal{P}_{reco} = 1. - \exp^{-0.6 \cdot \phi} \tag{5.7}$$

where ϕ is the overlap between strings. The factor 0.6 seems to be a reasonable number for this model [112]. Figure 5.15 shows $\mathcal{P}_{reco}$ for all generated events.

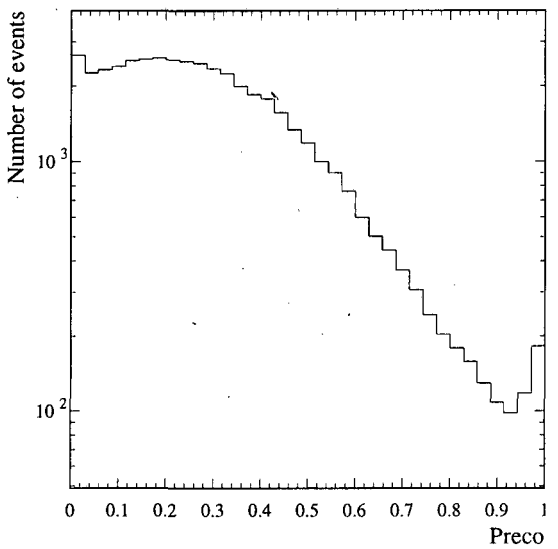

Figure 5.15: Reconnection probability values, $\mathcal{P}_{reco}$, for EXCALIBUR Monte Carlo generated events.

The fact that in this model all events are reconnected is considered unrealistic. Consequently, the events are required to fulfill: $\mathcal{P}_{reco} > \mathcal{P}_{cut}$, where $\mathcal{P}_{cut}$ value varies from 0% (all events are reconnected) to 50% (only 14% of the events are reconnected). The events that do not fulfill this requirement are replaced by the corresponding ones with no colour reconnection. The systematic is taken as the difference between the fit of the non reconnected sample and the fit of the sample that results after the cut. Figure 5.16 shows the value of the systematic uncertainty when varying the value of the cut, $\mathcal{P}_{cut}$, as well as the percentage of reconnected events corresponding to each cut.

A reasonable number of reconnected events is 40%, which corresponds to the value of 0.3 for $\mathcal{P}_{cut}$. Thus, the systematic quoted from this study is $\Delta M_{\mathrm{W}} = 25 \pm 21\,\mathrm{MeV}/c^2$. The error is estimated by doing 40 samples of the same size.

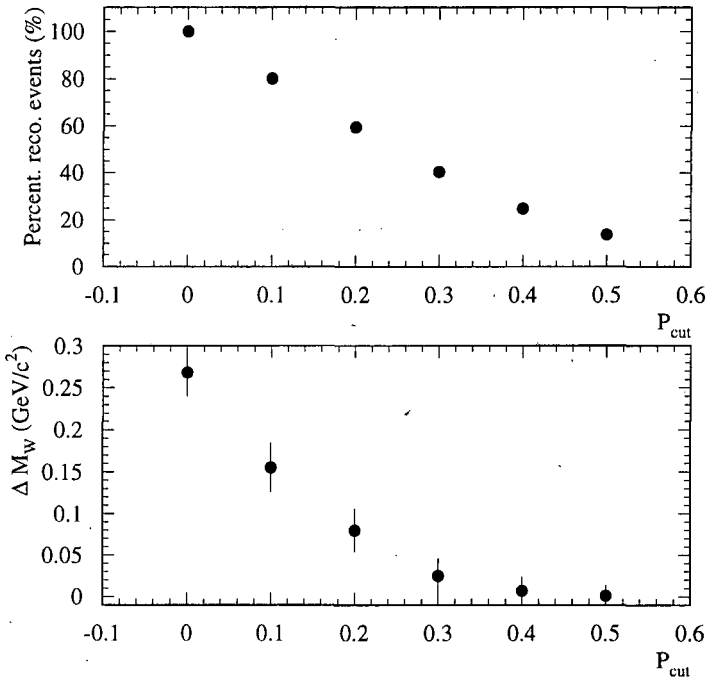

Figure 5.16: Above: percentage of reconnected events after applying the cut: $\mathcal{P}_{reco} > \mathcal{P}_{cut}$ for different values of $\mathcal{P}_{cut}$. Below: Colour reconnection systematic uncertainty using model I when varying the value of $\mathcal{P}_{cut}$ from 0 to 0.5.

Model type II, where the reconnection occurs at the crossing of two vortex lines, predicts only $\sim$ 27% reconnected events. For the rest of the events the non colour

reconnected event is taken instead when fitting all the sample. The systematic uncertainty found with this model is $\Delta M_W = 5 \pm 15\,\mathrm{MeV}/c^2$, smaller than the one found for model I.

Model type II', similar to type II except that the reconnection is suppressed if there is no reduction of the string lenght, predicts $\sim 24.4\%$ reconnected events. Computing the systematic the same way as for model type II, the systematic uncertainty is found to be $\Delta M_W = 17 \pm 15\,\mathrm{MeV}/c^2$.

Figure 5.17 shows the differences between the mass distributions of reconnected and non reconnected events for model types II and II'.

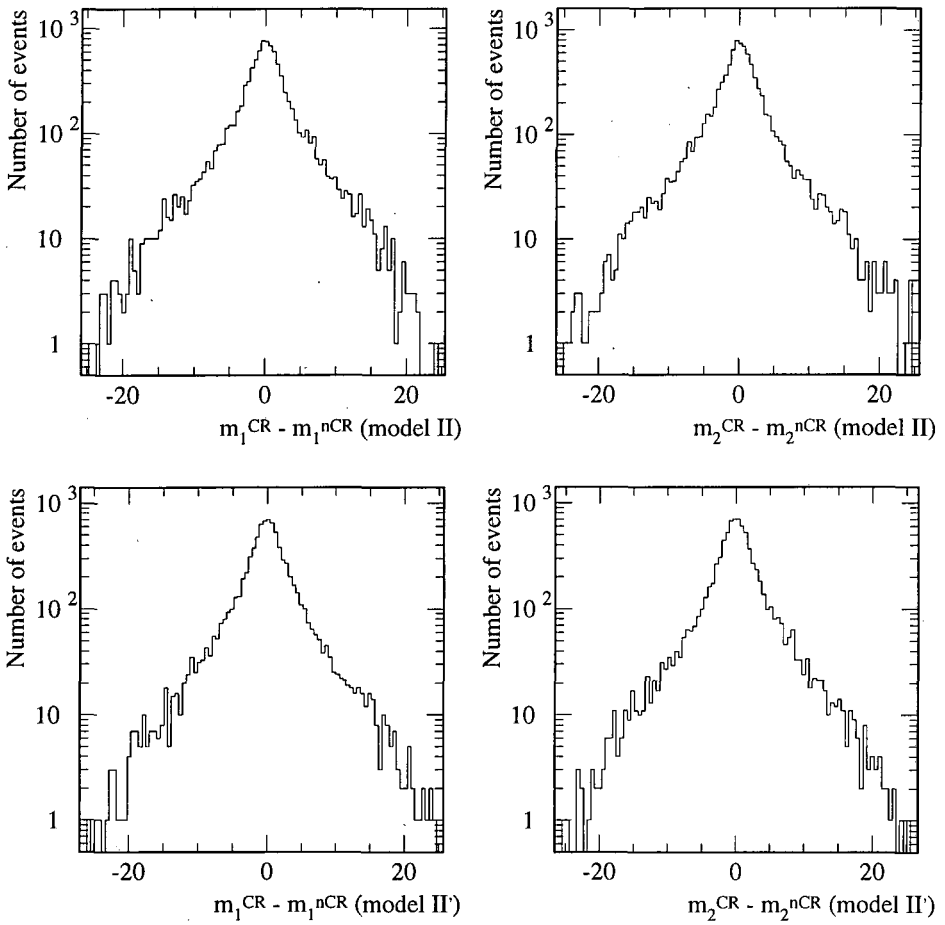

Figure 5.17: Differences between the mass distributions of reconnected and non reconnected events for model types II and II' and for both m_1 and m_2.

HERWIG models

For the HERWIG models, W^+W^- events are generated using HERWIG also for the generation of partons. Three different samples of 50k are fully simulated with the *PRECO* parameter (different from $\mathcal{P}_{reco}$ in equation 5.7), defining the level of reconnection probability, set to 0%, 11% and 60% (this last one supposed to be unrealistic) respectively. The events are not identical at the primary parton level and therefore the invariant masses derived for each case are subject to statistical fluctuations. The shifts obtained relative to the 0% reconnected sample are -10 and $-31\,\mathrm{MeV}/c^2$ respectively with errors of $\pm 25\,\mathrm{MeV}/c^2$ in each case.

The VNI model [29] has not been used to estimate a systematic error because its current implementation does not reproduce the predicted dependence of the charged event multiplicity on the minimum angle between jets from different W bosons, particle momentum distributions, and the mean value of the charged multiplicity at detector level seen in the data [113].

In conclusion, none of these models, as applied, predicts a significant effect on M_W. The largest uncertainty of $25\,\mathrm{MeV}/c^2$ found in the JETSET based models is taken as the quoted systematic error.

5.9.8 Bose-Einstein effect

Two separate studies are made each using two different approaches described in section 2.6.2.

In the first, the weighting method already used in the 172 GeV analysis is implemented using a KORALW Monte Carlo sample of 60k events generated with $M_W = 80.35\,\mathrm{GeV}/c^2$. The Bose-Einstein strength and source radius parameters are set to values found in a recent analysis of LEP1 data [114]: $\lambda = 0.26 \pm 0.04$ and $\sigma = 4.12 \pm 0.17\,\mathrm{GeV}^{-1}$. In figure 5.18 the distribution of weights for $W^+W^- \to 4q$ selected events is shown.

The results obtained are in table 5.3. A downdrift of $43 \pm 25\,\mathrm{MeV}/c^2$ is observed.

The second study is based on KORALW generated events with hadronisation handled by a modified PYTHIA where the Bose-Einstein correlations are implemented by shifts in the momenta of identical final state particles whilst ensuring that energy-

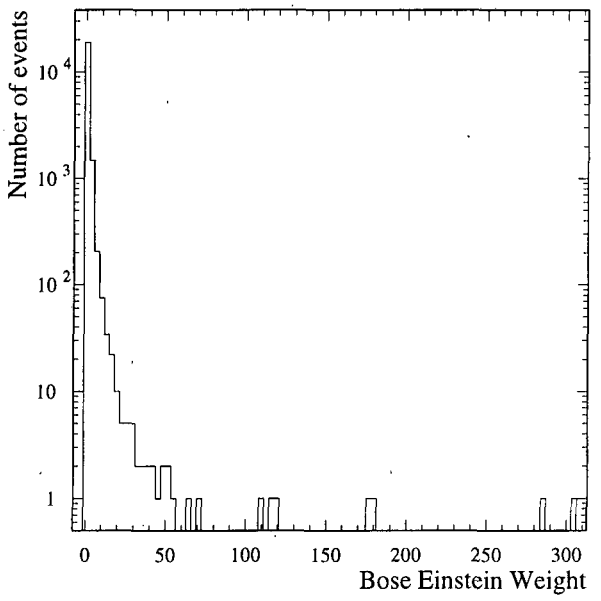

Figure 5.18: Bose-Einstein weight distribution for selected events.

	M_{W} with BE	M_{W} without BE	$M_{\mathrm{W}}^{BE} - M_{\mathrm{W}}^{NBE}$
M_{W} (GeV/c^2)	80.307	80.350	−0.043

Table 5.3: Fitted W mass when weighting and not, and mass difference.

momentum conservation is satisfied (model B_3 from [33]). The strength and source radius parameters are obtained from fits to Z data and for this model $\lambda = 2.2$ and $R = 0.23\,\mathrm{GeV}$ [114].

Two different samples are generated: one with correlations restricted to identical bosons within de same W, and another one where correlations between particles from different Ws are also allowed.

Figure 5.19 shows the difference between mass distribution for one sample and the other.

The RMS spread of the differences in mass when subsampling is used to determine the error on the uncertainty. A shift in M_{W} of $50 \pm 25\,\mathrm{MeV}/c^2$ is observed between the fit of both samples. The larger shift is taken as the quoted systematic error: $\Delta M_{\mathrm{W}} = 50\,\mathrm{MeV}/c^2$.

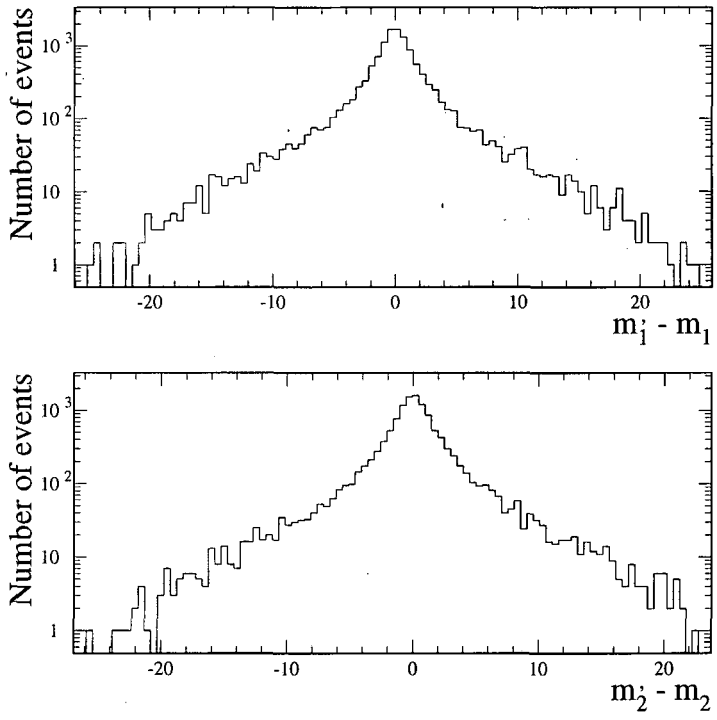

Figure 5.19: Difference between mass distributions from the sample with Bose-Einstein correlations within de same W (m_1 or m_2) and the sample that has, in addition, correlation between Ws (m_1' or m_2').

5.9.9 LEP energy

The LEP beam energy is recorded every 15 minutes, and more frequently if significant shifts are observed in the RF frequency of the accelerating cavities. The instantaneous values recorded nearest in time to the selected events are used to rescale the masses in this analysis. Consequently, the relative uncertainty on the LEP energy translates into the same relative uncertainty on the fitted mass. For the quoted LEP beam energy uncertainty of $\Delta E_b = 25\,\mathrm{MeV}$ [115], a systematic uncertainty of $\Delta M_\mathrm{W} = 22\,\mathrm{MeV}/c^2$ is assigned (using formula 4.15). This is quoted separately from the other experimental systematic errors to be able to easily combine the results with the other three LEP experiments.

Systematics summary

The different sources of systematic errors investigated in this analysis are summarised in table 5.4.

Source	ΔM_W (MeV/c^2)
Correlated errors	
MC fragmentation	35
Detector calibration	22
Jet corrections	10
Initial State Radiation	10
LEP energy	22
Uncorrelated errors	
Reference MC statistics	10
Background contamination	10
Colour reconnection	25
Bose-Einstein effects	50
Total	72

Table 5.4: Summary of systematic errors. The total systematic error is computed adding in quadrature all different sources.

5.10 Conclusions

The W mass value obtained by using a 2D reweighting method applied to 183 GeV data in the hadronic channel is:

$$M_W = 80.410 \pm 0.178(\text{stat}) \pm 0.045(\text{syst.}) \pm 0.056(\text{BE/CR})\text{GeV/c}^2 \quad (5.8)$$

and has been presented in Vancouver [116] and is going to be published.

The quoted theoretical error (BE/CR) is taken from Bose-Einstein and Colour Reconnection systematics added in quadrature.

Chapter 6

W mass combination

The combination of the W mass mesurements for the different leptonic channels is done energy by energy and experiment by experiment. Afterwards, these results are combined with the hadronic channel again energy by energy and experiment by experiment, taking into account correlated and uncorrelated systematics.

The combination of the results obtained from direct reconstruction (at 172 and 183 GeV energies) for the hadronic channel (4.17 and 5.8) gives a W mass value of:

$$M_{\mathrm{W}} = 80.53 \pm 0.18\,\mathrm{GeV}/c^2\ ,$$

where statistic and systematic errors are added in quadrature.

When combining this result with the one obtained with the semileptonic channels, the result for the W mass measured by ALEPH by the direct reconstruction method is:

$$M_{\mathrm{W}} = 80.44 \pm 0.13\,\mathrm{GeV}/c^2\ .$$

The combination of all direct reconstruction results of the four LEP experiments gives [117]:

$$M_{\mathrm{W}} = 80.36 \pm 0.09\,\mathrm{GeV}/c^2$$

with a χ^2 per degree of freedom of 1.07/3. The value of the W mass measured at LEP after the combination with the W mass determination from the WW cross-section at threshold is:

$$M_{\mathrm{W}}^{\mathrm{LEP}} = 80.37 \pm 0.09\,\mathrm{GeV}/c^2\ ,$$

in very good agreement with the W mass measurement coming from the hadron colliders (see figure 6.1). The combination of both measurements gives a world average W mass value of [118]:

$$M_{\mathrm{W}}^{W.A.} = 80.39 \pm 0.06\,\mathrm{GeV}/c^2\,. \tag{6.1}$$

The combination of the $\sin^2\theta_{\mathrm{W}}$ results coming from the measurements of neutrino-nucleon experiments: CCFR [119] and NuTeV [120] (the NuTeV measurement is twice as precise as the measurement by CCFR) is:

$$\sin^2\theta_{\mathrm{W}} = 0.2255 \pm 0.0021$$

and translates to an indirect W mass measurement [1] compatible with the world average value (see figure 6.1).

By performing a global electroweak fit using as input the Z^0 measurements from LEP/SLC, the $\sin^2\theta_{\mathrm{W}}$ from νN experiments, and the m_t from CDF and D0, the M_{W} obtained is shown in figure 6.1, compatible again with the world average value. The Higgs mass obtained is [118]:

$$\log_{10} m_{\mathrm{H}} = 1.96^{+0.33}_{-0.42} \qquad m_{\mathrm{H}} = 92^{+101}_{-57}\ \mathrm{GeV/c^2}\,.$$

with a χ^2 per degree of freedom of 16.2/13. After including the direct measurements of M_{W} the fit to all data gives:

$$\log_{10} m_{\mathrm{H}} = 1.92^{+0.32}_{-0.41} \qquad m_{\mathrm{H}} = 84^{+91}_{-51}\ \mathrm{GeV/c^2}\,.$$

[1] The neutrino-nucleon (νN) scattering experiments measure the neutral-current (NC) to charged-current (CC) cross-section ratio. To reduce systematics a measure of:

$$R^- = \frac{\sigma^{\nu}_{NC} - \sigma^{\bar{\nu}}_{NC}}{\sigma^{\nu}_{CC} - \sigma^{\bar{\nu}}_{CC}}$$

is performed instead. The Paschos-Wolfenstein relation [121] relates this ratio to $\sin^2\theta_{\mathrm{W}}$ in the on-shell renormalization scheme, and is (at lowest order):

$$R^- = \frac{1}{2} - \sin^2\theta_{\mathrm{W}}$$

where:

$$\sin^2\theta_{\mathrm{W}} = 1 - \frac{M_{\mathrm{W}}^2}{M_{\mathrm{Z}}^2}$$

with a χ^2 per degree of freedom of 16.4/15. The one-sided 95% confidence level upper limit on M_{H} is $280\,\mathrm{GeV}/c^2$, not including the direct search results. The Higgs mass precision depends strongly on $\alpha(M_{\mathrm{Z}}^2)$.

Figure 6.2 shows the check of consistency between direct and indirect W mass versus top mass measurements. The contour plots are 68% confidence level, and the Higgs is varied from 90 to $1000\,\mathrm{GeV}/c^2$.

In the future, when the measurements were as precise as:

$$\begin{aligned} \delta(1/\alpha(M_{\mathrm{Z}}^2)) &= \pm 0.01 \\ \delta m_t &= \pm 2\,\mathrm{GeV}/c^2 \\ \delta M_{\mathrm{W}} &= \pm 30\,\mathrm{MeV}/c^2 \end{aligned}$$

a factor of 2.5 improvement in relative M_{H} error would be expected [7].

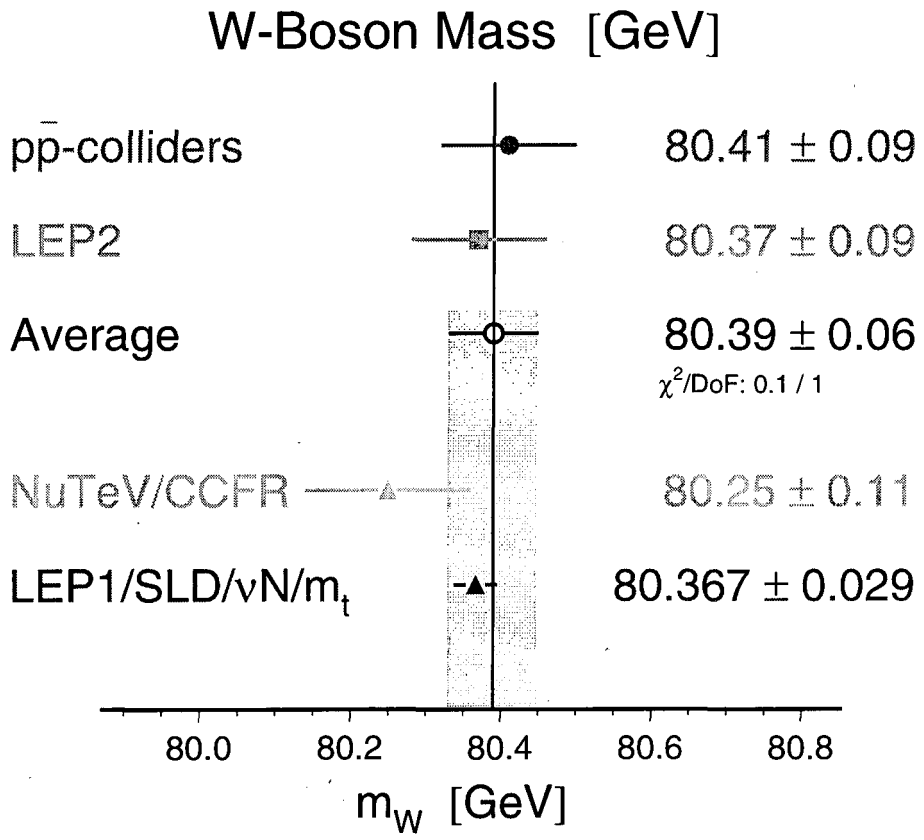

Figure 6.1: Comparison of W mass boson results between direct and indirect measurements (presented at the ICHEP in Vancouver in July 1998).

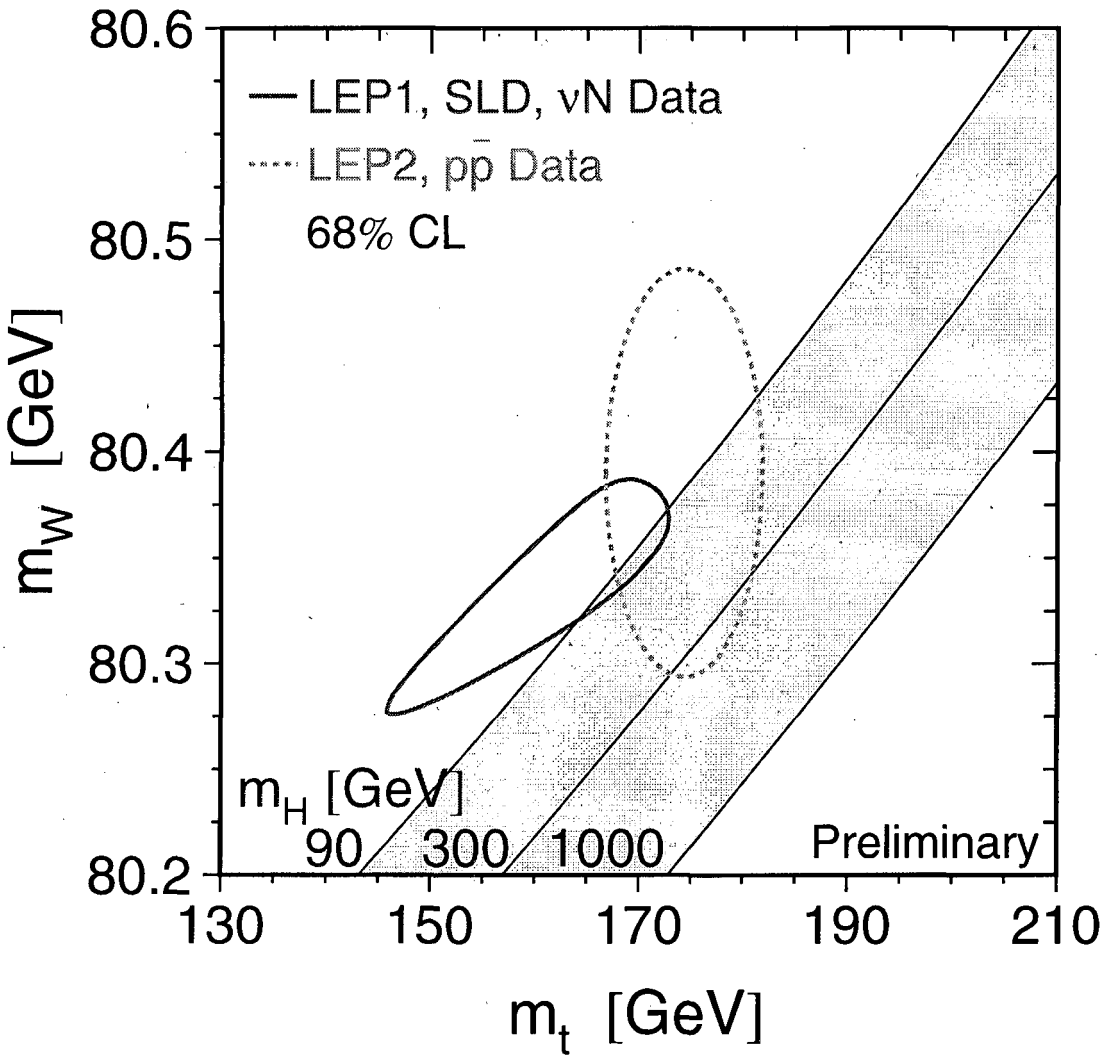

Figure 6.2: Indirect and direct measurements of the W mass and m_t (68% confidence level contour plots), compared with the Standard Model prediction for various values of M_{H} (from 90 to 1000 GeV/c^2).

Chapter 7

Summary and conclusions

The W mass in the fully hadronic channel using the data collected by ALEPH at centre-of-mass energies of 172 GeV and 183 GeV has been measured.

At 172 GeV, the W mass has been measured by using the direct reconstruction method. Due to the similarity between the hadronic decay channel events and the background events, a neural network has been used for the selection. After the clustering of the jets, a kinematical fit has been done to improve their resolution. Afterwards a jet pairing found to be the best in correctly assigning jets to partons was applied. The probability density function has been extracted from a reference Monte Carlo reweighted with the ratio of squared matrix elements of the reference W mass and any other W mass value. The two invariant mass distributions of the Monte Carlo were reweighted independently to find the corresponding W mass values, which were combined afterwards with the correct correlation of the two estimators to extract the W mass. No calibration curve was needed using this method.

At 183 GeV, the W mass has been extracted using the same technique as before. A new feature was applied in the reweighting technique trying to reduce the statistical error: The method has been applied to both invariant mass distributions at the same time, automatically taking into account the correlation between the two estimators. The W mass value was extracted without having to combine. This method was found to improve the statistical error by 10%.

The combination of both measurements gave a W mass value coming from the hadronic channel of $M_{\mathrm{W}} = 80.53 \pm 0.18\,\mathrm{GeV}/c^2$. After the combination of the other

measurements coming from the LEP experiments and the hadron colliders a world average value with an accuracy of $60\,\mathrm{MeV}/c^2$ is achieved. The comparison to the indirect W mass measurements coming from LEP1/SLD and the νN experiments has been done and compatible results were found. An upper-bound limit to the Higgs boson mass using this world-average value has been found to be $280\,\mathrm{GeV}/c^2$.

Appendix A

Hadronic events analysis

A.1 Jet finding

A description of some of the most commonly used cluster algorithms follows in this first appendix.

Initially, each final-state particle is considered to be a cluster. Using some distance measure (this will differ from one algorithm to another), the two nearest clusters are found. If their distance is smaller than some cut-off value, the two clusters are joined into one. In this new configuration with one cluster less, the two clusters that are now nearest are found and joined, and so on until all clusters are separated by a distance larger than the cut-off. This cut-off is called y_{cut}. The clusters remaining at the end are called **jets**.

Another usual way of finding jets without using a cut-off is to join the clusters till a predetermined number of jets is reached. This is the method used in both 172 and 183 GeV analyses, and the number of jets asked for is four.

The different definitions of the distance between clusters determine the different **cluster algorithms**:

- DURHAM algorithm [72]:

$$d_{ij}^2 = 2(\min(\mathrm{E_i}, \mathrm{E_j}))^2(1 - \cos\theta_{\mathrm{ij}}) \tag{A.1}$$

- JADE algorithm [71]:

$$d_{ij}^2 = 2\mathrm{E_i}\mathrm{E_j}(1 - \cos\theta_{\mathrm{ij}}) \tag{A.2}$$

– LUCLUS algorithm [73]:

$$d_{ij}^2 = \frac{4|\mathbf{p_i}|^2|\mathbf{p_j}|^2\sin^2(\theta_{ij}/2)}{(|\mathbf{p_i}||\mathbf{p_j}|)^2} \tag{A.3}$$

where $E_i, E_j, \mathbf{p_i}, \mathbf{p_j}$ are the energy and momenta of two different clusters and θ_{ij} is the angle between them.

The circumstance that different algorithms can be used is not an ambiguity of the theory. Instead, it just reflects the fact that it exists a certain amount of freedom in the definition of a jet.

In order to combine the nearest clusters, different **schemes** are available for all cluster algorithms:

E-scheme:
$$\begin{aligned} \mathbf{p}_{ij} &= \mathbf{p}_i + \mathbf{p}_j \\ E_{ij} &= E_i + E_j \end{aligned}$$

P-scheme:
$$\begin{aligned} \mathbf{p}_{ij} &= \mathbf{p}_i + \mathbf{p}_j \\ E_{ij} &= |\mathbf{p}_{ij}| \end{aligned}$$

E_0-scheme:
$$\begin{aligned} E_{ij} &= E_i + E_j \\ \mathbf{p}_{ij} &= \frac{E_{ij}(\mathbf{p}_i + \mathbf{p}_j)}{|\mathbf{p}_i + \mathbf{p}_j|} \end{aligned}$$

where $E_{ij}, \mathbf{p}_{ij}$ are the energy and momentum of the resulting sum of the *ith* and *jth* clusters.

The E-scheme is Lorentz invariant while the P and E_0-schemes have to be applied in the laboratory frame.

A.2 Global event shape variables

To describe the complicated geometries encountered in multihadronic events, a number of measures are introduced. These measures are intended to provide a global view of the properties of a given event, wherein the full information content of the event is condensed into one or a few numbers.

These quantities are required to be *infrared* and *collinear* safe. Infrared safe means that the quantity in question should not change abruptly if one adds one

soft particle to the final state, while collinear safe means that the quantity does not change abruptly if one splits one particle in the final state into two particles sharing proportionally its momentum.

Sphericity and aplanarity

The sphericity tensor is defined as:

$$S_{\alpha\beta} = \frac{\sum_i p_i^\alpha p_i^\beta}{\sum_i |\mathbf{p}_i|^2}, \tag{A.4}$$

where α, β=1,2,3 corresponds to the x, y and z components. By diagonalizing this tensor one may find three eigenvalues $\lambda_1 \geq \lambda_2 \geq \lambda_3$, with $\lambda_1 + \lambda_2 + \lambda_3 = 1$. The **sphericity** ($S$) of the event is then defined as:

$$S = \frac{3}{2}(\lambda_2 + \lambda_3), \tag{A.5}$$

so that $0 \leq S \leq 1$. Sphericity is essentially a measure of the summed $\mathbf{p}_\perp^2$ with respect to the event axis. A 2-jet event corresponds to $S \approx 0$ while an isotropic event to $S \approx 1$.

The sphericity tensor is quadratic in particle momenta. This means that the sphericity value is changed if one particle is split up into two collinear ones which share the original momentum. Thus sphericity is not a collinear safe quantity but it is an infrared safe quantity.

Eigenvectors $\mathbf{v}_i$ corresponding to the eigenvalues λ_i of the spheriticy tensor can be found. The $\mathbf{v}_1$ is called the sphericity axis, while the sphericity event plane is spanned by $\mathbf{v}_1$ and $\mathbf{v}_2$.

A measure of the transverse momentum component out of the event plane is called **aplanarity** (A). It is defined as:

$$A = \frac{3}{2}\lambda_3 \tag{A.6}$$

The constrained range is $0 \leq A \leq \frac{1}{2}$. A planar event has $A \approx 0$ while an isotropic one $A \approx \frac{1}{2}$.

Thrust abd oblateness

The quantity **thrust** (T) is defined by:

$$T = \max_{|\mathbf{n}|=1} \frac{\sum_{\mathrm{i}} |\mathbf{n} \cdot \mathbf{p}_{\mathrm{i}}|}{\sum_{\mathrm{i}} |\mathbf{p}_{\mathrm{i}}|}, \tag{A.7}$$

when the sum runs over all final state particles and $\mathbf{n}$ is the vector for which the maximum thrust value is attained. The allowed range is $1/2 \leq T \leq 1$, with a 2-jet event corresponding to $T \approx 1$ and an isotropic event to $T \approx 1/2$.

In the plane perpendicular to the thrust axis, a major axis and value may be defined in just the same fashion as thrust, i.e.

$$M_a = \max_{|\mathbf{n}|=1, \mathbf{n}\cdot\mathbf{v}_i=0} \frac{\sum_{i} |\mathbf{n} \cdot \mathbf{p}_i|}{\sum_{i} |\mathbf{p}_i|}.$$

The minor axis is defined perpendicular to the thrust and major axis, and a minor value M_i is calculated just as thrust and major. **Oblateness** is defined as the difference between major and minor:

$$O = M_a - M_i. \tag{A.8}$$

The upper limit on oblateness depends on the thrust value in a not so simple say. In general $O \approx 0$ corresponds to an event symmetrical around the thrust axis and high O to a planar object.

Fox-Wolfram moments

The Fox-Wolfram moments $H_l, l = 0, 1, 2, ...$, are defined by:

$$H_l = \sum_{i,j} \frac{|\mathbf{p}_i||\mathbf{p}_j|}{E_{vis}^2} P_l(\cos\theta_{ij}), \tag{A.9}$$

where θ_{ij} is the opening angle between hadrons i and j and E_{vis} the total visible energy of the event. The $P_l(x)$ are the Legendre polynomials.

To the extent that particle masses may be neglected, $H_o \equiv 1$. It is customary to normalize the results to H_0, i.e. $H_{l0} = H_l/H_0$. If momentum is balanced then $H_1 \equiv 0$. 2-jet events tend to give $H_l \approx 1$ for l even and $H_l \approx 0$ for l odd.

A.3 Kinematic fitting

The constrained fit package used in the hadronic channel to improve the di-jet invariant mass resolution is called MATHKINE [77] and it is explained here. The method is general and allows all measured quantities to vary in order to fulfil a set of constraints.

The procedure that is adopted to minimise a function subject to constraints is the use of Lagrange multipliers [78]. A function (S) is defined as:

$$S(\vec{y},\vec{\lambda}) = (\vec{y}-\vec{y_0})^{\top}\,\mathbf{V}^{-1}\,(\vec{y}-\vec{y_0}) \;+\; 2\vec{\lambda}\cdot\vec{f}(\vec{y}) \tag{A.10}$$

where $\vec{y_0}$ is the expectation value of the fitted variables $\vec{y}$, $\mathbf{V}$ is the error matrix, $\vec{\lambda}$ are the Lagrange multipliers and $\vec{f}(\vec{y})$ is a vector containing the constraints written as functions that must vanish, i.e. $\vec{f}(\vec{y}) = \vec{0}$.

The problem of minimising $S(\vec{y},\vec{\lambda})$ reduces to solve simultaneously the equations:

$$\begin{aligned} \frac{\partial S}{\partial \vec{y}} &= \vec{0} \\ \frac{\partial S}{\partial \vec{\lambda}} &= \vec{0}. \end{aligned} \tag{A.11}$$

In order to construct a fast iterative procedure to find a minimum the constraints $\vec{f}(\vec{y})$ are linearised using a first-order Taylor expansion:

$$\vec{f}(\vec{y}) \approx \vec{f}(\vec{y}^{(l)}) \;+\; \left.\frac{\partial \vec{f}(\vec{y})}{\partial \vec{y}}\right|_{\vec{y}=\vec{y}^{(l)}} \cdot (\vec{y}-\vec{y}^{(l)}). \tag{A.12}$$

Defining $\mathbf{B}$ as:

$$\mathbf{B} = \left.\frac{\partial \vec{f}(\vec{y})}{\partial \vec{y}}\right|_{\vec{y}=\vec{y}^{(l)}} \tag{A.13}$$

and replacing $\vec{y}$ by $\vec{y}^{(l+1)}$, equation A.10 can be written as an iterative equation:

$$S(\vec{y}^{(l+1)},\vec{\lambda}) = (\vec{y}^{(l+1)}-\vec{y_0})^{\top}\,\mathbf{V}^{-1}\,(\vec{y}^{(l+1)}-\vec{y_0}) + 2\vec{\lambda}\cdot(\vec{f}(\vec{y}^{(l)}) + \mathbf{B}\,(\vec{y}^{(l+1)}-\vec{y}^{(l)})). \tag{A.14}$$

Substituting equation A.14 into equation A.11 and after some algebra the following equations are found:

$$\begin{aligned} \mathbf{V}^{-1}\,(\vec{y}^{(l+1)}-\vec{y_0}) + \mathbf{B}^{\top}\vec{\lambda} &= \vec{0} \\ \vec{f}(\vec{y}^{(l)}) + \mathbf{B}\,(\vec{y}^{(l+1)}-\vec{y}^{(l)}) &= \vec{0}, \end{aligned} \tag{A.15}$$

which can be written as:

$$\begin{pmatrix} \mathbf{V}^{-1} & \mathbf{B}^{\top} \\ \mathbf{B} & \mathbf{0} \end{pmatrix} \begin{pmatrix} \vec{y}^{(l+1)} \\ \vec{\lambda} \end{pmatrix} = \begin{pmatrix} \mathbf{V}^{-1}\vec{y_0} \\ -\vec{f}(\vec{y}^{(l)}) + \mathbf{B}\vec{y}^{(l)} \end{pmatrix}. \tag{A.16}$$

After some algebra a recursion formula for determining $\vec{y}^{(l+1)}$ is obtained:

$$\vec{y}^{(l+1)} = \vec{y_0} + \mathbf{V}\mathbf{B}^{\top}(\mathbf{B}\mathbf{V}\mathbf{B}^{\top})^{-1} \left(\mathbf{B}\,(\vec{y}^{(l)} - \vec{y_0}) - \vec{f}(\vec{y}^{(l)})\right). \tag{A.17}$$

This recursion formula converges and minimizes $S(\vec{y}, \vec{\lambda})$ if the distribution of each parameter y_i is close to a Gaussian.

It is possible to take into account initial state radiation and Breit-Wigner mass distributions in the constrained fit by including in the equation A.10 a function $g(x)$, which only depends on a scalar variable and represents a penalty function and, following the likelihood concept, takes the form $-2\ln(p(x))$ ($p(x)$ is a probability distribution function connected to the variables $\vec{y}$ via constraints: $x - f(\vec{y}) = 0$) [79].

A.4 Neural Network Description

Neural Networks (NN) are useful tools for pattern recognition [107]. In high energy physics, they have been used or proposed as good candidates for tasks of signal versus background classification as the information carried by many variables is used at the same time (multidimensional method). The multidimensional Neural Net technique allows to handle non-linear classification problems, which cannot be solved by using linear cuts in the variables and allows also to treat the correlations between the different variables in an optimal way.

In the case of the hadronic W^+W^- channel selection, the neural network is used to distinguish two similar type of events: $e^+e^- \rightarrow W^+W^- \rightarrow 4q$ (signal) and $e^+e^- \rightarrow q\bar{q}(\gamma)$ (background). It is a very efficient way to improve the purity and efficiency results.

A.4.1 Description of a multilayered feed forward neural network

A multilayered feed forward neural network (MLNN) used for pattern recognition needs several levels or layers. Each neuron of a level (l) is directly connected with all neurons of the following level ($l+1$) but there is no connection with the neurons of the same layer. The strength of each connection is described by a weight. A typical architecture is shown in figure A.1. All of the i neurons of the network will

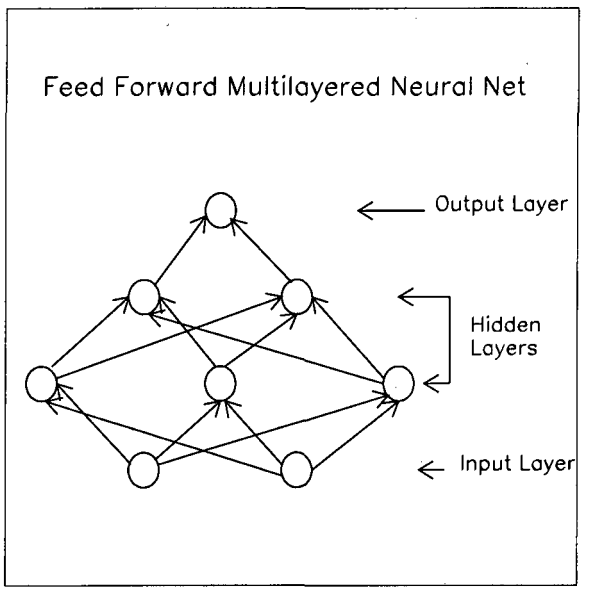

Figure A.1: Typical architecture of a feed forward multilayered neural network.

give an ouput O_i by performing a weighted sum of the O_j outputs of the j neureons they are connected with.

A MLNN used for pattern recognition will operate in three phases ("backpropagation" learning):

1. Supervised learning: events belonging to each class are presented to the system to train it to recognize their features. The class of the event is given as input at this stage. The weights connecting neurons are determined by using the gradient descent method [108].

2. Validation step: checking the ability of the network already trained to recognize events it has never seen before. Therefore, another sample of events is presented to the network without class indication.

3. The system is finally used to perform an event by event classification on real experimental events.

The learning consists in tuning the weight values, a positive weight being an excitation and a negative weight being an inhibition of the neurons.

An optimization of the architecture of the multilayered neural network is done taking into account that: the number of input units must be equal to the number of the selected discriminating variables; the number of output units is governed by the number of classes to be separated; and the number of hidden layers as well as the number of units per layer have to be optimized for the separation.

A.4.2 Optimizing the number of inputs

Information concerning the relative contribution of the different variables to the NN selection capability can be deduced from the weights values. In other words, connections with strong weights will lead to strong triggering of the ouput neuron unit which is bound to them. This is due to the fact that the weight values are continuously modified during the learning step by the backpropagation algorithm to give the best fit of the NN output for the classes to be separated.

To handle the information carried by the weight values W_{ij}, the vector S_{W_k} [109] is introduced such that:

$$S_{W_k} = \sum_{i=1}^{N_{hl}} |W_{ik}| \tag{A.18}$$

where N_{hl} is the number of neurons on the first hidden layer, and W_{ik} the weight of the connection between the input neuron k and the neuron i of the first hidden layer.

The bigger S_{W_k} the stronger the rôle of the variable k in the separation of $W^+W^- \rightarrow 4q$ and background events. This last quantity can be normalized by

taking:

$$S^*_{W_k} = \frac{S_{W_k}}{\sum_{k=1}^{N_V} S_{W_k}} \tag{A.19}$$

where N_V is the total number of variables of the input layer. This quantity $S^*_{W_k}$ gives the discriminant power of each variable and can be used to take out the less discrimating ones from the set originally chosen.

Appendix B

Monte Carlo Statistics Systematic calculation

The systematic uncertainty on the W mass due to the Monte Carlo statistics can be computed using the fact that each bin has different sensitivity. This is an analytical way to compute this systematic instead of doing Monte Carlo subsamples of the reference and extrapolating the fit to the data to one sample.

The sensitivity to each bin can be defined as:

$$\Delta M_W^i = \frac{\Delta\sigma_i}{\frac{\partial\sigma_i}{\partial M_W}} \tag{B.1}$$

where σ_i is the cross-section corresponding to the ith bin:

$$\sigma_i = \frac{N_i}{\mathcal{L}\cdot\epsilon} \tag{B.2}$$

and consequently:

$$\Delta\sigma_i = \frac{\sqrt{N_i}}{\mathcal{L}\cdot\epsilon} \tag{B.3}$$

where N_i is the number of events in the ith bin, $\mathcal{L}$ is the luminosity and ϵ is the selection efficiency.

The probability density function is defined as:

$$\rho_i(m) = \frac{1}{N_T}\cdot\frac{N_i}{\Delta m_i} \tag{B.4}$$

where N_T is the total number of events and Δm_i is the width of each bin in the plot of sensitivity versus invariant mass.

Deriving this probability in terms of M_W and making use of eq. B.2, the following equation is obtained:

$$\frac{\partial \rho_i}{\partial M_W} = \frac{1}{N_T} \cdot \frac{\partial}{\partial M_W}\left(\frac{N_i}{\Delta m_i}\right) = \frac{1}{\sigma_T \Delta m_i} \cdot \frac{\partial \sigma_i}{\partial M_W} \tag{B.5}$$

where σ_T is the total cross-section.

Making use of this last equation and eq. B.3, the error on M_W per each bin i is defined as:

$$\Delta M_W^i = \frac{1}{\Delta m_i \cdot \frac{\partial \rho_i}{\partial M_W} \cdot \frac{N_T}{\sqrt{N_i}}}, \tag{B.6}$$

By considering that all the errors are independent (this is an approximation but it is correct), the errors can be summed in quadrature for all the bins as:

$$(\Delta M_W^T)^2 = \frac{1}{\sum_i \left(\Delta m_i \cdot \frac{\partial \rho_i}{\partial M_W} \cdot \frac{N_T}{\sqrt{N_i}}\right)^2}. \tag{B.7}$$

This equation gives the systematic uncertainty due to Monte Carlo statistics, and it is used in the analysis of 183 GeV data.

Bibliography

[1] S.L. Glashow, Nucl. Phys. B22 (1961) 579;
S. Weinberg, Phys. Rev. Lett. **19** (1967) 1264;
A. Salam, *Elementary Particle Theory*, ed. N. Svartholm, Almqvist and Wiksell, Stockholm (1968) 367;

[2] S.L. Glashow, J. Iliopoulos and L. Maiani, Phys. Rev. **D2** (1970) 1285.

[3] G. 't Hooft, Nucl. Phys. **B33** (1971) 173.

[4] The LEP Collaborations (ALEPH, DELPHI, L3 i OPAL The LEP Electroweak Working Group and the SLD Heavy Flavour Group), *A combination of preliminary electroweak measurements and constraints on the Standard Model*, ALEPH internal report, ALEPH 98-037 PHYSICS 98-018, 15 May 1998.

[5] N. Cabbibo, Phys. Rev. Lett. **10** (1963) 531;
M. Kobayashi and K. Maskawa, Prog. Theor. Phys. **49** (1973) 652.

[6] Super-Kamiokande Collaboration, results presented at the Neutrino '98 Conference, Japan, 5 June 1998.

[7] M.W. Grünewald, Combined Analysis of Precision Electroweak Results, 29th ICHEP, Vancouver, July 1998.

[8] W. Beenakker and A. Denner, Int. J. Mod. Phys. **A9** (1994) 4837.

[9] V. Barger *et al.*Phys. Rev. **D28** (1983) 2912;
X. Tata, M. Drees, C.S. Kim, Phys. ReV. **D37** (1988) 784;
J. Terrón, T. Álvarez, A. Leites, Nucl. Phys. **B301** (1988) 1.

[10] A. Denner, Fortschr. Phys. **41** (1993) 307.

[11] T. Muta, R. Najima and S. Wakaizumi, Mod. Phys. Lett. **A1** (1986) 203.

[12] Z. Kunszt and W.J. Stirling, *Determination of the mass of thw W boson*, in Physics at LEP2, eds. G. Altarelli *et al.*. CERN Yellow Report 96-01 (1996) vol.1, 149.

[13] M. Consoli and A. Sirlin, in *Physics with LEP*, J. Ellis and R. Peccei (eds.), CERN 86-02 (1986) 63;
F. Jegerlehner, in *Testing the Standard Model*, M. Cvetič and P. Langacker (eds.), Proc. of the 1990 Theor. Adv. Study Inst. (World Scintific, Singapore, 1991), 476.

[14] D. Bardin, A. Leike, T. Riemann and M. Sachwitz, Phys. Lett. **B206** (1988) 539.

[15] U. Baur and D. Zeppenfeld, *Phys. Rev. Lett.* 75 (1995) 1002.

[16] M. Veltman, *Physica* **29** (1963) 186;
R.G. Stuart, *Phys. Lett.* **B262** (1991) 113;
A. Aeppli, G.J. van Oldenborgh and D. Wyler, *Nucl. Phys.* **B428** (1994) 126.

[17] W. Beenakker, in e^+e^- *Collisions at* 500 GeV*: The Physics Potential*, ed. P.M. Zerwas (DESY 92-123, Hamburg, 1992), part A, 195.

[18] W. Beenakker and F.A. Berends, *WW cross-sections and distributions*, in Physics at LEP2, eds. G. Altarelli *et al.*. CERN Yellow Report 96-01 (1996) vol.1, 79.

[19] J. Fleischer, F. Jegerlehner and M. Zralek, Zeit. Phys. **C42** (1989) 409;
K. Kolodziej, M. Kolodziej and M. Zralek, Phys. Rev. **D43** (1991) 3619;
J. Fleischer, F. Jegerlehner and K. Kolodziej, Phys. Rev. **D47** (1993) 830.

[20] M. Böhm *et al.*, Nucl. Phys. **B304** (1988) 463;
W. Beenakker, F.A. Berends and T. Sack, Nucl. Phys. **B367** (1991) 287;
W. Beenakker, K. Kolodziej and T. Sack, Phys. Lett. **B258** (1991) 469.

[21] A. Sommerfeld, *Atombau und Spektrallinien*, Bd. 2, Vieweg, Braunschweig (1939);
A.D. Sakharov, JETP **18** (1948) 631.

[22] V.S. Fadin, V.A. Khoze, A.D. Martin and A. Chapovsky, Phys. Rev. **D52** (1995) 1377.

[23] V.S. Fadin, V.A. Khoze, A.D. Martin and W.J. Stirling, Phys. Lett. **B363** (1995) 112.

[24] E.A. Kuraev and V.S. Fadin, Sov. J. Nuc. Phys. **41** (1985) 466;
G. Altarelli and G. Martinelli, Yellow Report CERN 86-02 (1996) 47.

[25] D. Bardin, M. Bilenky, A. Olchevski and T. Riemann, Phys. Lett. **B308** (1993) 403; **B357** (1995) 725(E);
D. Bardin, D. Lehner and T. Riemann, "Complete Initial State QED Corrections to Off-Shell Gauge Boson Pair Production in e^+e^- Annihilation" DESY 96-028 (1996).

[26] J. Fleischer, F. Jegerlehner and M. Zralek, Z. Phys. **C42** (1989) 409;
F. Jegerlehner in *Radiative corrections: Results and Perspectives*, eds. N. Dombey and F. Boudjema, NATO ASI Series, Plenum Press, New York (1990), 185.

[27] J.Ellis and K. Geiger, Physical Review **D54** (1996) 1967;
G. Gustafson and J. Häkkinen, Z. Phys. **C64** (1994) 659;
G. Gustafson, U. Petersson and P. Zerwas, Phys. Lett. **B209** (1988) 90.

[28] T. Sjöstrand and V.A. Khoze, Z. Phys. **C62** (1994) 281; Phys. Rev. Lett. **72** (1994) 28.

[29] J. Ellis and K. Geiger Phys. Rev. **D54** 1967; 1997 hep-ph/9703348, preprint CERN-TH/97-46.

[30] R. Hanbury-Brown and R.Q. Twiss, Nature **178** (1956) 1046;
G. Goldhaber, S. Goldhaber, W. Lee and A. Pais, Phys. Rev. **120** (1960) 300.

[31] T. Sjöstrand Comp. Phys. Commun. **82** 1994 74;

[32] L. Lönnblad and T. Sjöstrand Phys. Lett. **B351** (1995) 293.

[33] L. Lönnblad, T. Sjöstrand, *Modelling Bose-Einstein correlations at LEP2*, Eur. Phys. J. (1998) 165.

[34] S. Jadach and K. Zalewski, preprint CERN-PPE/97-30 (1997);
K. Fialkowski and R. Wit, Z. Phys. **C74** (1997) 145; hep-ph/9703227 (1997).

[35] Lep Design Report, vol. 1: *The LEP Injector Chain.* CERN-LEP/83-29 (1983);
Lep Design Report, vol. 2: *The LEP Design Report.* CERN-LEP/84-01 (1984).

[36] D. Decamp *et al.* (ALEPH Collaboration), *ALEPH: a detector for electron-positron annihilations at LEP*, Nucl. Inst. and Meth. **A294** (1990) 121.

[37] P. Aarnio *et al.* (DELPHI Collaboration), Nucl. Inst. and Meth. **A303** (1991) 233.

[38] B. Adeva *et al.* (L3 Collaboration), Nucl. Inst. and Meth. **A289** (1990) 33.

[39] K. Ahmet *et al.* (OPAL Collaboration), Nucl. Inst. and Meth. **A305** (1991) 275.

[40] C. Bowdery, ed. (ALEPH Collaboration), *The ALEPH Handbook*, vol. 1 (1995); vol. 2 (1997). Published by CERN.

[41] D. Buskulic *et al.* (ALEPH Collaboration), *Performance of the ALEPH detector at LEP*, Nucl. Inst. and Meth. **A360** (1995) 481.

[42] A.A. Sokolov and I.M. Ternov, Sov. Phys. Dokl. **8** (1964) 1203.

[43] V.N. Baier and Y.F. Orlov, Sov. Phys. Dokl **10** (1966) 1145;
A.A. Zholentz *et al.*, Phys. Lett. **B96** (1980) 214;
A.S. Artamonov *et al.*, Phys. Lett. **B118** (1982) 255;
D.P. Barber *et al.*, Phys. Lett. **B135** (1984) 498;
W.W. McKay *et al.*, Phys. Rev. **D29** (1984) 2483.

[44] LEP Energy Working Group, *LEP energy calibration in 1996*, LEP Energy Group/97-01 (March 1997);
`http://www.cern.ch/LEPECAL/reports/reports.html`.

[45] S. Jadach, W. Placzek, E. Richter-Wąs, B.F.L. Ward and Z. Wąs, *Upgrade of the Monte Carlo program BHLUMI for Bhabha scattering at low angles to version 4.04*, CERN-TH/96-158 (June 1996).

[46] P. Mató, *Data processing for Large* e^+e^- *Experiments*, Ph.D. thesis, Univ. of Barcelona (1990).

[47] M. Delfino *et al.*, Comput. Phys. Commun. **57** (1989) 401.

[48] J. Knobloch, *JULIA Users and Programmers guide*, ALEPH internal report, ALEPH 90-11 (1990).

[49] H. Albretch, E. Blucher and J. Boucrot, *ALPHA Users Guide*, ALEPH internal report, ALEPH 95-112 (1995).

[50] R. Frühwirth, HEPHY-PUB 503/87 (1987).

[51] B. Bloch-Devaux *et al.*, *KINGAL Users Guide*, ALEPH internal report, ALEPH 87-53 (1988).

[52] R. Brun *et al.*, *GEANT3 Users Guide*, CERN-DD/EE/84-1 (1987).

[53] F. Ranjard, *GALEPH-Monte Carlo program for ALEPH*, ALEPH internal report, ALEPH 88-119 (1988).

[54] H. Fesefeldt, *GHEISHA*, Aachen 3rd Inst. Nucl. Phys. **A23** (Proc. Suppl.) (1991) 291.

[55] M. Skrzypek, S. Jadach, W. Placzek and Z. Wąs, Comput. Phys. Commun. **94** (1996) 216.

[56] M. Skrzypek *et al.*, Phys. Lett. **B372** (1996) 289.

[57] E. Barberio and Z. Wąs, Comput. Phys. Commun. **79** (1994) 291.

[58] V.S. Fadin, V.A. Khoze, A.D. Martin and A. Chapovsky, Durham report DTP/94/116 (1994);
V.S. Fadin *et al.*, Phys. Rev. **D52** (1995) 1377.

[59] J. Fujimoto *et al.* (MINAMI-TATEYA Collaboration), *GRACE User's manual, version 2.0*, KEK report 92-19 (1993) (submitted to Comput. Phys. Commun.).

[60] T. Sjöstrand, Comput. Phys. Commun. **82** (1994) 74.

[61] Working Group on QCD Event Generators, in "Physics at LEP2",

[62] G. Altarelli, T. Sjöstrand and F. Zwirner eds., CERN 96-01 (1996), vol.2, 103.

[63] F.A. Berends, R. Pittau and R. Kleiss, Comput. Phys. Commun. **85** (1995) 437.

[64] F.A. Berends, G. Burgerse and W.L. Van Neerven, Phys. Lett. **B185** (1987) 395; Nuc. Phys. **B297** (1988) 429; Nucl. Phys. **B304** (1988) 921.

[65] T. Sjöstrand and V.A. Khoze, Z. Phys. **C62** (1994) 281.

[66] G. Marchesini and B.R. Webber, Nucl. Phys. **B310** (1988) 461;
I. Knowles, Nucl. Phys. **B310** (1988) 571;
G. Marchesini *et al.*, Comput. Phys. Commun. **67** (1992) 465.

[67] ALEPH Collaboration, Phys. Lett. **B313** (1993) 509.

[68] S. Jadach, B.F.L. Ward and Z. Wąs, Comput. Phys. Commun. **79** (1994) 466.

[69] H. Anlauf *et al.*, Comput. Phys. Commun. **79** (1994) 466.

[70] H. Albrecht, E. Blucher, J. Boucrot *ALPHA: Aleph Physics Analysis Package*, ALEPH internal report, ALEPH 97-058, SOFTWR 97-003 (June 1997).

[71] W. Bartel *et al.* (JADE Collaboration), Z. Phys. **C33** (1986) 23;
S. Bethke, Habilitation thesis, LBL 50-208 (1987).

[72] S. Catani, Yu. L. Dokshitzer, M. Olsson, G. Turnock and B.R. Webber, Phys. Lett. **B269** (1991) 432.

[73] T. Sjöstrand, Comput. Phys. Commun. **28** (1983) 227.

[74] Working Group on QCD, in "Z Physics at LEP 1", G. Altarelli, R. Kleiss and C. Verzegnassi eds., CERN 89-08 (1989), vol.1, 373.

[75] C. Guicheney *et al.*, NIM A362 (1995) 478-486.
C. Guicheney *et al.*, *WW cross-section measurement at 172 GeV using a Neural Network*, ALEPH internal report, ALEPH 97-053, PHYSIC 97-047 (1997);
`http://alephwww.cern.ch/~guichene/ww_tools/qnnwtag.html`.

[76] ALEPH Collaboration, *A Precise Measurement of* $\Gamma_Z \to b\bar{b}/\Gamma_Z \to$ *hadrons*, Phys. Lett. **B313** (1993) 535.

[77] A. Tilquin *et al.*,
`http://alephwww.cern.ch/LEP2ANALYSIS/WTF/code/mathkine.doc`.

[78] V. Blobel in: European Physical Society, "Formulae and methods in experimental data evolution", vol 3, (1984), p. L1.

[79] J.B. Hansen, "Triple Gauge-boson Couplings in W Pair Production via e^+e^- Annihilation", October 1996.

[80] A. Travelsi, *Direct* W *mass measurement from 170 and* 172 GeV *data*, ALEPH 97-025, PHYSIC 97-020, 1997.

[81] A. Blondel, Private communication, 22/4/1997.

[82] G. altarelli, T Sjöstrand and F. Zwirner, "Physics at LEP2", vol 1, (1996).

[83] A. Moutoussi, Private communication.

[84] A. Travelsi,"Direct W mass measurement from 170 and 172 GeV data", ALEPH 97-025, PHYSIC 97-020.

[85] G. Merino, Private communication.

[86] P. Perez, Private communication.

[87] A. Juste, *Measurement of the W mass in* e^+e^- *annihilation*, Ph. Dissertation, June 1998.

[88] M. Vreeswijk,
`http://alephwww.cern.ch/~jezeques/WmassWeiKWCC03.F`

[89] D. Bardin et al. "Semi-Analytical Approach fto Four-Fermion Production in e^+e^- Annihilation." CERN-TH-7295-94 (1994).
D. Bardin et al. "GENTLE/4fan: a package of Fortran programs for the description of e^+e^- annihilation into four fermions." DESY-ZEUTHEN-96-05 (March 1996).

[90] ALEPH collaboration, *Studies of Quantum Chromodyniamics with the ALEPH detector*, CERN-PPE/96-186, submitted to Physics Reports.

[91] F.A. Berends, R. Pittau and R. kleiss, Comp. Phys. Commun. 85 (1995) 437.

[92] I. Riu, *W mass Background Systematic Study using Z peak data*, ALEPH 97-060, PHYSIC 97-053.

[93] F. Ligabue, `http://alephwww.cern.ch/~ligabue/syst/syst.html`

[94] M.-N. Minard, Private Communication, 12 March 1997.

[95] R.M. Barnett et al., Phys. Rev. D54 (1996) 1.

[96] M. Skrzypek, S. Jadach, W. Placzek and Z. Was, Comp. Phys. Commun. 94 (1996) 216.

[97] D.R. Yennie, S.C. Frautschi and H. Suura, Annuals of Phys. **13** (1961) 379. S. Jadach and B.F.L. Ward, TPJU - 15/88 (1988).

[98] S. Jadach and K. Zalewski,*W mass Reconstruction from Hadronic Events in LEP2: Bose-Einstein effect*, CERN-TH/97-29, February 1997.

[99] E.A. Kuraev and V.S. Fadin, Sov. J. Nucl. Phys. **41** (1985) 466.

[100] The working group on LEP energy, *LEP Energy Calibration in 1996*, LEP Energy Group/97-01.

[101] T. Sjöstrand and V.A. Khoze, Z. Phys. C62 (1994) 281.

[102] G. Gustafson, U. Pettersson and P. Zerwas, Phys. Lett. B209 (1988) 90.

[103] T. Sjöstrand and V.A. Khoze, Phys. Rev. Lett. 72 (1994) 28.

[104] J. Ellis and K. Geiger, CERN-TH/97-046, submitted to Phys. Lett. B.

[105] S. Jadach and K. Zalewski, CERN-TH/97-29 (1997).

[106] S. Jezequiel, `http://alephwww.cern.ch/~jezeques/bose.F`

[107] J.A. Hertz, A. Krogh and R.G. Palmer, *Introduction to the theory of neural computation*, Addison-Wesley, Redwood City CA, 1991;
K. Hornik, M. Stinchcombe and H. White, *Neural Networks* **2** (1989) 359;
B. Müller and J. Reinhardt, *Neural networks: an introduction*, Springer-Verlag, Berlin, 1991.

[108] Y. Le Cun, Proc. Cognitiva 85, Paris (1985) 599.

[109] V. Breton et al., NIM **A362** (1995) 478.

[110] ALEPH Collaboration, *Measurement of the W mass by Direct Reconstructino in* e^+e^- *Collisions at* 172 GeV , Phys. Lett. B422 (1998) 384.

[111] Particle Data Group, Eureo. Phys. Jour. **C3** (1998) 90.

[112] T. Sjöstrand, Private Communication.

[113] O. Buchmüller et al., *On Colour Rearrangement Effects in Hadronic WW Events - Predictions of the HERWIG and VNI Generators* -, ALEPH internal report, ALEPH 98-059, PHYSIC 98-026, 1998.

[114] ALEPH Collaboration, *Bose-Einstein correlations in W-pair decays*, Contribution to ICHEP98, Paper 894 to be published in the Proceedings.

[115] LEP energy working group, *LEP energy calibration above the* W *threshold*, contribution to ICHEP98 Abstract 352.

[116] ALEPH Collaboration, *Measurement of the W mass in* e^+e^- *Collisions at* 183 GeV , 29th ICHEP, Vancouver, July 1998.

[117] LEPEWWG/MW/98-02, *LEP WW cross-section and W mass for '98 Summer conferences*, (1998).

[118] D. Karlen, Experimental Status of the Standard Model, 29th ICHEP, Vancouver, July 1998.

[119] CCFR Collaboration, K. McFarland *et al.*, *A precision measurement of electroweak parameters in Neutrino-Nucleon Scattering*, Eur. Phys. J. C1 (1998) 509.

[120] The NuTeV, D0, CDF collaborations, *Precision Measurement of* $\sin^2\theta_W$ *from* νN *Scattering at NuTeV and Direct Measurements of* M_W, Fermilab-Conf-98-200-E, to be published in the proceedings of the 6th international workshop of Deep Inelastic Scattering, Brussel, Belgium (1998).
T. Bolton, Presentation in the 29th ICHEP in Vancouver (1998).

[121] E.A. Paschos and L. Wolfenstein, Phys. Rev. D7 (1973) 91.